Examination of Cone Photoreceptor Packing and Foveal Architecture in Eyes of Children and Adults

by

Hanieh Mirhajianmoghadam

A dissertation submitted to the Vision Sciences Department,
College of Optometry
in partial fulfillment of the requirements for the degree of

DOCTOR OF PHILOSOPHY

in Physiological Optics

Chair of Committee: Jason Porter, Ph.D.

Committee member: Lisa A. Ostrin, O.D., Ph.D.

Committee member: Nimesh B. Patel, O.D., Ph.D.

Committee member: Toco Y. P. Chui, Ph.D.

University of Houston
August 2020

DEDICATION

To my parents, my siblings, and my husband. Thanks for everything.

ACKNOWLEDGMENTS

First and foremost, I would like to express my sincere gratitude to my advisor, Jason Porter for all of his guidance, motivation, and support throughout my PhD. His willingness to help me, whether it was hanging my first ARVO poster or answering my very basic questions with patience, is greatly appreciated. Thanks for teaching me skills that are transferable outside the lab and providing me the opportunity to grow as a more independent researcher.

I am deeply indebted to Dr. Patel for his invaluable help and guidance with MATLAB coding and any OCT-related issue, and for allowing me to use clinical tools in his lab. Our discussions always motivated me to think outside the box.

I am also extremely grateful to Dr. Ostrin for allowing me to collaborate with her on the Kids imaging project and for her valuable scientific and writing help. Additionally, many thanks to her for accepting me as a postdoctoral fellow in her lab.

Next, I wish to extend my gratitude to Dr. Chui for her expert advice and intellectual guidance, especially for different aspects of the third project.

Moreover, I cannot thank Dr. Frishman enough for providing me with the opportunity to be part of the UHCO family and dealing with my problems over the past 5 years.

The research presented here could not have been accomplished without the technical support and generous help of Ms. Hope Queener, Dr. Alex Schill, and Ms. Mindy Fox.

To the past and present members of Dr. Porter's lab, thanks for helping me to gather the data and run the AOSLO system. Particularly, Gwen and Suman for reading the initial drafts of all of the chapters presented here and helping me whenever I needed it.

Special thanks go to all UHCO faculty, staff, and graduate students for making UHCO an incredible place to pursue science and a wonderful community to be part of.

Last but not least, I cannot begin to express my thanks to my parents, Mahnaz and Abbas, for their love, prayers, and sacrifices, as well as teaching me the value of honesty and

perseverance. I am grateful to my sister, Hengameh, for putting the idea of studying abroad into my head and for her unwavering support. I also wish to thank my brother, Mohammadreza, for his relentless support and motivation. I also owe much gratitude to my husband, Rasoul, who was with me through thick and thin for the past 4 years and has constantly encouraged me when the path was arduous. His unfailing love, patience, and understanding made the completion of this chapter of my life possible.

ABSTRACT

Purpose: The fovea is a specialized retinal region that plays an integral role in vision. The goal of this dissertation was to better understand whether axial elongation impacts (a) overall foveal geometry in adults and children, and (b) parafoveal microvascular geometry in adults.

Methods: (1) Foveal pit parameters were quantified from volume scans acquired in healthy adult eyes using spectral domain optical coherence tomography. Cone density, cone spacing, and foveal avascular zone (FAZ) geometry were quantified from adaptive optics scanning laser ophthalmoscope (AOSLO) images of cone photoreceptors and foveal capillaries. Metrics were compared between eyes with short and long axial lengths (ALs). (2) Cone density and spacing, foveal pit, and FAZ metrics were quantified in healthy children and examined as a function of age and refractive status. (3) AOSLO images of FAZ microvasculature were used to quantify metrics of parafoveal intercapillary regions (PICRs) within 3 zones in healthy adults. Metrics were examined as a function of axial length and FAZ geometry.

Results: (1) Adult eyes with long ALs had lower cone densities and increased cone spacing (increased farthest neighbor, nearest neighbor, and intercell distances) ($P<0.02$). In the long AL group, eyes with larger FAZ areas had larger foveal pit volumes ($P=0.004$), areas ($P=0.004$), and diameters ($P=0.003$). Cone density was not related to FAZ area or foveal pit volume. (2) Foveal pit and FAZ metrics were not related to the age, axial length, or refractive status of healthy children. Cone density was lower in myopic versus non-myopic children at eccentricities of 0.2 and 0.3 mm ($P<0.001$). Age and cone density were not related after controlling for AL. (3) PICR minor axis was not related to axial length or FAZ area. However, eyes with smaller FAZ areas had more circularly-shaped PICRs, as evidenced by increased values of PICR circularity ($P<0.05$ for all zones).

Conclusions: This dissertation increases understanding of the role of axial elongation on foveal features in healthy adults and children. Results suggest that the morphometry of the FAZ,

parafoveal microvasculature, and foveal pit are not related to eye's axial length, whereas cone density and spacing are affected by axial elongation.

TABLE OF CONTENTS

LIST OF TABLES

LIST OF FIGURES

CHAPTER 1

General Introduction

1.1 The healthy human fovea

The fovea centralis (fovea) is a specialized region of the human retina. It is approximately 1.5 mm in diameter and has unique morphological and functional characteristics that distinguish it from the surrounding retina. For example, the healthy fovea is typically characterized anatomically by the excavation of inner retinal layers (forming the foveal pit), a capillary-free region known as the foveal avascular zone (FAZ), and increased cone density. Due to these (and other) properties, the fovea of a healthy eye provides the highest spatial sampling of the retinal image, is the location for maximal visual acuity, and enables trichromatic color vision (Hirsch & Curcio, 1989; Rossi & Rooda, 2010). Thus, the fovea plays an integral role in our ability to visualize the environment.

1.1.1 Foveal pit structure

In the healthy adult human fovea, inner retinal layers are typically displaced laterally forming a depression called the foveal pit (Figure 1-1). The margin of the pit is characterized by an accumulation of cells in the ganglion cell and inner nuclear layers. Some studies have suggested that the foveal pit may have evolved in primate eyes to maximize the amount of unimpeded light that is incident on the central-most foveal cones (i.e., reduce the amount of light that might normally have been scattered if retinal cells were not removed from above the photoreceptors) (Martin, 1986; Provis et al., 2013) while more recent studies have argued that it has no functional importance (Marmor et al., 2008; McAllister et al., 2010). The size of the foveal pit is quite variable among healthy adult eyes (Dubis et al., 2012; Wilk et al., 2017), with diameters ranging from approximately 1 to 2.5 mm, and significantly varies with race/ethnicity and age (Wagner-Schuman et al., 2011; Nesmith et al., 2014). An absence of the foveal pit (i.e., the persistence of inner retinal layers) may present on its own or in association with conditions such as albinism (Recchia et al., 2002).

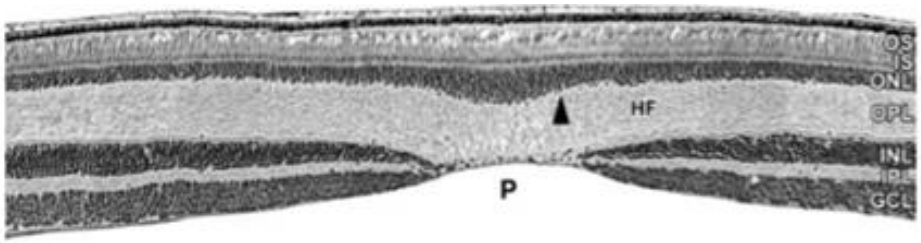

Figure 1-1. A cross-section of the human fovea, showing the foveal pit (P) formed by the absence of inner retinal layers. Anterior retinal layers are located at the bottom of the image, while posterior layers are located toward the top. Light from the outside environment would travel from the bottom to the top of this image. HF, Henle fibers; OS, outer segment; IS, inner segment; ONL, outer nuclear layer; OPL, outer plexiform layer; INL, Inner nuclear layer; IPL, Inner plexiform layer; GCL, ganglion cell layer. Reprinted with permission (Springer & Hendrickson, 2004b).

1.1.2 Vasculature and the foveal avascular zone (FAZ)

The vascular network that supplies the retina derives primarily from two sources that are provided by several branches of the ophthalmic artery. The outer retina receives its nourishment from the choriocapillaries, which originate from the short posterior ciliary arteries that pierce through the sclera around the optic nerve. The inner two-thirds of the retina is supplied by the central retinal artery, which branches off of the ophthalmic artery, enters the eye along the optic nerve, and divides into four major branches that each supply a distinct quadrant of the retina. While the central retinal artery branches into several vascular plexuses, the number of vascular plexuses and their arrangement regionally vary within the retina. Despite the presence of up to four vascular networks in the macular region (Snodderly et al., 1992; Tan et al., 2012; Chan et al., 2015), the fovea typically contains a central region that is devoid of vasculature, called the foveal avascular zone (FAZ), that is bordered by a single layer of capillaries (Iwasaki & Inomata, 1986; Snodderly et al., 1992; Provis et al., 2000). The size of the FAZ is quite variable among healthy individuals. While it is known that the area of the FAZ varies with race (Linderman et al., 2018), conflicting evidence exists on whether relationships exist between FAZ structural

properties and other demographic properties. For example, it is still inconclusive whether there is a relationship between gender and the size of the FAZ. Linderman et al. (2017) and Rommel et al. (2018) reported larger FAZ areas in females compared to males, whereas Fujiwara et al. (2017) did not observe gender differences. There is also an inconsistency in the literature regarding whether FAZ size is related to age (Fujiwara et al., 2017; Falavarjani et al., 2018; Tan et al., 2016).

1.1.3 Photoreceptors

The human retina contains 4.6 million cones and 92 million rods, on average (Curcio et al., 1990). In a typical eye, the foveal region contains approximately 200,000 cones while the central-most part of the fovea that contains only cones, the foveola (~250 to 350 µm in diameter), possesses approximately 7,000 cones and has the highest density of cone photoreceptors (Curcio et al., 1990). Values for the peak cone density in healthy eyes have been reported to vary between 100,000-324,000 cones/mm^2 based on histological examination (Curcio et al., 1990; Diaz-Araya et al., 1993) and between 100,000-216,000 cones/mm^2 in *in vivo* studies (Putnam et al., 2005; Li & Roorda, 2010).

Figure 1-2 illustrates the distribution of rods and cones in a healthy retina as a function of eccentricity from the foveal center. Cone density (red line) reduces precipitously as one moves away from the foveal center (Osterberg, 1935; Curcio et al., 1990) and levels off at an eccentricity of approximately 3 mm (~10-12°). Within this range, the cones change from being thin, long, and tightly packed at the foveal center to wider, shorter, and increasingly spaced in the periphery. Conversely, the density of rods (black line) increases rapidly from the foveal center to reach its peak value at an eccentricity of 3-5 mm (~10-18°) (Curcio et al., 1990; Jonas et al., 1992). At 400-500 µm (~1.5°) from the foveal center, rods and cones have equal density (Osterberg, 1935; Curcio et al., 1990).

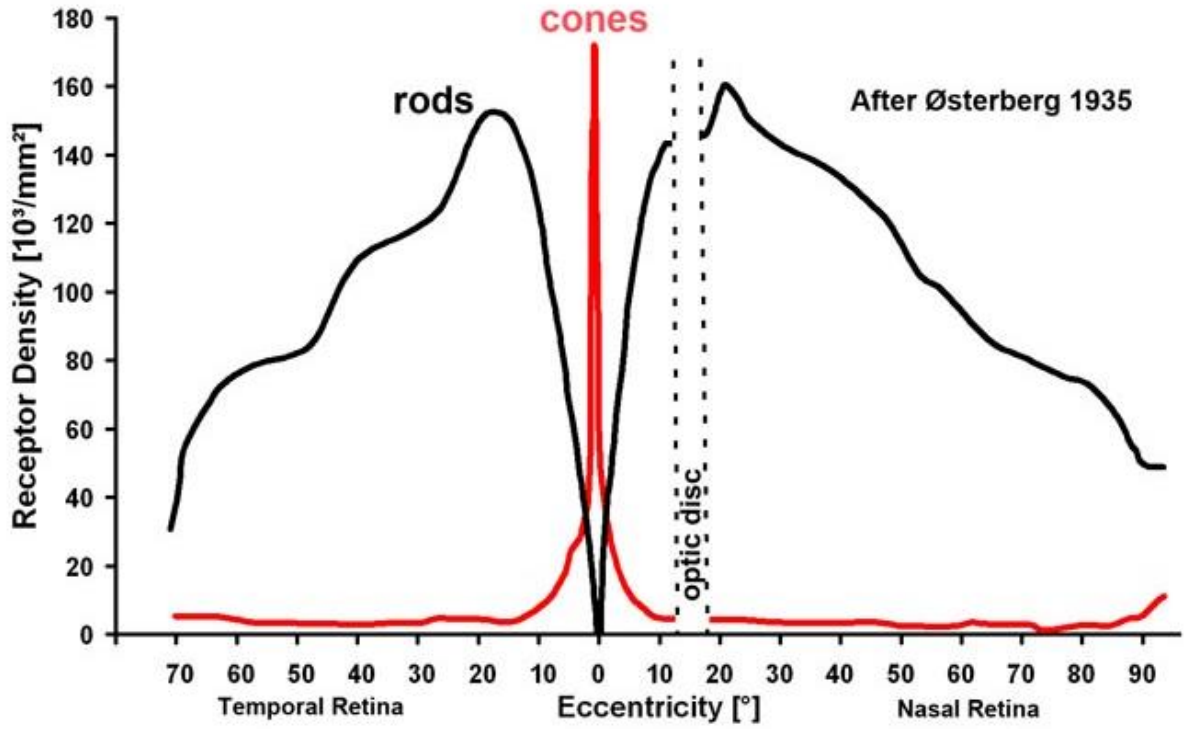

Figure 1-2. Density of rod (black line) and cone (red line) photoreceptors along the horizontal meridian in a healthy human retina. The density of cones drops steeply with increasing eccentricity from the foveal center, whereas the density of rods increases to reach a peak at an eccentricity of approximately 18-20° and then decreases. (https://webvision.med.utah.edu/book/part-iii-retinal-circuits/circuitry-for-rod-cells-through-the-retina/)

Cone packing varies within the retina and can be influenced by different factors. Cones tend to be asymmetrically packed within retina, with cone density being greater along the horizontal meridian compared to vertical meridian at the same retinal eccentricity (Curcio et al., 1990; Mirhajianmoghadam et al., 2020). Along the horizontal meridian, cone density tends to taper off more quickly with increasing eccentricity in the temporal direction compared to the nasal direction (Curcio et al., 1990). While no significant differences in cone density have been found between genders and racial groups (Park et al., 2012; Legras et al., 2018), cone density does decrease with increasing age (Song et al., 2011). In addition, the variability in cone density across subjects is highest at the foveal center and decreases with increasing eccentricity

(Curcio et al., 1990). This change in variability is thought to reflect variations in the extent or rate of inward migration of cones toward the foveal center during development (which will be further discussed in the following sections) (Curcio et al., 1990).

1.2 Foveal development and maturation

Foveal development is a protracted process. Pronounced morphological changes occur before and after birth as the fovea becomes fully developed and adult-like. However, the timing and rate of development vary for different foveal features.

1.2.1 Development of the foveal pit and the FAZ

The site of the future fovea can be identified as early as 11 weeks gestation and is typically characterized by the presence of a thickened ganglion cell layer and a single layer of pure cones (Linberg & Fisher, 1990; Provis et al., 1998). The foveal pit is formed during the second half of gestation (Hendrickson & Yuodelis, 1984; Hendrickson, 1992) by the centrifugal migration of inner retinal neurons away from the foveal center toward the foveal rim. At this stage, inner retinal cells are already synaptically coupled with cones. Initially, the foveal pit is deep and narrow, but becomes wider and shallower after birth up to 4 years of age (Hendrickson, 1992; Hendrickson et al., 2012; Springer & Hendrickson, 2005) (Figure 1-3).

In the earliest stages of development, the retina receives oxygen and nutrients through hyaloid vasculature, which resides within the vitreous. However, the hyaloid vascular system retracts and retinal vascularization starts from 14-16 weeks gestation from the optic nerve head and spreads radially over the surface of the retina. The superficial retinal vessels dive deeper and bud to from inter-connected vascular networks. Interestingly, retinal vessels skirt around the incipient fovea during this time. Studies suggest that ganglion cells express factors that repel astrocytes and prevent the formation of blood vessels (Kozulin et al., 2009a; Kozulin et al.,

2010), leading to the definition of an avascular region. Enormous evidence indicates that the presence of a FAZ is a prerequisite for the development of a foveal pit and if the FAZ fails to develop, a foveal pit is not formed. Postnatally, the FAZ enlarges until at least 15 months of age as the foveal pit matures and remodels (Provis & Hendrickson, 2008).

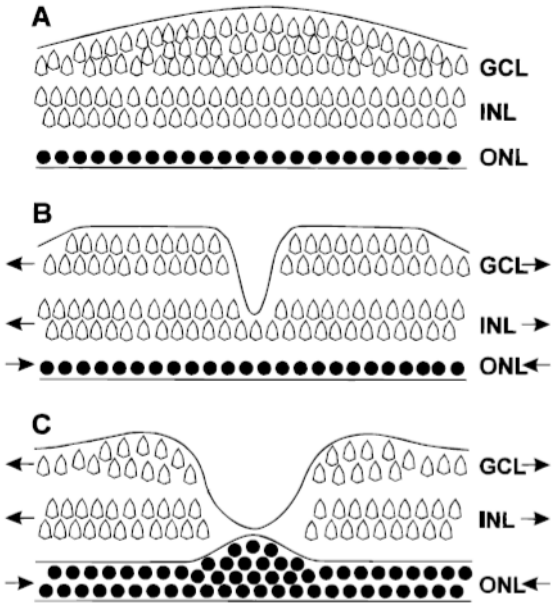

Figure 1-3. Illustrations of the retina at different stages of foveal development. (A) The appearance of the central retina prior to the early emergence of the fovea. Cone nuclei form a monolayer in the outer nuclear layer (ONL) and the ganglion cell layer (GCL) is thickened. (B) During the third trimester, the foveal pit begins to form. Arrows indicate the direction in which cells in different layers move. Cells in the outer retina tend to crowd toward the incipient fovea whereas cells in the inner nuclear layer (INL) and GCL move centrifugally. (C) The foveal pit becomes shallower and wider in the adult retina and extends through the original GCL and INL. The centripetal movement of cones leads to the accumulation of cone nuclei in the ONL. Reprinted with permission (Springer 1999).

1.2.2 Photoreceptor development

At around 11 weeks of gestation, foveal cones differentiate and start to form a single layer underlying the thickened ganglion cell layer (Linberg & Fisher, 1990). Cones are 6-8 µm wide with short axons by 25 weeks of gestation (Hendrickson et al., 2012). The primitive inner

segment (IS) and outer segment (OS) of foveal cones are very short and immature. However, in the periphery, rods and cones are more developed and have slightly longer inner and outer segments (Yuodelis & Hendrickson, 1986; Vajzovic et al., 2012; Hendrickson et al., 2012). As the pit begins to form, cones become more tapered and their axons elongate to maintain their synaptic contacts. Rods are originally absent from the central 1500-1800 μm of the retina. However, the diameter of the rod-free zone narrows. Studies suggest that rods and cones migrate toward the center of the fovea throughout development, probably as soon as they differentiate (Diaz-Araya & Provis, 1992). Hence, foveal cone density doubles between 22 weeks gestation and birth (Yuodelis and Hendrickson, 1986). Nevertheless, this value is far from the average adult cone density. The development and maturation of photoreceptors are mainly postnatal events as cones are markedly immature at birth (Yuodelis & Hendrickson, 1984; Yuodelis & Hendrickson, 1986; Hendrickson 1992). After birth, cones become thinner and their IS and OS lengths increase dramatically (Figure 1-4). A few weeks after birth, inner and outer segments of foveal cones are still shorter than those of cones in the periphery, and become similar in length to those of peripheral cones between 9 and 15 months after birth (Hendrickson 1992). As cones migrate centripetally, their axons further elongate and their nuclei stack on top of each other to accommodate increased cone packing. Histological studies have shown that OS length and the density of foveal cones at 45 months of age are only half of adult values (Yuodelis & Hendrickson, 1986) and that the fovea appears fully mature at 13 years of age (Hendrickson et al., 2012). Longitudinal *in vivo* studies in rhesus monkeys also confirm the postnatal maturation of the fovea (Patel et al., 2017).

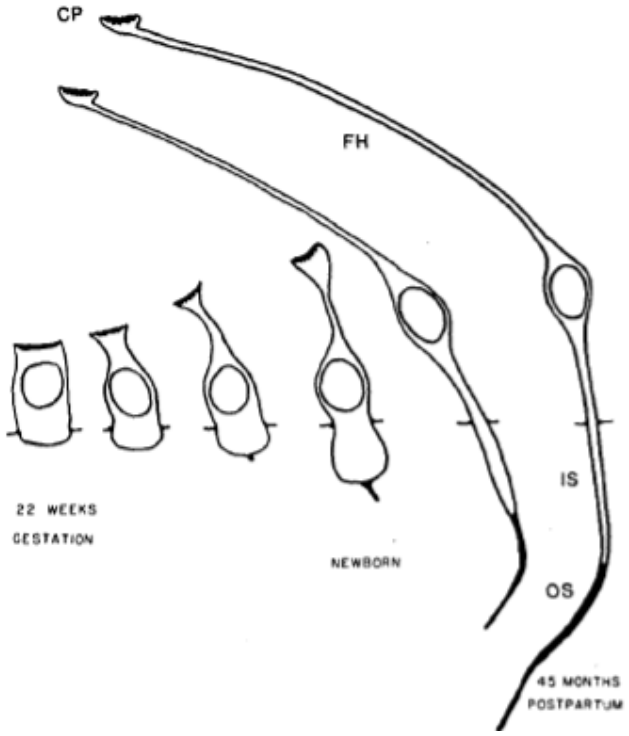

Figure 1-4. Schematic drawing showing the development and maturation of foveal cones between 22 weeks gestation and 45 months after birth. From left to right, cones are shown at 22 weeks gestation, 24 to 26 weeks gestation, 34 to 36 weeks gestation, at birth (newborn), 15 months after birth, and 45 months after birth. Striking morphological changes of foveal cones occur after birth. OS, outer segment; IS, inner segment; CP, cone pedicle; FH, Henle fiber. Reprinted with permission (Hendrickson & Yuodelis 1984).

1.2.3 Mechanisms of foveal development

In general, there are two proposed models for foveal formation: active and passive. The active model suggests that gradients of trophic factors and signaling molecules attract cones toward the foveal center and repel inner retinal layers away from it. As the density of neurons at the incipient fovea increases, they experience hypoxia, as evidenced by the upregulation of angiogenic factors (Sandercoe et al., 2003). However, the primitive fovea remains avascular due to a high expression of anti-angiogenic factors secreted by retinal ganglion cells (Kozulin et al., 2009a; Kozulin et al., 2010). Gradients of axonal guidance factor EphA6 have also been suggested to repel astrocytes from the emerging fovea (Kozulin et al., 2009b). Yet, it is not quite

clear what factors guide cone packing. Fibroblast growth factor mediates cone narrowing and elongation (Cornish et al., 2005). It is also speculated that the presence of adhesive interactions between adjacent photoreceptors during their elongation promotes the centripetal displacement of cones toward the central retina, leading to increased cone packing (Provis et al., 2013).

On the other hand, the passive model of foveal formation was proposed based on finite element analysis of a model of developing retina (Springer & Hendrickson, 2004a). This model suggests that forces normally present in the developing eye, such as intraocular pressure (IOP), along with growth-induced retinal stretch, deform the avascular retina (or FAZ) to give rise to a foveal pit. According to this model, the absence of retinal vasculature alters the rigidity of the tissue and allows passive forces to form the foveal pit. Without the FAZ, a pit does not emerge. Modeling also suggests that presence of the pit, combined with retinal stretching, leads to centripetal displacement of cones toward the foveal center (Springer, 1999). Based on the passive explanation, the sizes of the FAZ and the foveal pit, along with cone packing, should all be correlated.

More recently, a hybrid “active-passive” model has been proposed for foveal development (Wilk et al., 2014) in which the initial packing of cones is due to an active component and the foveal pit forms due to mechanical forces (mainly IOP) at the FAZ. Subsequently, growth-induced stretch promotes the elongation and further packing of cones toward the foveal center. This hybrid model predicts that the presence of the pit facilitates additional cone packing.

1.3 Axial elongation and myopia

On average, the length of the human eye is 17 mm at birth and increases by approximately 5 mm up to 6 years of age (Mutti et al., 1996). However, a substantial proportion of growth occurs during the first year of life (Larsen, 1971; Brown et al., 1999). While the axial length of the eye

increases, the cornea and crystalline lens flatten to maintain emmetropia. Interestingly, corneal changes are usually limited to the first two years of life (Insler et al., 1987; Friedman et al., 1996), whereas the crystalline lens loses almost 20 Diopters of power over the first 6 years of life (Zadnik et al., 1993).

Refractive errors occur due to a mismatch between eye's refractive power and its axial length. In the case of myopia, the eye is longer than its focal length. Consequently, light rays from infinity focus in front of the retina. Myopia is the most common ocular disorder worldwide (Pararajasegaram et al., 1999; Pan et al., 2012) and its prevalence has increased rapidly, especially in East-Asia (Wong et al. 2000; Shimizu et al., 2003). Vast majority of studies have shown that increase in myopia is due to increase in axial length (McBrien & Millodot, 1987; Bullimore et al., 1992; Grosvenor & Scott, 1993; Llorente et al., 2004; Hou et al., 2018).

Various ocular structures have been reported to be altered in axial myopes compared to emmetropes. For example, linear cone density (cones/mm^2) is significantly lower in myopic compared to emmetropic adult eyes (Chui et al., 2008a; Lombardo et al., 2012), while myopes tend to have shallower and less steeply-sloped foveal pits relative to emmetropes (Dubis et al., 2012). Such changes are attributed, in part, to retinal stretching in elongated myopic eyes.

Early onset myopia (or school/juvenile myopia) manifests during early childhood (between 9 to 11 years of age), progresses through adolescence, and is reported to account for 60% of myopic cases in the United States (Gilmartin 2004). Most of our knowledge about differences in foveal structure between myopes and emmetropes is mainly derived from developed adult retinas. Differences in FAZ area and retinal thickness associated with axial elongation and myopia have been recently studied *in vivo* in children (Read et al., 2015; Lee et al., 2015; Hsu et al., 2019, Golebiewska et al., 2019). However, it is still unclear whether cone packing and foveal pit geometry are different between myopic and emmetropic children. Recently, Park et al. (2013) and Tumahai et al. (2018) performed adaptive optics imaging of

cone photoreceptors in groups of children and adults. However, values of cone density were not reported for children separately and the closest eccentricity examined was 0.45 mm from the foveal center.

1.4 *In vivo* retinal imaging

Histological imaging provides valuable information about retinal structure with high anatomical resolution. However, this technique requires the use of excised tissue, which prohibits the longitudinal examination of the same tissue and can also suffer from post-processing artifacts. *In vivo* retinal imaging, on the other hand, provides the ability to image the same eye over time and document changes longitudinally. Fundus imaging is a traditional clinical technique used to visualize the posterior pole *in vivo*. While this technique has proven to be very valuable for examining healthy and diseased eyes, its wide-field images are limited in their ability to detect change at a microscopic level.

Optical coherence tomography (OCT) is a more recent non-invasive optical imaging modality that provides cross-sectional images of the living retina (Huang et al. 1991). In brief, OCT provides cross-sectional retinal images by measuring the magnitude and echo time delay of backscattered light. Early time domain OCT (TD-OCT) systems have more recently been replaced with spectral domain OCT (SDOCT) systems that can perform faster scans with higher axial resolution (~3-5 µm) (Wojtkowski et al., 2004; Chen et al., 2005), which is comparable to that found in histological sections. While OCT systems provide excellent resolution in depth, current commercial systems provide lateral resolutions of only 15 to 20 µm (Popescu et al., 2011). Therefore, current SDOCT systems lack the lateral resolution required for cellular imaging, as these instruments do not correct for the eye's optical aberrations.

Adaptive optics (AO) is a technology used to compensate for and minimize aberrations and, thereby, improve the performance of optical systems. Although originally designed for

astronomical telescopes, adaptive optics has extended into retinal imaging (and other fields) as it provides substantial improvements in lateral resolution (~2.5 μm in a healthy human eye).

1.4.1 Adaptive optics scanning laser ophthalmoscope (AOSLO)

Liang et al. (1997) combined adaptive optics with fundus imaging to acquire images of the living human retina at a microscopic spatial scale for the first time. Since then, adaptive optics has incorporated into other ophthalmic imaging modalities. Roorda et al. (2002) were the first to combine adaptive optics with a confocal scanning laser ophthalmoscope (SLO). First invented by Webb et al. (1980), an SLO scans a light source across the retina in a raster pattern. Reflected light is detected by a scientific camera (such as an avalanche photodiode or photomultiplier tube). However, a confocal pinhole is placed immediately before the detector to collect only that light which is reflected from the plane of focus and to reject (or block) light that is scattered or reflected back from other retinal structures. Compared to conventional SLO imaging, an adaptive optics scanning laser ophthalmoscope (AOSLO) provides higher axial and lateral resolution (Roorda et al., 2002), and has been widely used to study retinal structures such as cone photoreceptors (Chui et al., 2008a; Li et al., 2010; Lombardo et al., 2012), retinal vasculature (Tam et al., 2010; Chui et al., 2012), and the lamina cribrosa (Ivers et al., 2011) in normal and diseased eyes.

For all of the studies included in this dissertation, we used the Houston adaptive optics scanning laser ophthalmoscope (AOSLO) (Figure 1-5). The system uses a superluminescent diode (SLD) light source (S Series Broadlighter SLD, S-840-B-I-20, Superlum, Carrigtwohill, Ireland) with a center wavelength of 840 nm (full width at half maximum = 50 nm) for aberration correction and imaging. Light from the SLD is raster scanned horizontally using a resonant scanner (Electro-Optical Products Corp, Glendale, NY USA) operating at 14.9 kHz and vertically using a galvanometric scanner (GSI Group Corp, Bedford, MA USA) operating at 25 Hz.

Aberrations are measured using a custom-built Shack-Hartmann wavefront sensor and are corrected using a deformable mirror (Hi-Speed DM97-15, ALPAO, Montbonnot-Saint-Martin, France). Light is detected using photomultiplier tubes for the confocal and split detector channels.

As mentioned above, the Houston ASOLO includes a split detector imaging configuration that allows for non-confocal or multiply scattered light to be collected simultaneously to that collected through the confocal channel. In brief, a reflective annular mirror is placed in in the imaging light path. The confocal (directly back scattered) signal is reflected off of the annular mirror to the confocal detector (PMT1) while multiply scattered light continues to propagate until it strikes a knife edge mirror that splits the remaining light in half between the two split detector photomultiplier tubes (PMT2, PMT3). The split detector signal is then calculated as the difference between the intensities of the two split detector signals divided by their sum (Scoles et al., 2014). Using multiply scattered light in AOSLO imaging provides excellent contrast for visualizing blood vessels (Chui et al., 2012).

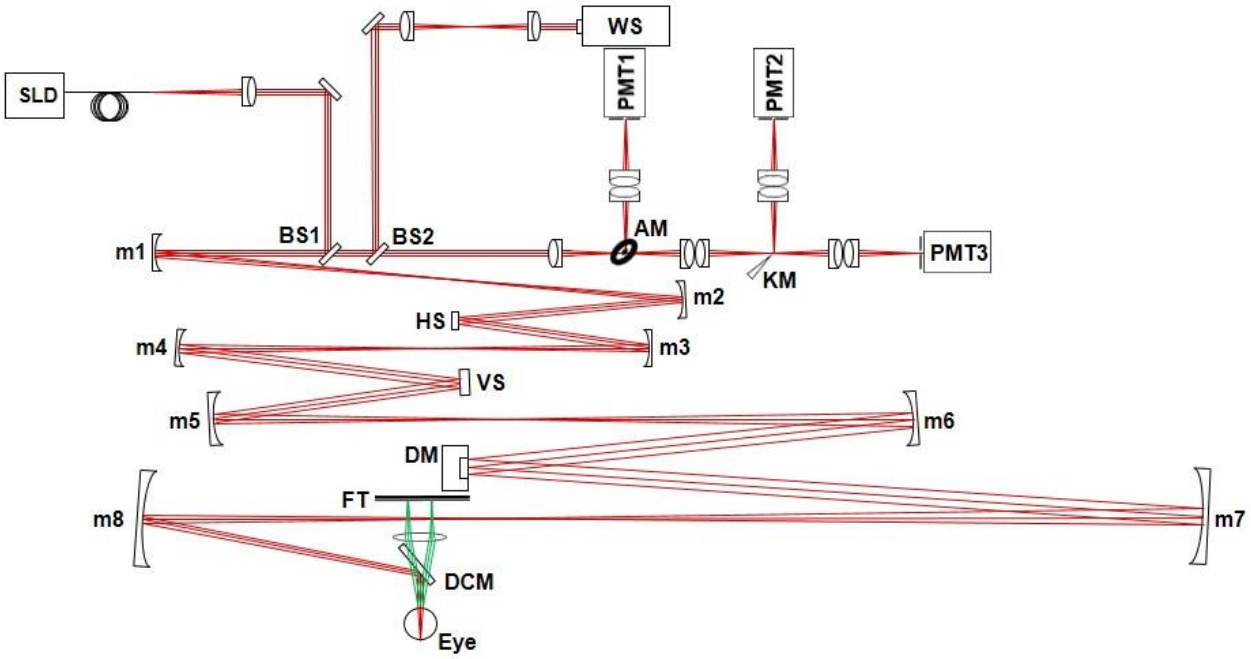

Figure 1-5. Houston AOSLO system schematic (flattened for clarity). Superluminescent diode (SLD): center wavelength of 840 nm; BS1, BS2: beam splitters; m1 ~ m8: spherical mirrors; HS: horizontal scanner; VS: vertical scanner; DM: deformable mirror (ALPAO DM97-15); DCM: dichroic mirror, reflects 750-850 nm, transmits 400-750 nm; FT: fixation target; WS: Shack-Hartmann wavefront sensor; AM: annular mirror; KM: knife-edge mirror; PMT: photomultiplier tube.

1.5 Specific aims

The overall goal of this dissertation is to provide a comprehensive picture of the foveal retina and any structural differences associated with axial elongation, thereby shedding light on the potential role of retinal stretching on foveal geometry.

1.5.1 SPECIFIC AIM 1 - Determine whether differences exist in overall foveal architecture (cone packing, FAZ, and foveal pit metrics) between healthy adult eyes with long and short axial lengths

Different factors have been proposed to influence foveal architecture and the packing of cones at the foveal center, including axial elongation (Springer & Hendrickson, 2004a; Springer & Hendrickson, 2005). Several studies have separately quantified foveal pit metrics or foveal cone density with refractive error in normal eyes (Chui et al., 2008a; Dubis et al., 2009). However, there is a general lack of data examining both foveal structure and cone density within and between eyes with short versus long axial lengths (Wilk et al., 2017). We first compared FAZ geometry, foveal pit size and cone packing between adult eyes with short and long axial lengths. We then examined whether relationships exist between foveal parameters. This study provides improved understanding of foveal architecture in the healthy adult eye and the potential role of axial elongation in determining the geometry of the fovea.

1.5.2 SPECIFIC AIM 2 - Determine whether differences exist in overall foveal structure as a function of age and refractive status in eyes of healthy children

Foveal development is a prolonged process and continues for years after birth (Yuodelis and Hendrickson, 1986, Lee et al., 2015). Many studies suggest that the development and maturation of the foveal region continue throughout childhood and into adolescence (Hendrickson et al., 2012; Vajzovic et al., 2012; Lee et al., 2015; Read et al., 2015). Hence, foveal anatomy may change with age in children. Despite the fact that the most striking structural changes in the foveal region are related to centripetal migration and maturation of cones, there is limited *in vivo* data describing cone packing in children (Park et al., 2013; Tumahai et al., 2018). Moreover, even though myopia typically occurs during childhood (i.e., juvenile myopia), most of what is known about differences in cone packing and foveal pit structure between myopic and non-myopic eyes comes from fully developed adult retinas (Chui et al., 2008a; Dubis et al., 2009). We measured and compared foveal pit size, FAZ geometry, and cone packing metrics in children of different ages and with different refractive errors. This

study provides a comprehensive, *in vivo* assessment of foveal structure in children and sheds light on whether structural changes occur due to age and myopia in children.

1.5.3 SPECIFIC AIM 3 - Determine whether differences exist in capillary geometry immediately surrounding the FAZ border as a function of axial length and FAZ structure in healthy adult eyes

The capillary network bordering the FAZ is single-layered. It is unclear whether retinal stretching associated with axial elongation or FAZ size impacts the arrangement of vasculature immediately surrounding the FAZ. While the majority of studies that have analyzed the microvascular network from *in vivo* images have quantified vessel density, the effect of axial length on macular vessel density is not well defined. Recent work suggests that parafoveal intercapillary regions (PICRs), or regions between capillaries, may be more sensitive to changes in vascular structure than vessel density (Salz et al., 2016; Schottenhamml et al., 2016; Krawitz et al. 2018). We quantified PICR metrics for those capillaries surrounding the margin of the FAZ in healthy adult eyes and determined whether PICR properties were related to an eye's axial length and/or FAZ structure. This study details microvessel geometry surrounding the FAZ and elucidates the potential impact of axial elongation or FAZ size on parafoveal capillary structure in healthy adult eyes.

CHAPTER 2

***In vivo* assessment of cone packing and foveal pit and foveal avascular zone morphometry in healthy adult eyes**

Contributing Authors:

Suman Adhikari, B Optom; Alexander W. Schill, PhD; Gwen Musial, PhD; Hope M. Queener, MS; Nimesh B. Patel, OD, PhD; Jason Porter, PhD

2.1 Introduction

The healthy adult fovea is a specialized region that is characterized by increased cone density, excavation of inner retinal layers (forming the foveal pit), and a capillary-free region, known as the foveal avascular zone (FAZ). Although this region contains only 0.3% of all cones and occupies less than 0.02% of the total retinal area (Curcio et al., 1990), approximately 40% of primary visual cortex is devoted to this region (Manson & Kandel, 1991; Hendrickson 2005), making the fovea an important component of vision. Different factors have been proposed to influence foveal architecture and the packing of cones at the foveal center, including axial elongation (Springer & Hendrickson, 2004a; Springer & Hendrickson, 2005). In addition to impacting the eye's refractive error, axial elongation can exert mechanical stretch on the posterior pole (Huang et al., 2019) and potentially lead to structural changes in cone and foveal geometries.

Several studies have separately quantified foveal cone density and other foveal metrics with refractive error in healthy adult eyes. Using techniques that bypassed the optics of the eye or compensated for the eye's optics using adaptive optics, Coletta and Watson (2006) and Rossi et al. (2007) reported reduced acuity in myopes compared to emmetropes, providing indirect evidence that foveal cones are more widely spaced (i.e., of lower density) in myopic eyes compared to emmetropic eyes. Studies that have used adaptive optics imaging to directly visualize cone photoreceptors have found that cone density is typically lower in myopes compared to emmetropes (Chui et al., 2008a; Lombardo et al., 2012) and in eyes with longer axial lengths (Li et al., 2010). In addition to examining cone properties, studies have investigated whether other foveal features are also different with axial length (Dubis et al., 2009; Tick et al., 2011; Fujiwara et al., 2017). For example, Dubis et al. (2009) found a tendency for the foveal pit to be slightly shallower and less steep in myopic eyes relative to emmetropic eyes, even though the differences were not statically significant. While these studies have improved

our understanding of foveal architecture in healthy adult eyes, many report their results in terms of refractive error, which arises due to a mismatch between an eye's axial length *and* its refractive power (i.e., is not solely due to an individual's axial length). Moreover, studies have investigated the potential role of axial elongation on *individual* foveal structures. However, less is known about cone packing in tandem with surrounding structural measurements of the fovea (FAZ and foveal pit size) in the same eyes as a function of axial length (Wilk et al., 2017). Better understanding whether relationships exist between different foveal features may shed light on anatomical bases of visual dysfunctions and also clarify models of foveal development (Wilk et al., 2017).

The main purpose of this study was to determine whether differences exist in overall foveal and cone photoreceptor geometries between healthy adult eyes with long and short axial lengths. Spectral domain optical coherence tomography images of the foveal pit and confocal and split detector adaptive optics scanning laser ophthalmoscope images of the foveal cone photoreceptor mosaic were obtained in healthy adult subjects with short and long axial lengths. Foveal pit parameters, FAZ metrics, and cone packing metrics were compared between groups. We also examined whether relationships existed between different foveal structures in each group. These results provide improved understanding of foveal architecture and the potential role of axial elongation in its geometry.

2.2 Methods

Healthy subjects, 20 to 45 years of age, with no history of eye disease or surgery were recruited to participate in the study. The study followed the tenets of the Declaration of Helsinki and was reviewed by the University of Houston Institutional Review Board. After explaining the nature of the study, informed consent was obtained from all participants. African and African-American

individuals were not included in the study because previous work has shown that they have deeper and wider foveal pits compared to Caucasians (Wagner-Schuman et al., 2011).

Each subject had a best corrected visual acuity of 20/20 or better. For each subject, the pupil of one eye was dilated using 1 drop of 1% tropicamide (Henry Schein Inc., Melville, NY USA) and 1 drop of 2.5% phenylephrine (Paragon BioTeck Inc., Portland, OR USA). Upon dilation, three autorefraction measurements were performed (ARK-510, Nidek, Gamagori, Japan) and averaged. Biometry data, including anterior corneal radius of curvature, anterior chamber depth, lens thickness, and axial length, were measured (LenStar LS 900, Haag-Streit, Koeniz, Switzerland) and were incorporated into a four surface eye model to laterally scale adaptive optics scanning laser ophthalmoscope (AOSLO) images. In the model, the posterior radius of curvature of the cornea was calculated as 0.8831 x (anterior radius of curvature of the cornea) (Williams, 1992). The refractive indices for the aqueous, lens, and vitreous were taken from LeGrand's Complete Theoretical eye (Le Grand & El Hage 1980) while the index of the cornea was assumed to be 1.38. Axial length measurements were used to classify subjects as having short (≤ 23 mm) or long (≥ 24.6) axial lengths. The criteria for the upper or lower bounds of axial length in our 2 groups were based on statistics of axial length measurements (mean ± standard deviation = 23.7 ± 0.9 mm) performed in a large population of healthy adult eyes (Oliveira et al., 2007). Eyes with axial lengths greater than or equal to one standard deviation higher than the mean (i.e., 24.6 mm = 23.7 + 0.9 mm) were considered as having long axial lengths. Conversely, eyes with axial lengths less than or equal to one standard deviation below the mean (i.e., 22.8 mm = 23.7 – 0.9 mm) were considered as having short axial lengths. However, for ease of recruitment, the upper bound for the short axial length group was relaxed to 23 mm.

2.2.1 Adaptive Optics Scanning Laser Ophthalmoscope (AOSLO) imaging & analysis

AOSLO videos were acquired in one eye of each subject over 1° and/or 1.5° field sizes. Videos were approximately 10 seconds long (250 frames) and were recorded as subjects fixated at the corners and middle of each side of the imaging raster (covering the central 3 degrees). A custom-made bite bar was used to position each subject in 3-dimensions with respect to the AOSLO's optical axis. Aberrations were measured over a dilated pupil (approximately 8 mm) at a wavelength of 840-nm (S Series Broadlighter Superluminescent Diode, S-840-B-I-20, Superlum, Carrigtwohill, Ireland; Full Width at Half Maximum = 50 nm) using a Shack-Hartmann wavefront sensor and were corrected using a deformable mirror (Hi-Speed DM97-15, ALPAO, Montbonnot-Saint-Martin, France). Light levels were kept more than 10 times below the maximum permissible exposure limit dictated by the ANSI standards (Delori et al., 2007; ANSI, 2014).

A strip-registration technique was used to remove eye motion and generate a registered image from each confocal video (Stevenson & Roorda, 2005; Dubra & Harvey, 2010). The offsets of each strip from the confocal videos were then applied to identical strips in the corresponding split detector videos and used to produce registered split detector images. Individual registered images were then stitched together (Adobe Photoshop, Adobe Systems Inc., San Jose, CA USA) to create larger montages of the cone mosaic and FAZ in each eye. A representative montage of the cone mosaic is shown in Figure 2-1.

Due to the instrument's inability to resolve the central-most foveal cones, we used a custom MATLAB program (Mathworks, Inc., Natick, MA USA) to estimate the location of peak cone density (Putnam et al., 2005), corresponding to a retinal eccentricity of 0°, as previously described (Mirhajianmoghadam et al., 2020). Cone density and spacing metrics were calculated over a square, 37 μm x 37 μm region of interest at eccentricities of 0.15, 0.2, and 0.3 mm from the foveal center along all 4 major meridians using a custom, semi-automated program (Mosaic Analytics, Translational Imaging Innovations, Hickory, NC USA) (Cooper et al., 2016). Linear

bound cone density (cones/mm^2) was calculated as the ratio of the number of bound Voronoi cells to the summed area of the bound Voronoi cells within the region of interest (Shapiro et al., 1985; Li et al., 2007). Nearest neighbor distance (NND) and farthest neighbor distance (FND) were computed as the distances (in μm) between the center of a given cone and the center of its nearest neighboring or its farthest neighboring cone, respectively. Intercell distance (ICD) was calculated as the average distance (in μm) between the center of a given cone and the centers of each of its adjacent neighbors.

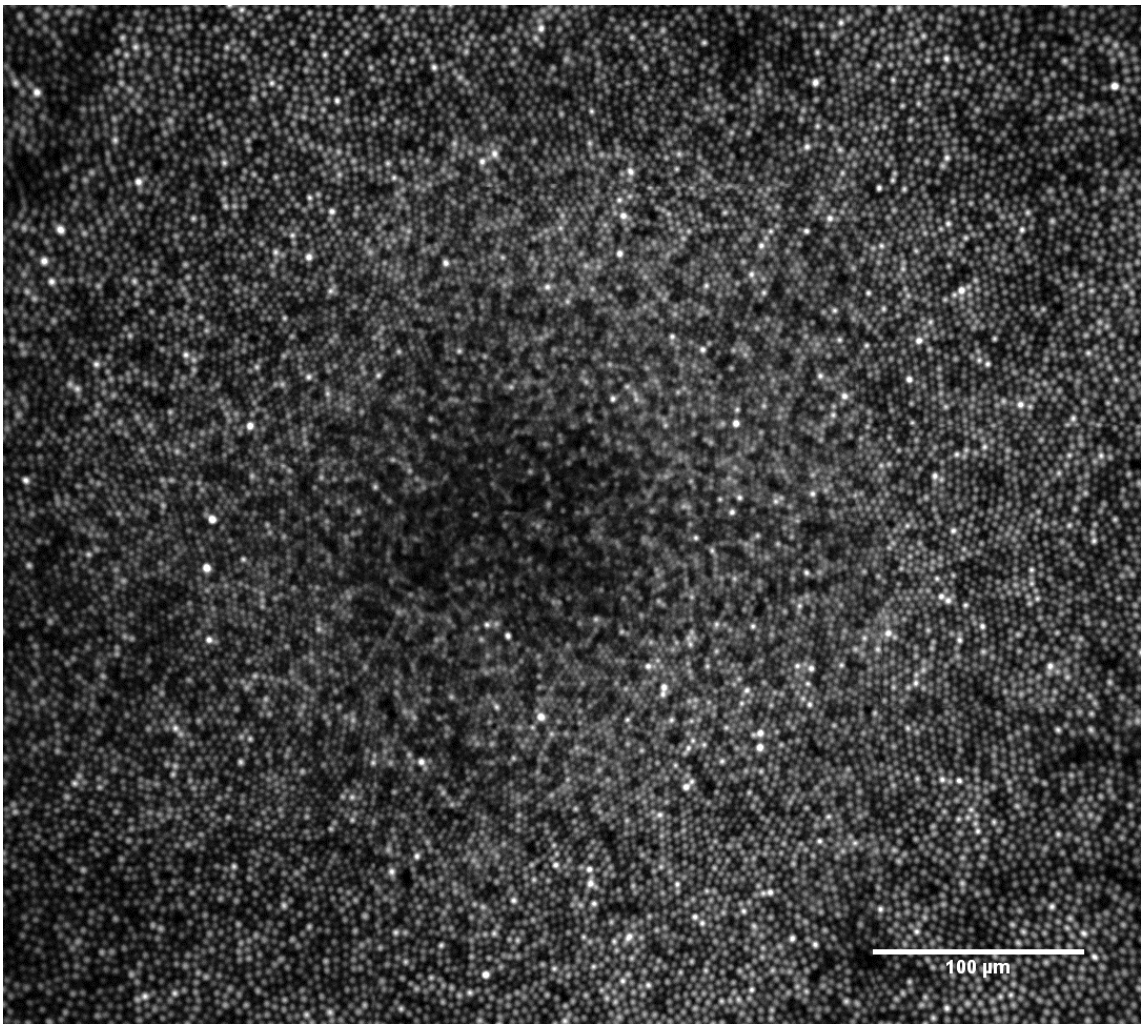

Figure 2-1. A representative montage of the foveal cone mosaic acquired in a healthy adult eye using confocal AOSLO imaging. Scale bar: 100 μm.

In order to visualize capillaries forming the border of the FAZ, the imaging plane was shifted anteriorly and AOSLO videos were recorded at a depth where the capillaries were in best focus. Subsequently, a method similar to that employed by Chui et al. (2012) was used to create perfusion images, as previously described (Mirhajianmoghadam et al. 2020). In this method, locations in the video that experience dynamic changes in intensity (such as regions where blood is actively flowing) experience larger standard errors in intensity relative to locations where intensities are more static over time (e.g., devoid of perfused vasculature). A standard error image was made for each retinal location by calculating the standard error of each pixel over 25-frame intervals, normalizing the image to its maximum value, and stretching the histogram to provide full dynamic range.

After creating registered perfusion images from each video, a montage of the perfused FAZ was created by stitching together perfusion images from different retinal locations (Adobe Photoshop, Adobe Systems Inc., San Jose, CA USA) (Figure 2-2). The border of the FAZ was manually traced three times in ImageJ to quantify mean FAZ area, perimeter, circularity, and axis ratio (Schneider et al., 2012). The area of the FAZ was calculated by multiplying the area of one pixel (mm^2) by the number of pixels inside the border of the FAZ. The perimeter of the FAZ was calculated as the total number of pixels encompassing the FAZ border in mm. Circularity was calculated as 4 pi * (area/perimeter^2). A perfect circle has a circularity of 1 while a polygon shape has a value close to 0. Axis ratio was calculated as the ratio of the major to minor axis of the ellipse best fit to the border of the FAZ.

2.2.2 Spectral Domain Optical Coherence Tomography (SDOCT) imaging & analysis

Macular cube volume scans (128 B-scans, 512 A-scans/B-scan) were acquired over the central 6 x 6 mm of the retina using the Cirrus HD-OCT (Carl Zeiss Meditec, Dublin, CA, USA). Retinal thickness data were imported into a custom MATLAB program to calculate foveal pit parameters

based on the technique introduced by Dubis et al. (2009). All measurements were corrected for each individual's axial length. First, 180 radially oriented slices were extracted through the foveal center (which was automatically determined by the OCT instrument's onboard algorithm). Retinal thickness profiles for each slice were fit with a difference of Gaussian (DoG) curve that was used to determine points involved in the calculation of foveal pit metrics. Inflection points of the first derivative of the best-fit DoG correspond to locations with maximum foveal pit slope, while zero crossing points represent locations corresponding to the peaks of the foveal rim and bottom of the foveal pit (Figure 2-3). Foveal pit diameter was quantified in each slice as the rim to rim distance and was averaged across all 180 radial slices. Foveal pit depth was quantified in each slice as the difference between the average retinal thickness of both rim locations and the retinal thickness at the bottom of the foveal pit, and subsequently averaged across slices. Foveal pit slope was quantified as the mean of the maximum slopes along the foveal contour across slices. Foveal pit volume was quantified as the volume within the space bounded by the surface of the inner limiting membrane (ILM) and a plane connecting the foveal rim points, while foveal pit area was calculated as the area contained within a plane enclosed by the foveal rim locations of all slices.

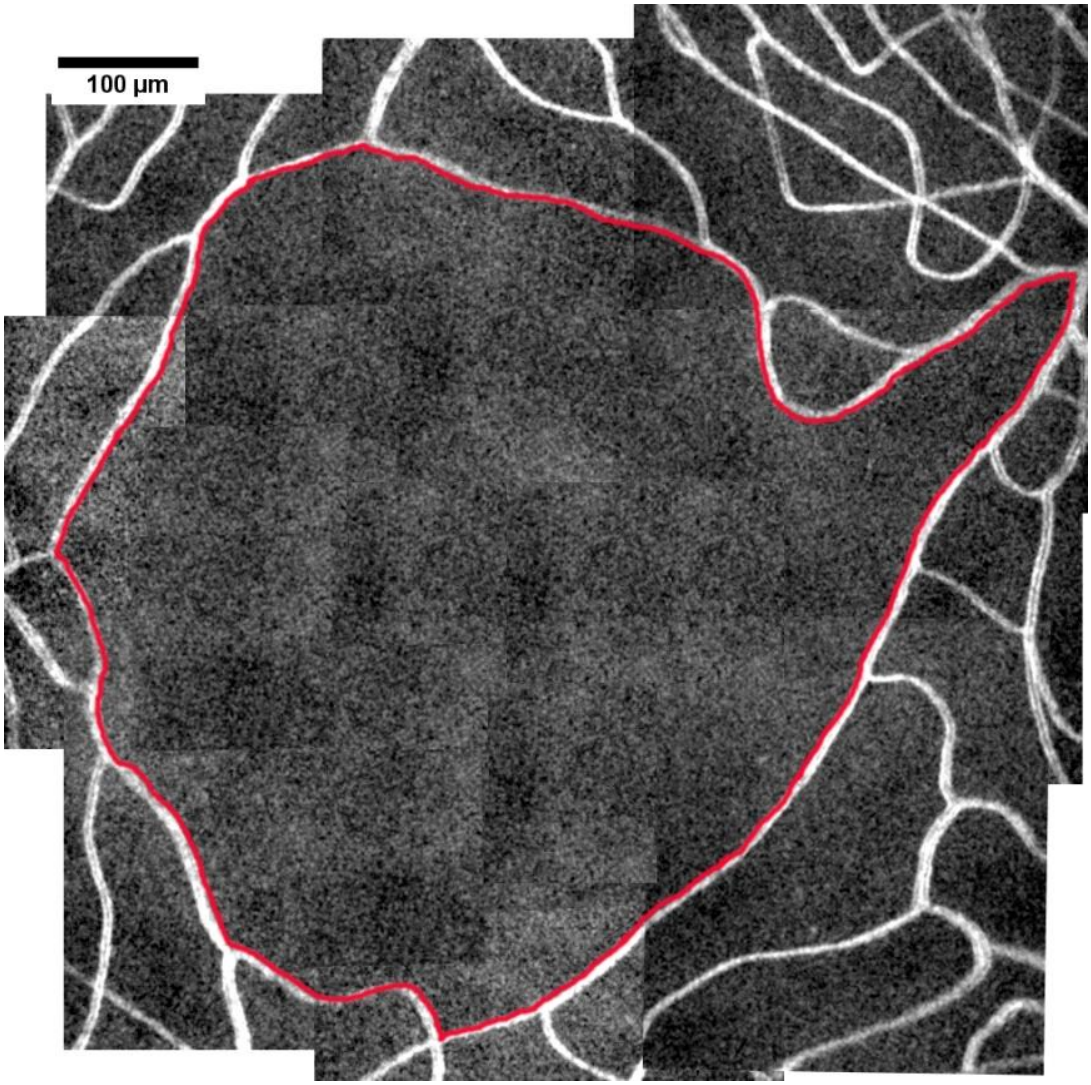

Figure 2-2. A representative montage of the perfused FAZ acquired in a healthy adult eye using split detector AOSLO imaging. The border of the FAZ was manually traced (red) using ImageJ. Scale bar: 100 µm.

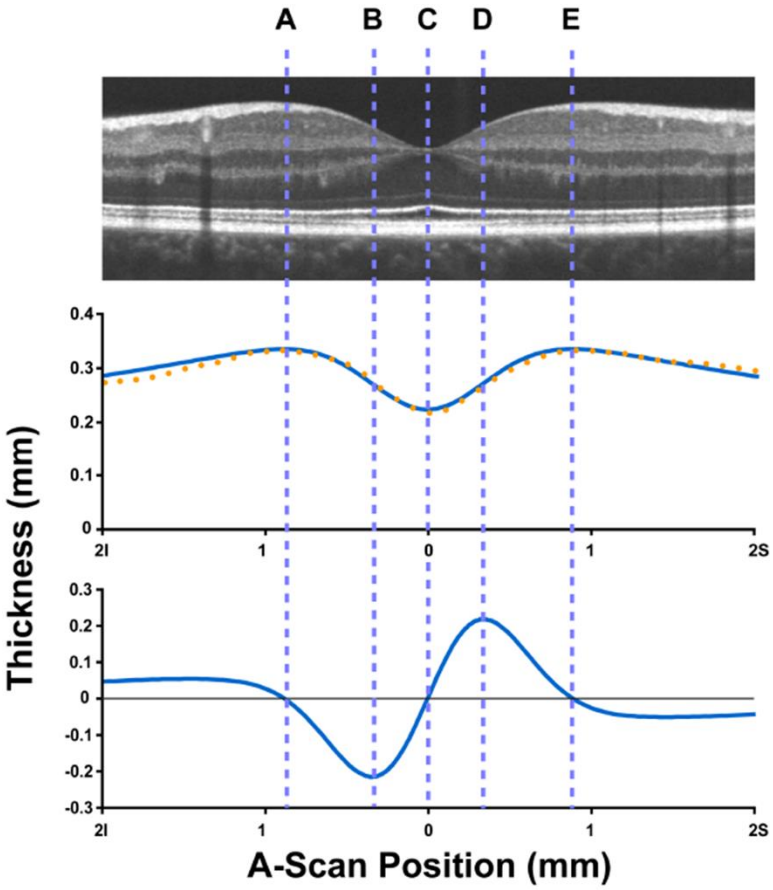

Figure 2-3. Schematic illustrating the method for quantifying foveal pit parameters from SDOCT B-scans. Top image shows a representative B-scan taken through the center of the foveal pit. Middle plot shows a trace of the Inner Limiting Membrane (ILM, orange dotted curve) marked from the above B-scan, indicating total retinal thickness, and the Difference of Gaussian (DoG) fit to the ILM (blue solid curve). Bottom plot shows the first derivative of the DoG fit that is used to calculate the following foveal pit parameters: Diameter (in mm), or rim to rim distance (AE); Depth (in µm), or distance from the straight line connecting the two rim points (AE) to the bottom of the foveal pit (along C); Slope (degrees), or maximum slope of the foveal contour as determined by the inflection points of the first derivative curve (at points B, D). Reprinted with permission (Dubis, 2012).

2.2.3 Statistical analyses

Unpaired student's T-tests were used to compare FAZ and foveal pit parameters between short and long axial length groups. To compare the main effects of axial length and eccentricity on cone density and spacing metrics (as well as the interaction effect between axial length and eccentricity), a two-way analysis of variance (ANOVA) was conducted. A Pearson correlation

was performed to determine whether significant relationships existed between cone, foveal pit, and FAZ metrics. A P value of 0.05 was considered to be statically significant. When needed, P values were adjusted to account for multiple comparisons using the Benjamini-Hochberg procedure (Benjamini & Hochberg, 1995).

2.3 Results

Twenty-six subjects were enrolled in this study. Table 2-1 summarizes subject characteristics. Subjects had a mean age (± standard deviation) of 28.0 ± 4.7 years. The short (≤ 23 mm) and long (≥ 24.6 mm) axial length groups consisted of an equal number of subjects (n=13). While there were no significant differences in the ages of subjects between groups, values of axial length and spherical equivalent refractive error were significantly different between the short axial length and long axial length groups.

Table 2-1. Demographic, axial length (AL), and refractive characteristics for all subjects enrolled in the study, and separated by short and long axial length groups (Short AL Eyes, Long AL Eyes). Data are presented as mean ± standard deviation.

	All Eyes	**Short AL Eyes (AL ≤ 23 mm)**	**Long AL Eyes (AL ≥ 24.6 mm)**	**P value**
Number of Subjects	26	13	13	-
Sex (Female/Male)	17 / 9	10 / 3	7 / 6	-
Age (years)	28.0 ± 4.7	27.4 ± 3.3	28.5 ± 5.9	0.543
Axial length (mm)	23.88 ± 1.30	22.64 ± 0.23	25.12 ± 0.37	< 0.001*
Spherical Equivalent Refractive Error (SER)	-0.94 ± 2.39	0.6 ± 1.78	-2.46 ± 1.93	0.0003*

* P < 0.05 was regarded as statistically significant

Mean foveal pit and FAZ metrics for all eyes and for both groups are shown in Table 2-2. Foveal pit metrics were not statistically different between short and long axial length groups (P > 0.05; two-tailed t-test). While there were also no significant differences in any FAZ metrics between the two groups (P > 0.05; two-tailed t-test), FAZ area and perimeter tended to be greater in eyes with longer axial lengths (P = 0.08 and P = 0.12, respectively).

Table 2-2. Mean (± standard deviation) foveal pit and foveal avascular zone (FAZ) parameters in all healthy adult eyes, and in short and long axial length groups.

	All Eyes	Short AL Eyes	Long AL Eyes	P value
Foveal Pit Metrics				
Pit volume (mm^3)	0.094 ± 0.027	0.103 ± 0.023	0.085 ± 0.029	0.10
Pit area (mm^2)	3.022 ± 0.557	3.116 ± 0.558	2.928 ± 0.563	0.40
Pit diameter (mm)	1.930 ± 0.189	1.970 ± 0.168	1.890 ± 0.207	0.29
Pit depth (mm)	0.109 ± 0.033	0.113 ± 0.026	0.105 ± 0.038	0.52
Pit slope (degrees)	11.4 ± 3.3	11.6 ± 3.4	11.3 ± 3.4	0.83
FAZ Metrics				
FAZ area (mm^2)	0.29 ± 0.12	0.25 ± 0.10	0.33 ± 0.12	0.08
FAZ perimeter (mm)	2.40 ± 0.52	2.24 ± 0.43	2.56 ± 0.57	0.12
FAZ circularity	0.62 ± 0.14	0.62 ± 0.15	0.63 ± 0.12	0.87
FAZ axis ratio	1.21 ± 0.12	1.22 ± 0.13	1.20 ± 0.12	0.59

Mean values of cone metrics for the short and long axial length groups are shown in Figure 2-4. Table 2-3 presents the results of two-way ANOVAs that were performed to examine the effects of eccentricity and axial length group (as well as their interaction) on cone density and spacing metrics. Results showed significant differences for the main effects of eccentricity and axial length group on linear cone density, farthest neighbor distance, and intercell distance ($P < 0.001$ for all), as well as nearest neighbor distance ($P = 0.02$), indicating that linear cone density (Figure 2-4A) was significantly lower and cone spacing (farthest neighbor, intercell, and nearest neighbor distances, Figures 2-4B-D) was significantly higher in the long axial length group relative to the short axial length group across all eccentricities examined. However, the lack of a significant interaction precluded the assessment of whether differences in cone metrics exist between groups at individual eccentricities. A Bonferroni post-hoc analysis showed that linear cone density was significantly higher at an eccentricity of 0.15 mm compared to 0.2 mm ($P = 0.007$), and at an eccentricity of 0.2 mm compared to 0.3 mm ($P < 0.001$) across axial length groups. Post-hoc analysis also determined that intercell distance and nearest neighbor distance (Figure 2-4C,D) were significantly lower across groups at an eccentricity of 0.15 mm compared to 0.2 mm ($P = 0.03$ and $P = 0.001$, respectively), and at an eccentricity of 0.2 mm

compared to 0.3 mm ($P < 0.001$ for both). Farthest neighbor distance was significantly lower only at an eccentricity of 0.2 compared to 0.3 mm (Bonferroni post-hoc, $P < 0.001$).

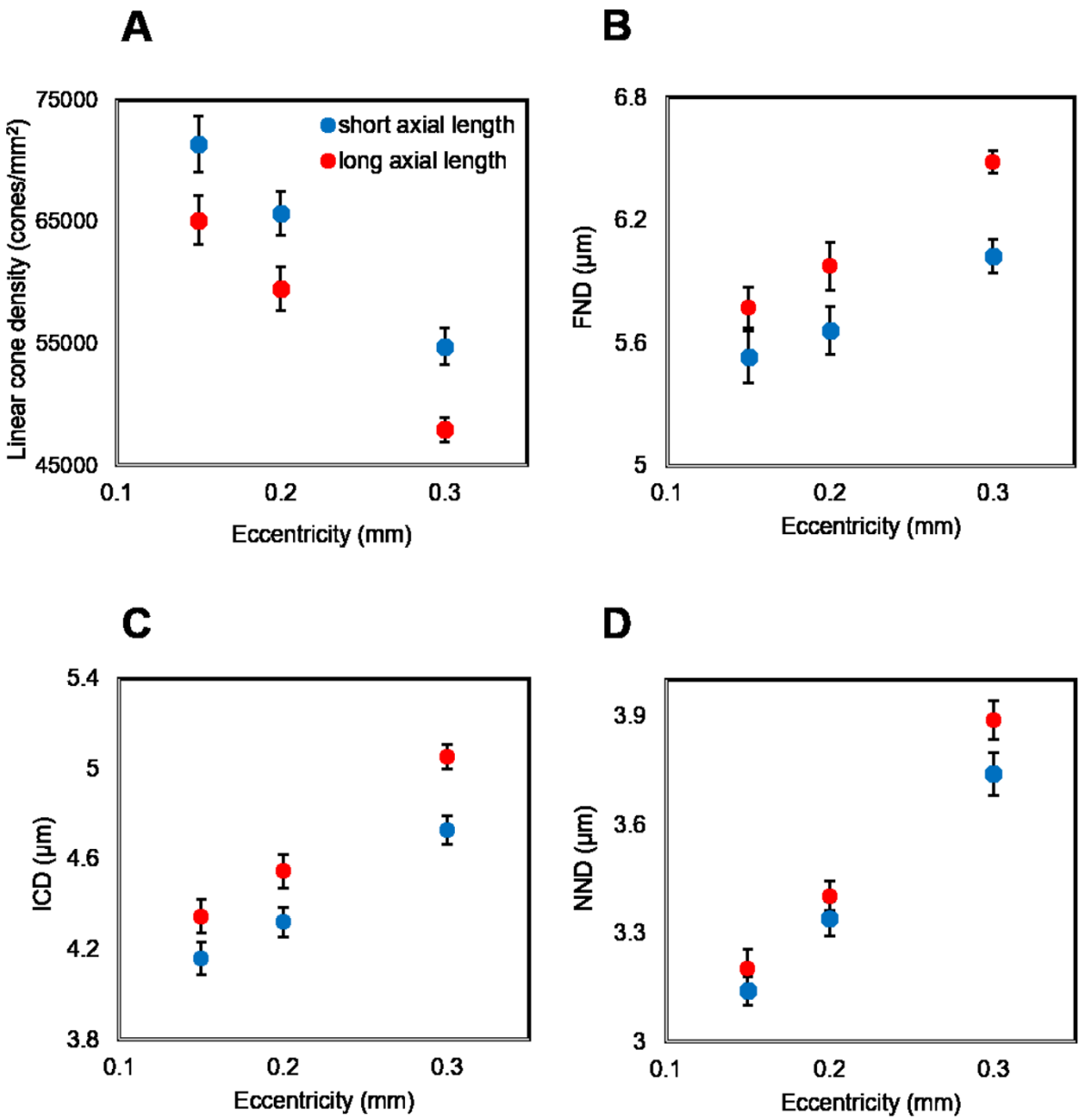

Figure 2-4. Cone photoreceptor metrics as a function of eccentricity for short (blue) and long (red) axial length groups. Filled circles represent the mean values for each group. Error bars represent ± 1 standard error of the mean. (A) Linear cone density was significantly lower in the long axial length group across all eccentricities. (B) Farthest neighbor distance (FND), (C) intercell distance (ICD), and (D) nearest neighbor distance (NND) were significantly higher in the long axial length group across all eccentricities.

Table 2-3. Main effects and interaction effects of eccentricity and axial length group on cone density and spacing metrics.

	P value			
	Linear cone density	**Farthest neighbor distance**	**Nearest neighbor distance**	**Intercell distance**
Main effect of eccentricity	<0.001*	<0.001*	<0.001*	<0.001*
Main effect of axial length group	<0.001*	<0.001*	0.02*	<0.001*
Interaction effect of eccentricity x axial length group	0.98	0.58	0.59	0.55

* P < 0.05 was regarded as statistically significant

We also examined whether relationships existed between FAZ, foveal pit, and cone parameters within each group of eyes. After correcting for multiple comparisons, eyes with larger FAZ areas in the long axial length group also had significantly larger foveal pit areas (r = 0.74, P = 0.004), foveal pit diameters (r = 0.75, P = 0.003), and foveal pit volumes (r = 0.74, P = 0.004) (Figure 2-5). However, no relationships between FAZ and foveal pit parameters were seen in the short axial length group after adjusting for multiple comparisons. In addition, cone density was not correlated with FAZ area or foveal pit volume in short or long axial length groups.

2.4 Discussion

The main purpose of this study was to examine whether differences exist in overall foveal geometry, cone density, and cone spacing between healthy adult eyes with short and long axial lengths. We also sought to determine whether relationships exist between foveal parameters. Foveal pit and FAZ metrics were not significantly different between short and long axial length groups. Linear cone density was significantly lower, while nearest neighbor distance, farthest neighbor distance, and intercell distance were significantly higher, in the long axial length group across all eccentricities. Eyes with larger FAZ areas had larger foveal pit volume, area, and

diameter only for those within the long axial length group.

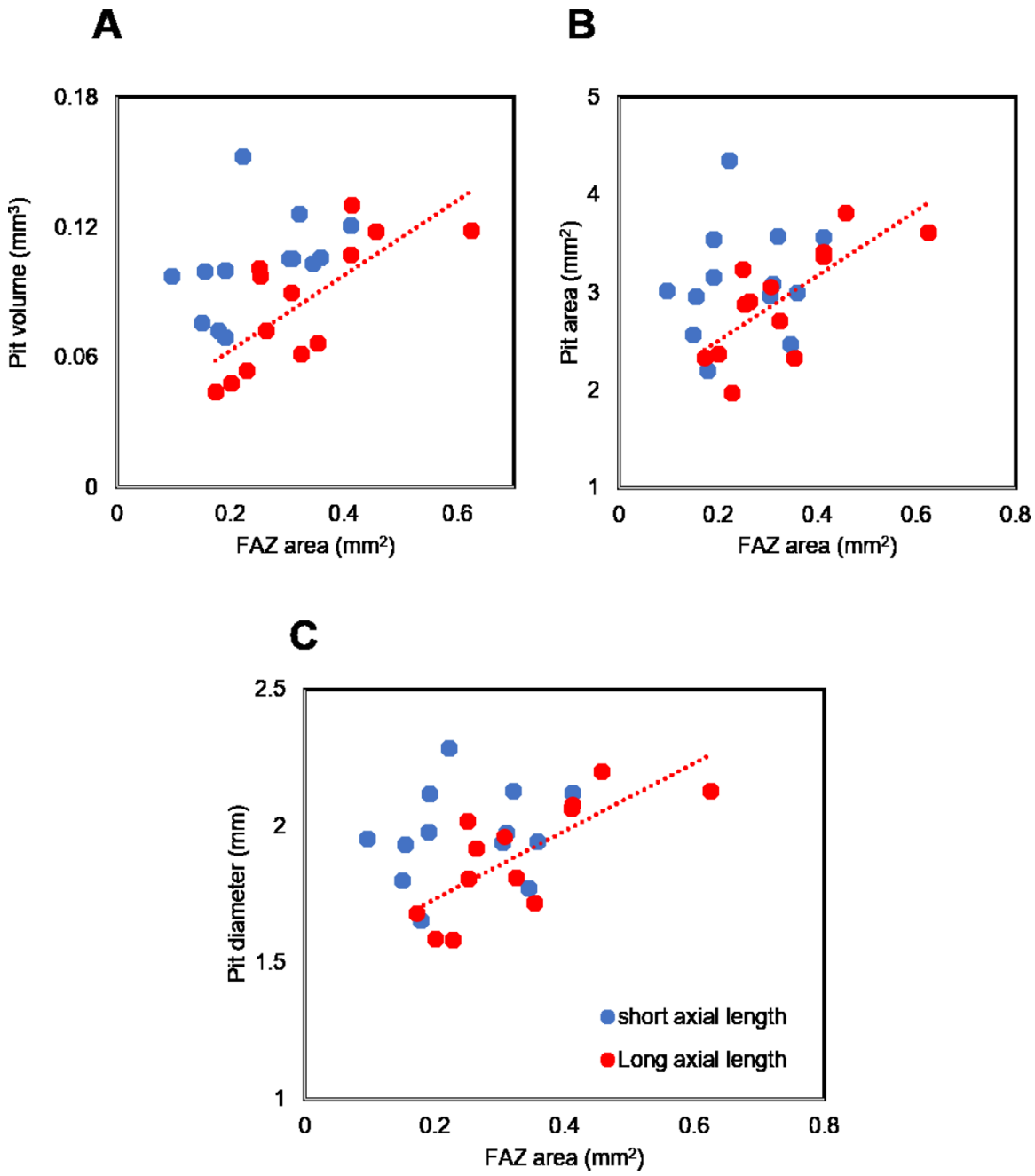

Figure 2-5. Comparison between FAZ area and (A) foveal pit volume, (B) foveal pit area, and (C) foveal pit diameter for all eyes within short (blue) and long (red) axial length groups. Filled circles represent individual eyes. Dotted lines show linear regressions that are statistically significant. Foveal pit volume, area, and diameter all increase with increasing FAZ area only for eyes in the long axial length group.

The fact that some foveal metrics were different between axial length groups (i.e., cone density and spacing) while others were not (i.e. FAZ and foveal pit metrics) suggests that different factors determine the adult-like geometry of different foveal structures. The decreased cone densities and increased cone spacings measured in the long axial length group suggest that axial elongation plays a role in determining cone distribution across individuals. Despite finding no differences in FAZ and foveal pit metrics between axial length groups, it is still possible that axial elongation could also impact foveal structure. For example, the effect of axial elongation on the foveal pit could be offset and/or confounded by genetic factors, as studies have demonstrated the heritability of retinal traits in healthy eyes (Han et al., 2017).

Multiple factors can influence the morphometric shape of the foveal pit. We found no differences in foveal pit metrics between eyes in short and long axial length groups. This result is consistent with an earlier study that reported no significant differences in foveal pit metrics between emmetropic and myopic eyes (Dubis et al., 2009). While Dubis et al. (2009) presented the first *in vivo* quantification of foveal pit metrics when modeling the pit in three-dimensions, the study did not report the racial make-up of its subjects. A subsequent study from the same lab (Wagner-Schuman et al., 2011) found that foveal pit geometry does differ between eyes from different races (i.e., Caucasians versus African-Americans). Based on this result, we restricted the racial/ethnic groups that participated in this study to minimize variability. In addition, axial length is another factor with the potential to influence the size and shape of the pit. Many studies approaching this topic have grouped subjects based on refractive error. Even though axial length is a main determinant of refractive error (Curtin, 1985; Young et al., 2007; Hou et al., 2018), refractive error is generated due to a mismatch between the eye's refractive power and axial length. Therefore, it is possible that eyes with the same refractive error could have different axial lengths (and vice versa), potentially confounding the effects of axial elongation on retinal structure. Consequently, we chose to focus on axial length alone to minimize potential

variability that could be present with refractive error and lend insights into the potential role of retinal stretching on foveal geometry. Tick et al. (2011) investigated the effect of axial elongation on pit metrics using OCT imaging and reported a negative correlation between foveal pit diameter and axial length. However, scans were not scaled based on each subject's axial length, which complicates any interpretation.

Foveal avascular zone metrics were not significantly different between short and long axial length groups. Among various metrics of FAZ morphometry, FAZ area has been most widely investigated. Consistent with previous studies (Chui et al., 2014; Fujiwara et al., 2017; Wen et al., 2019), we found no correlation between axial length and FAZ area. Outside of area, much less is known about other morphological metrics of the FAZ and their relationship with axial length. Hence, we additionally quantified FAZ perimeter, circularity, and axis ratio, as there is currently no ideal metric for assessing FAZ structure (Linderman et al., 2018). Regardless, these additional metrics were also not significantly different between the axial length groups.

Across all eccentricities examined, eyes in the long axial length group had decreased linear cone density and increased values of nearest neighbor, farthest neighbor, and intercell distances relative to the short axial length group. These findings suggest that retinal stretching due to axial elongation may affect cone photoreceptor packing over the region analyzed. Given that the total number of cone photoreceptors are determined before birth (Young, 1985; Rich et al., 1997) and that the total number of foveal cones are relatively similar between individuals (Curcio et al., 1990; Zhang et al., 2015), it is possible that foveal cones could be less tightly packed in eyes with longer axial lengths as they attempt to cover a larger retinal area. Similar to results found by Chui et al. (2008a) and Lombardo et al. (2012) when comparing myopic to emmetropic eyes, we found decreased cone densities in the long axial length group compared to the short axial length group. The closest eccentricities at which cone densities were measured by Chui et al. (2008a) and Lombardo et al. (2012) were 0.3 mm and 0.26 mm,

respectively. In our study, we quantified cone metrics closer to the foveal center (0.15 mm), but were unable to image cones closer than this eccentricity in all eyes. Li et al. (2010) reported cone density measurements in 18 healthy adult eyes at eccentricities as close as 0.1 mm and observed a significant decrease in linear cone density with increasing axial length starting at an eccentricity of 0.3 mm. The lack of significant interaction between the axial length group and eccentricity in this study precluded us from comparing cone density between the two axial length groups at each eccentricity. It is of note that the relationship between axial length and cone density at these eccentricities cannot be extrapolated to the foveal center (location of peak cone density) as retinal stretching may not be uniformly distributed across the retina (Chui et al., 2008a).

While cone density was not related to foveal pit volume or FAZ area in this study, eyes with larger FAZ areas in the long axial length group tended to possess larger pit volumes, areas, and diameters. Springer and Hendrickson (2004a) proposed a model for foveal development based on a series of finite element analyses. They suggest that forces, such as intraocular pressure (IOP) and growth-induced retinal stretch, exert increased pressure on retinal areas that are more elastic and malleable than the surrounding tissue (such as the FAZ) and may account for foveal pit formation, as well as for the centripetal migration of cones toward the foveal center. Based on this model, one should expect a relationship to exist between the size of the FAZ, foveal pit geometry, and foveal cone density. Consistent with previous studies (Dubis et al., 2012; Wilk et al., 2017), we observed a positive correlation between FAZ area and foveal pit shape and size. Although Springer and Hendrickson's model of foveal development suggests that the presence of the pit is necessary for increased packing of the cones at the foveal center, we did not find cone density to be correlated with FAZ area or pit volume at any eccentricity. Likewise, Wilk et al. (2017) did not find any relationship between peak cone density and foveal pit volume. In aggregate, the lack of relationship between cone density and foveal pit

size reported in our *in vivo* study of adult retinas, as well as in other studies (Wilk et al., 2017), runs contrary to the structural changes predicted by Springer and Hendrickson's finite element analysis model. However, it is important to note that these *in vivo* studies were performed in adult retinas that had already matured. Therefore, we cannot rule out the possibility that the finite element analysis modeling may be relevant to the development of the foveal pit and not necessarily to its maturation.

In conclusion, we examined and compared overall foveal geometry (FAZ, foveal pit, and cone structure) between healthy adult eyes with short and long axial lengths. Cone density and spacing were significantly different between long and short axial length groups, while FAZ and foveal pit metrics were not. The results suggest that the distribution of cones over the regions analyzed in this work is affected by retinal stretching due to axial elongation, whereas FAZ and foveal pit geometry are primarily driven by other factors.

2.5 Acknowledgements

This research was supported by National Institutes of Health (NIH) Grant P30 EY007551 and the University of Houston College of Optometry (Student Vision Research Support Grant). The authors thank Mindy Fox for her contribution in data collection. We also thank Joseph Carroll for providing the MATLAB code to analyze foveal pit parameters and Joseph Carroll and Robert Cooper for providing Mosaic Analytics.

CHAPTER 3

***In vivo* assessment of foveal geometry and cone photoreceptor density and spacing in children**

Citation:

Mirhajianmoghadam H, Jnawali A, Musial G, Queener HM, Patel NB, Ostrin LA, Porter J. *In vivo* assessment of foveal geometry and cone photoreceptor density and spacing in children. *Sci Rep* 2020;10:8942

3.1 Introduction

The healthy human adult fovea is a specialized retinal region that provides high spatial sampling of the retinal image (Hirsch & Curcio, 1989; Rossi & Roorda, 2010). The fovea is typically characterized anatomically by increased cone density, excavation of inner retinal layers (forming the foveal pit), and a capillary-free region known as the foveal avascular zone (FAZ). Although the location of the fovea can be identified as early as 11 weeks gestation (Provis et al., 1998) by a single layer containing only cones (Provis, 1985; Hendrickson, 1992), the fovea undergoes substantial changes, both *in utero* and *ex utero*, including thinning and elongation of cone inner and outer segments (Hendrickson & Yuodelis, 1984; Yuodelis & Hendrickson, 1986; Hendrickson et al., 2012), photoreceptor migration toward the foveal center (Yuodelis & Hendrickson, 1986), the formation of Henle's fiber layer (Hendrickson & Yuodelis, 1984), remodeling of the FAZ (Provis & Hendrickson, 2008), and a widening and shallowing of the foveal pit (Hendrickson et al., 2012; Springer & Hendrickson, 2005).

Despite the formation of an identifiable fovea before birth, foveal development is a protracted process. While some aspects of the fovea are reported to mature at an early age, such as the size of the FAZ (Provis & Hendrickson, 2008; Hendrickson et al., 2012), many studies suggest that the development and maturation of the fovea continues throughout childhood and into adolescence (Hendrickson et al., 2012; Vajzovic et al., 2012; Bruce et al., 2013; Read et al., 2015; Lee et al., 2015). Age-related differences in the thicknesses of retinal layers have been broadly investigated *in vivo* in children. While the majority of changes are thought to occur within the first few years of life (Hendrickson & Yuodelis, 1984), more recent studies report increases in the thicknesses of the outer nuclear layer (Lee et al., 2015) and outer retinal layers in the foveal region until at least 12 years of age (Read et al., 2015). Reports of age-related differences in cone density are sparse. Yuodelis and Hendrickson (Yuodelis & Hendrickson, 1986) examined 5 eyes histologically after birth and found that peak cone density

at birth was only 17% of the value measured in their 37 year-old adult eye. In addition, they found that peak cone density in a 45 month-old donor eye was only half of that in the 37 year-old eye.

Few studies have quantified cone density and FAZ metrics *in vivo* in children. Park et al. (2013) and Tumahai et al. (2018) performed adaptive optics imaging of cone photoreceptors in groups of children and adults between the ages of 10-20 years and 6-20 years, respectively, at eccentricities as close as 0.5 mm and 0.45 mm from the foveal center, respectively. Despite these efforts, cone density and spacing values have yet to be described for eccentricities closer than 0.45 mm (approximately 1.5°) from the fovea in a cohort of subjects who are only children. In another study, FAZ area was quantified in 26 eyes between the ages of 10 and 19 years using optical coherence tomography angiography (Fujiwara et al., 2017). However, data detailing other FAZ metrics have yet to be described only in children (particularly for those under 10 years of age) (Yanni et al., 2012; Fujiwara et al., 2017). Furthermore, there is a lack of *in vivo* data in children detailing a more comprehensive examination of overall foveal morphometry that incorporates measurements of cone density with other structural measures, such as the size of the FAZ and the foveal pit, in the same eyes.

In addition, differences in foveal cone structure are not well-described in children with different refractive errors. The prevalence of myopia continues to grow worldwide (Vitale et al., 2009; Holden et al., 2016). In the United States, approximately 60% of new myopic cases are classified as school age onset (or juvenile) myopia, typically presenting in children between 9 to 11 years of age and progressing through the early teenage years (Gilmartin, 2004). However, most of what is known about differences in cone density and foveal pit shape between myopic and non-myopic retinas comes from studies performed in fully-developed adult retinas. Cone density has been shown to be significantly lower in myopic compared to non-myopic adult eyes (Chui et al., 2008a; Lombardo et al., 2012), and no significant differences have been observed

in the diameter, depth, and slope of the foveal pit between myopic and emmetropic subjects aged 13 to 52 years old (Dubis et al., 2009). Therefore, the main purpose of this study was to determine whether overall foveal structure, including cone density and spacing, FAZ size, and foveal pit shape, differs as a function of age and refractive status in children. This work yields a better understanding of overall foveal morphometry in children and provides insights into mechanisms of ocular growth.

3.2 Methods

Healthy children, 5.8 to 15.8 years of age, were recruited to participate in this study. After explaining the nature of the study, informed consent for study participation was acquired in the form of written informed assent from all children and written permission from all parents. The study followed the tenets of the Declaration of Helsinki and was approved by the University of Houston Institutional Review Board.

Children underwent a comprehensive vision examination to determine ocular refraction, best corrected visual acuity, biometry, and ocular health status. All children had a best corrected visual acuity of 20/20 or better. Both eyes were dilated using 1% tropicamide (Henry Schein Inc., Melville, NY USA) and 2.5% phenylephrine (Paragon BioTeck Inc., Portland, OR USA). Upon dilation, autorefraction was performed (WAM-5500, Grand-Seiko, Hiroshima, Japan); at least five measurements were taken and averaged for each eye. The refractive status for each child was determined from the average spherical equivalent refractive error (SER) of the examined eye, and was classified as myopic (cycloplegic SER ≤ -0.50 D) or non-myopic (cycloplegic SER > -0.5 D).

3.2.1 Ocular biometry and image scaling

Axial length, anterior corneal radius of curvature, corneal thickness, anterior chamber depth, and lens thickness were measured in each eye using an ocular biometer (LenStar LS 900, Haag-Streit, Koeniz, Switzerland). Biometry data were used to laterally scale adaptive optics scanning laser ophthalmoscope (AOSLO) and spectral domain optical coherence tomography (SDOCT) images using a four surface eye model. The refractive index of the cornea was taken to be 1.38 (Patel et al., 1995), and the posterior radius of curvature of the cornea was modeled after Williams(Williams, 1992) to be 0.8831 x (anterior radius of curvature of the cornea). The schematic eye model was modified for children by incorporating previously published values of the anterior and posterior radii of curvatures of the lens based on the age of each child using the following equations (Mutti et al., 1998):

$$lens\ anterior\ radius\ of\ curvature\ (mm) = -0.021x^2 + 0.151x + 11.45 \quad (1)$$

$$lens\ posterior\ radius\ of\ curvature\ (mm) = 0.004x^2 + 0.063x + 6.236 \quad (2)$$

where x is the (age in years – 10). The refractive indices for the aqueous, lens, and vitreous were taken from LeGrand's Complete Theoretical eye (Le Grand & El Hage, 1980).

3.2.2 Spectral Domain Optical Coherence Tomography (SDOCT) Imaging & Analysis

High resolution volume scans centered on the macula (97 B-scans, 1024 A-scans/B-scan) were acquired over a 20° x 20° field in the right eye of each child using spectral domain optical coherence tomography (SDOCT; Spectralis HRA+OCT, Heidelberg Engineering, Heidelberg, Germany) and used to calculate foveal pit parameters (Fig. 3-1). SDOCT and AOSLO images could not be acquired with sufficient quality in the right eye of 4 subjects due to poor fixation. Therefore, images were acquired from the left eyes of these subjects for both modalities and used for the study.

The internal limiting membrane and Bruch's membrane were automatically delineated in each SDOCT B-scan using the instrument's onboard segmentation algorithm and confirmed by

visual inspection. Segmented B-scans were imported into a custom MATLAB program (Mathworks, Inc., Natick, MA USA) to generate retinal thickness maps, from which 24 radially oriented slices (each separated by 15°) were interpolated through the center of the fovea and smoothed. For each radial slice, the difference in retinal thickness between adjacent points along the smoothed profile (i.e. the numerical derivative) was calculated to determine the slope of the foveal contour. Locations with a numerical derivative of zero corresponded to the peaks of the foveal rim and the bottom of the foveal pit within each radial slice. The pit diameter for a single radial slice was defined as the distance between the peak locations of the foveal rim on both sides of the pit (Fig. 3-1). Mean foveal pit diameter for each eye was calculated as the average pit diameter across all 24 radial slices. Foveal pit depth within each slice was calculated as the difference between the mean retinal thickness of both peak rim locations and the retinal thickness at the bottom of the foveal pit. Mean foveal pit depth for each eye was calculated as the average pit depth across all 24 radial slices. Mean foveal pit slope was calculated for each eye as the average of the maximum slopes between the foveal rims and the bottom of the pit across all radial scans. Using the retinal thickness maps for each eye, we identified locations along the foveal contour within the pit that had heights corresponding to 10-70% of the mean foveal pit depth in 2% increments. For each interval, an ellipse was fit to the points with the same percent height. The centers of the 30 fitted ellipses were averaged and used to determine the mean center of the foveal pit. Foveal point thickness (Read et al., 2015) was calculated as the retinal thickness at the mean center of the foveal pit.

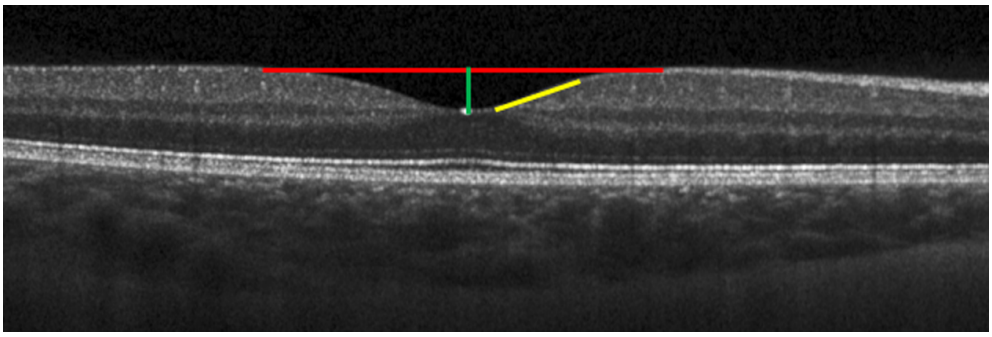

Figure 3-1. Representative SDOCT B-scan acquired through the center of the fovea and used to calculate foveal pit metrics, including foveal pit diameter (red line), foveal pit depth (green line), and foveal pit slope (yellow line).

3.2.3 Adaptive Optics Scanning Laser Ophthalmoscope (AOSLO) Imaging & Analysis

Cone photoreceptors and the foveal avascular zone (FAZ) were also imaged in a subset of children using an AOSLO (Ivers et al., 2011). A custom bite bar was made for each child and attached to a 3-dimensional translation stage to align the child's pupil with the optical axis of the instrument and to minimize head movements during image acquisition. Children were instructed to view a digitally controlled fixation target presented at different locations within the AOSLO system. The fixation light was moved from the foveal center (0°) to a retinal eccentricity of 2° in 0.5° steps in multiple directions to acquire images over a roughly 4° x 4° patch of retina, centered on the fovea. At each retinal location, aberrations were measured over a dilated pupil (approximately 8 mm) at a wavelength of 840-nm (S Series Broadlighter Superluminescent Diode, S-840-B-I-20, Superlum, Carrigtwohill, Ireland; Full Width at Half Maximum = 50 nm) using a Shack-Hartmann wavefront sensor and were corrected using a deformable mirror (Hi-Speed DM97-15, ALPAO, Montbonnot-Saint-Martin, France). Light levels for aberration correction and imaging (peak power of ~300 μW at the corneal plane) were more than 10 times below the maximum permissible exposure established by the ANSI standards (Delori et al., 2007; ANSI, 2014).

Confocal and split detector videos of cone photoreceptors and retinal vasculature comprising the FAZ were simultaneously collected over a 1° or 1.5° field of view at a rate of 25 Hz at each retinal location. After correcting for scan distortions, a strip-registration technique was used to remove inter- and intra-frame eye motion, and create a stabilized video and registered image for each confocal video (Stevenson & Roorda, 2005; Dubra & Harvey, 2010). The same offsets were then applied to identical strips from each frame in the corresponding split detector video to generate stabilized split detector videos.

Montages of the cone mosaic were generated by manually stitching individual confocal registered images using Adobe Photoshop (Adobe Systems Inc., San Jose, CA USA). A representative example of a montage of the cone mosaic from a 6-year old child is shown in Figure 3-2A. Because it was not possible to resolve the central-most foveal cones in all subjects to identify the location of peak cone density (i.e., the location with a retinal eccentricity of 0°), we used a technique developed by Putnam et al. (2005) to estimate the location of peak cone density. In brief, a custom MATLAB program was used to semi-automatically mark all resolved cones within the central 3° of the fovea (Li & Roorda, 2007) and generate a topography map of cone density values. Separate ellipses were then fit to locations in the foveal mosaic that contained 65-70%, 71-75%, and 76-85% of the maximum cone density measured in the montage. The centers of these 3 ellipses were averaged to estimate the location of peak cone density.

A custom, semi-automated program (Mosaic Analytics, Translational Imaging Innovations, Hickory, NC USA)(Cooper et al., 2016) was used to calculate cone metrics within a 37 x 37 μm sampling window at eccentricities of 0.2 mm, 0.3 mm, and 0.5 mm from the foveal center along all 4 major meridians. Linear and angular bound cone densities (cones/mm^2 and cones/deg^2, respectively) were calculated as the ratio of the number of bound Voronoi cells to the summed area of the bound Voronoi cells (Shapiro et al., 1985; Li & Roorda, 2007). Farthest

neighbor distance was calculated as our spacing metric, as Cooper et al. (2016) found this metric to be most sensitive to a change in the total number of cones marked within an image out of the four metrics that were examined (including density recovery profile distance, nearest neighbor distance, farthest neighbor distance, and intercell distance). Farthest neighbor distance was calculated as the distance (in μm) between a given cone and its farthest neighbor, where the neighbors of a given cone are comprised of all cones within adjacent Voronoi cells. Cone metrics were averaged across all 4 meridians for analyses performed across all eyes (regardless of refractive error). For analyses examining the impact of different meridians on cone density and spacing, metrics were averaged along the horizontal meridian (nasal, temporal) and vertical meridian (superior, inferior) separately.

AOSLO videos of inner retinal vasculature were acquired by shifting the focal plane anteriorly to a plane where the capillaries were in best focus. After correcting for scan distortions and stabilizing videos, perfusion images were created using a method similar to that employed by Chui et al. (2012). This technique is based on the premise that the largest changes of intensity (or greatest standard errors) occur over time in regions of the video where blood is actively flowing as opposed to retinal regions that are more static in their structure (e.g., devoid of perfused vasculature). Motion-corrected videos were normalized to the maximum intensity value of any pixel in the video and were median filtered using a 3 x 3-pixel kernel to reduce noise. Each 150- to 250-frame filtered video was divided into 25-frame intervals in order to limit the influence of slower (less than 0.5 Hz) tissue reflectance changes on the perfusion image. The standard-error of each pixel over the 25-frames was computed as the standard error frame, which was subsequently median filtered by a 3 x 3-pixel kernel. All available filtered standard-error frames were averaged to produce a standard-error image. This image was then normalized to its maximum value and histogram-stretched so that the lower and upper 1% of the histogram were set to 0 and 255, respectively.

Registered perfusion images were stitched together using Adobe Photoshop to create a montage of the perfused FAZ (Fig. 3-2B). The border of the FAZ was semi-automatically traced two times using the NeuronJ plug-in for ImageJ (Meijering et al., 2004). The coordinates of the border were then imported into in a custom MATLAB program to quantify FAZ metrics. The area of the FAZ was calculated by multiplying the area of one pixel (in mm^2) by the number of pixels enclosed by the border of FAZ. The perimeter of the FAZ was calculated as the total length of the FAZ border (in mm). Axis ratio was calculated as the ratio of the length of the major axis to that of the minor axis of an ellipse best-fit to the border of the FAZ. Effective diameter (in µm) was defined as the diameter of a circle with an area equivalent to the calculated FAZ area. Circularity was calculated as:

$$Circularity = 4\pi\left(\frac{area}{perimeter^2}\right) \quad (3)$$

where a value of 1 indicates a perfect circle and a value closer to 0 indicates a polygon shape. Acircularity index measures the degree of irregularity in the overall shape of the FAZ and was calculated as the ratio of the FAZ perimeter to the perimeter of a circle with an area that is equal to the FAZ area (Tam et al., 2011). A perfectly circular FAZ has an acircularity index of 1. The value of the acircularity index increases with increasing deviation of the shape of the FAZ from a circle.

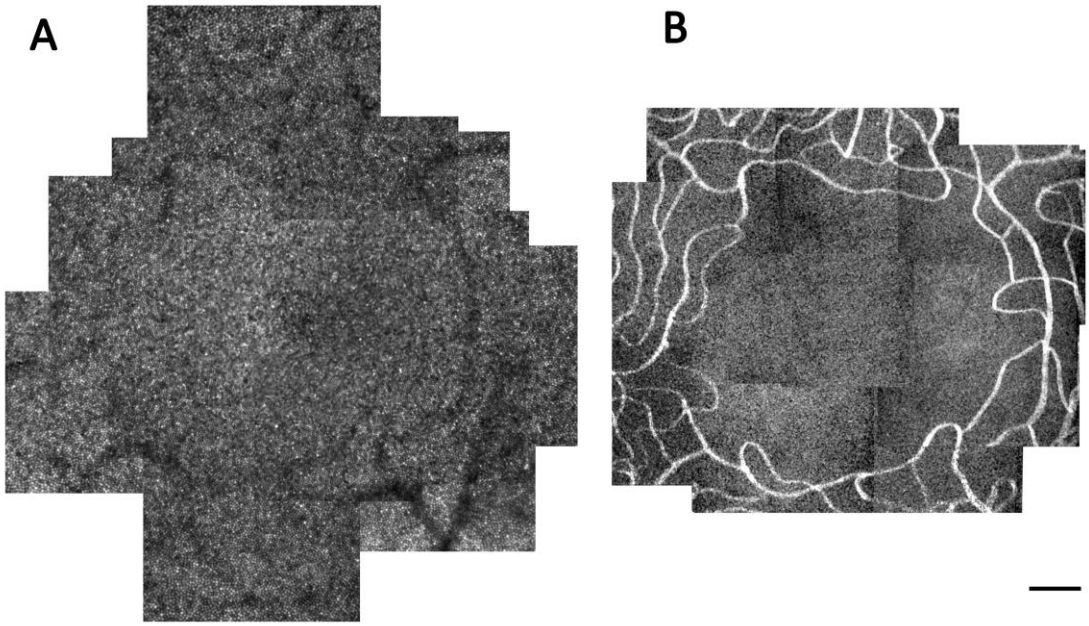

Figure 3-2. (A) Representative AOSLO cone photoreceptor mosaic acquired over the central 4° of the fovea in a 6 year-old child. (B) Capillary perfusion image surrounding the foveal avascular zone for the same subject at the same spatial scale as in (A). Scale bar = 100 μm.

3.2.4 Statistical analysis

Data are presented as mean ± standard deviation. Multiple linear regression models were conducted to examine the relationships of cone density, cone spacing, FAZ size, and foveal pit metrics with age and axial length across all eyes. To reduce the false-discovery rate associated with multiple statistical testing, a Bonferroni correction was applied and a *P* value of < 0.0026 was considered significant. To compare FAZ and foveal pit metrics between myopic and non-myopic children, unpaired t tests (or Mann-Whitney Rank Sum tests) were used for metrics following a normal (or non-normal, as determined by Kolmogorov–Smirnov test) distribution. A three-way ANOVA was performed for the analysis of cone density and spacing to study interactions between refractive error, eccentricity and meridian. A *P* value < 0.05 was considered statistically significant.

3.3 Results

Forty-eight eyes from 48 children (23 females, 25 males) were included in the study. Subject characteristics are shown in Table 3-1. Children had a mean age of 11.2 ± 2.7 years and ranged from 5.8-15.8 years old. Parents self-reported the race or ethnicity of their children to be White (n = 15), Hispanic (n = 19), African-American (n = 8), Asian (n = 3) and mixed (n = 3). All children were reported to be full-term (greater than 38 weeks gestation) by their parents. The mean spherical equivalent refractive error (SER) for all subjects was -0.13 ± 2.08 D (range: -5.44 D to +7.23 D). Mean axial length was 23.44 ± 1.02 mm (range: 20.86 to 25.64 mm). Eyes with longer axial lengths had more myopic spherical equivalent refractive errors (r = -0.77, $P < 0.0001$), and eyes of older children had longer axial lengths (r = 0.62, $P < 0.0001$).

Table 3-1. Demographic, refractive, and biometric characteristics for all 48 children (All Subjects) and separated by refractive group (Non-myopes, Myopes). Data are presented as mean ± standard deviation (range).

	All Subjects	**Non-myopes (SER > -0.50 D)**	**Myopes (SER ≤ -0.50 D)**	**P value**
Number of subjects	48	30	18	--
Sex (Female/Male)	23 / 25	16 / 14	7 / 11	--
Age (years)	11.2 ± 2.7 (5.8 to 15.8)	10.2 ± 2.6 (5.8 to 15.8)	12.9 ± 1.9 (8.5 to 15.8)	<0.001*
Spherical Equivalent Refractive Error (D)	-0.13 ± 2.08 (-5.44 to +7.23)	0.96 ± 1.64 (-0.44 to +7.23)	-1.96 ± 1.32 (-5.44 to -0.56)	<0.001*
Axial length (mm)	23.44 ± 1.02 (20.86 to 25.64)	22.94 ± 0.84 (20.86 to 24.54)	24.26 ± 0.72 (22.81 to 25.64)	<0.001*
Anterior corneal radius of curvature (mm)	7.75 ± 0.24 (7.29 to 8.36)	7.79 ± 0.24 (7.42 to 8.36)	7.68 ± 0.22 (7.29 to 8.19)	0.1
Corneal thickness (µm)	557.9 ± 30.0 (487 to 633)	565.0 ± 29.7 (492 to 633)	545.9 ± 27.2 (487 to 598)	0.03*
Anterior chamber depth (mm)	3.74 ± 0.30 (2.96 to 4.38)	3.64 ± 0.28 (2.96 to 4.19)	3.92 ± 0.26 (3.54 to 4.38)	< 0.01*
Lens thickness (mm)	3.43 ± 0.23 (3.05 to 4.55)	3.48 ± 0.25 (3.12 to 4.55)	3.34 ± 0.18 (3.05 to 3.79)	0.04*

* Indicates a statistically significant difference between non-myopes and myopes ($P < 0.05$)

3.3.1 Foveal parameters with age and axial length

Mean foveal pit metrics for all subjects (n = 48) are shown in Table 3-2. Across subjects, the range of foveal pit metrics varied between a factor of 1.3 (for foveal point thickness) and 2.2 (for foveal pit slope). Because age and axial length were found to be correlated, we performed a multiple linear regression analysis (with age and axial length as independent variables) to determine the extent to which each foveal pit metric was related to age and axial length. We found that no foveal pit metrics were significantly correlated with age or axial length (Table 3-2).

Mean FAZ parameters for all analyzed subjects (n = 31) are also shown in Table 3-2. FAZ parameters and cone metrics were analyzed for a subset of subjects as not all parents provided permission for AOSLO imaging, and some children found it challenging to maintain adequate fixation during imaging. FAZ area showed considerable variability between subjects, with an approximately 11-fold range of values (between 0.051 to 0.557 mm^2). After performing a similar multiple linear regression analysis (with age and axial length as independent variables), we found that no FAZ metrics were significantly correlated with age or axial length. However, there was a tendency for FAZ circularity to increase (P = 0.06) and FAZ acircularity to decrease (P = 0.07) with increasing axial length.

Table 3-2. Mean (± standard deviation) foveal pit and foveal avascular zone (FAZ) parameters, and their correlation with age and axial length across all children.

	Mean ± SD (Range)	R^2	Axial length (P Value)	Age (P Value)
Foveal Pit Metrics (n = 48)				
Foveal Pit Depth (µm)	129 ± 15 (99 to 170)	0.03	0.23	0.64
Foveal Pit Diameter (mm)	2.16 ± 0.19 (1.67 to 2.61)	0.06	0.10	0.33
Foveal Pit Slope (degrees)	16.5 ± 3.1 (11.5 to 25.6)	0.11	0.61	0.15
Foveal Point Thickness (µm)	220 ± 13 (195 to 258)	0.03	0.49	0.25
FAZ Metrics (n = 31)				
FAZ Area (mm^2)	0.302 ± 0.125 (0.051 to 0.557)	0.10	0.21	0.61
FAZ Perimeter (mm)	2.503 ± 0.666 (1.009 to 3.853)	0.04	0.93	0.35
Axis Ratio (unitless)	1.18 ± 0.15 (1.01 to 1.63)	0.04	0.31	0.96
FAZ Effective Diameter (µm)	606 ± 138 (255 to 842)	0.09	0.21	0.79
Circularity (unitless)	0.60 ± 0.15 (0.38 to 0.88)	0.12	0.06	0.27
Acircularity (unitless)	1.32 ± 0.16 (1.07 to 1.63)	0.11	0.07	0.27

Montages of the foveal cone mosaic were created for one eye of each of 29 children. Representative images of the cone mosaic are shown in Figure 3-3 for three subjects of different ages at each of the three examined eccentricities. Linear cone densities for all subjects are plotted at the eccentricities examined in Figure 3-4A. Mean linear cone densities across all children and meridians were 55,897 ± 6,698 cones/mm^2, 47,009 ± 4,802 cones/mm^2, and 32,556 ± 3,954 cones/mm^2 at 0.2 mm, 0.3 mm, and 0.5 mm eccentricities, respectively. A one-way ANOVA and Bonferroni post-hoc test revealed that linear and angular cone densities were significantly higher at an eccentricity of 0.2 mm compared to 0.3 mm ($P < 0.001$), and at an eccentricity of 0.3 mm compared to 0.5 mm ($P < 0.001$). A comparison of our mean linear cone density values with other histological and *in vivo* studies is shown in Table 3-3. Figure 3-4B shows mean linear cone densities along the horizontal and vertical meridians across the 29 examined subjects.

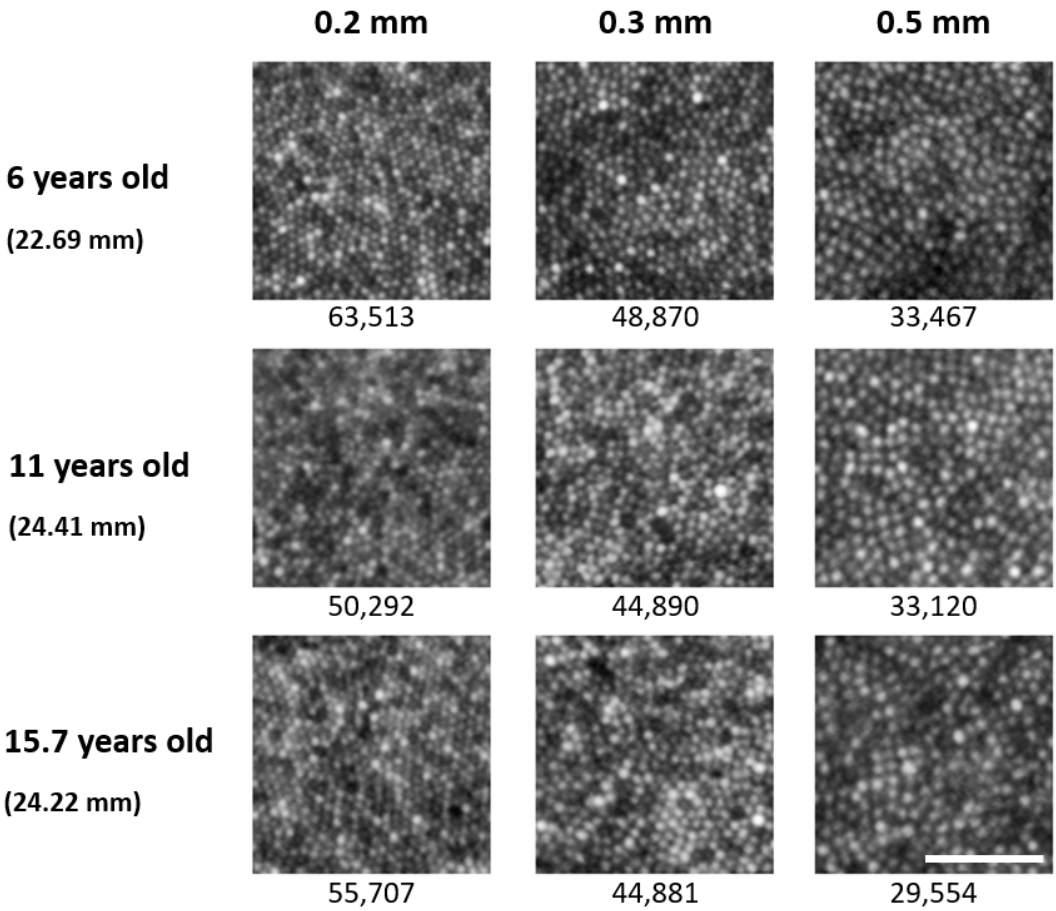

Figure 3-3. Representative cone photoreceptor images acquired along the inferior meridian in three subjects at the three examined eccentricities of 0.2 mm, 0.3 mm, and 0.5 mm from the estimated location of peak cone density. Each subject's axial length is indicated in parentheses beneath their age. Linear cone density (cones/mm^2) is specified for each image. Linear cone photoreceptor density decreases with increasing eccentricity in each eye. Scale bar = 50 μm.

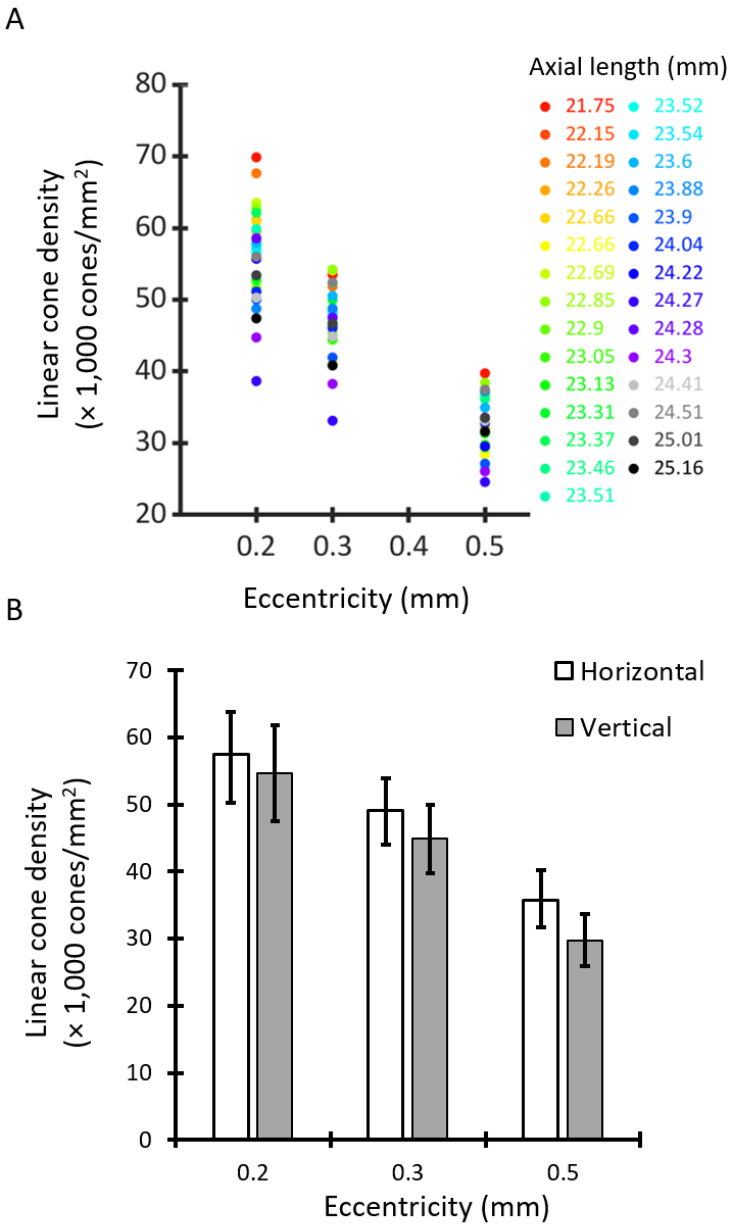

Figure 3-4. (A) Linear cone densities (cones/mm^2) averaged across all meridians for the 29 children examined at the three retinal eccentricities. Each subject is represented by a different color. (B) Mean linear cone densities averaged across horizontal (no fill) and vertical (gray) meridians. Error bars represent ± 1 standard deviation. Linear cone densities were significantly higher along the horizontal meridian than the vertical meridian across all eccentricities.

Table 3-3. Comparison of linear cone density measurements between previously published ex vivo and in vivo studies with measurements from the current study.

Study	Ex Vivo	In Vivo Adult			In Vivo Children/Adult	In Vivo Children
	Curcio et al. (1990)	Li et al. (2010)	Song et al. (2011)	Elsner et al. (2017)	Lombardo et al. (2012)	Park et al. (2013)	Current work
Number of subjects	7	18	10	36	12	36	29
Age range (years)	27-44	23-44	22-35	18-34	24-38	10-20	5-16
Axial length range (mm)	Not reported	22.9-28.3	22.1 - 26.1	23.2 - 25.8	22.6 - 26.6	22.01 - 28.43	20.86 - 25.64
Linear Cone Density (cones/mm^2) at eccentricities of:							
~0.20 mm	73,000	78,900 ± 9300	67,400 ± 15,600 (0.18 mm)	Not reported	Not reported	Not reported	55,897 ± 6,698
~0.30 mm	53,500	57,000 ± 6800	56,700 ± 7,900 (0.27 mm)	43,216 ± 6,039 (0.27 mm)	49,393 ± 7,941 (0.26 mm)	Not reported	47,009 ± 4,802
~0.40 mm	42,200	Not reported	46,800 ± 8,300 (0.36 mm)	Not reported	38,000	Not reported	Not reported
≥ 0.50 mm	36,000 (0.50 mm)	Not reported	38,800 ± 7,500 (0.45 mm)	27,466 ± 3,496 (0.63 mm)	30,049 ± 4,954 (0.6 mm)	32,554 ± 2,884 (0.50 mm)	32,556 ± 3,954 (0.50 mm)
Meridians reported	All	All	All	All	Horizontal	All	All

Cone metrics as a function of axial length for three different retinal eccentricities are shown in Figure 3-5. A multiple linear regression was performed for each cone metric measured at each eccentricity, with age and axial length as independent variables, and the cone metric as the dependent variable. These analyses yielded statistically significant relationships only for metrics analyzed at an eccentricity of 0.2 mm. At this eccentricity, the model explained 50.4% of the variance in linear cone density (cones/mm^2), and revealed that linear cone density significantly decreased with increasing axial length (P = 0.001, Fig. 3-5A). Similarly, 46.8% of the variance in farthest neighbor distance (when measured at an eccentricity of 0.2 mm) could be explained using a multiple linear regression model. The model showed that eyes with longer axial lengths also had increased cone spacing (i.e., increased farthest neighbor distance) (P = 0.002, Fig. 3-5C). Neither axial length nor age contributed to the regression models for angular cone density (cones/deg^2) at any eccentricity (Fig. 3-5B).

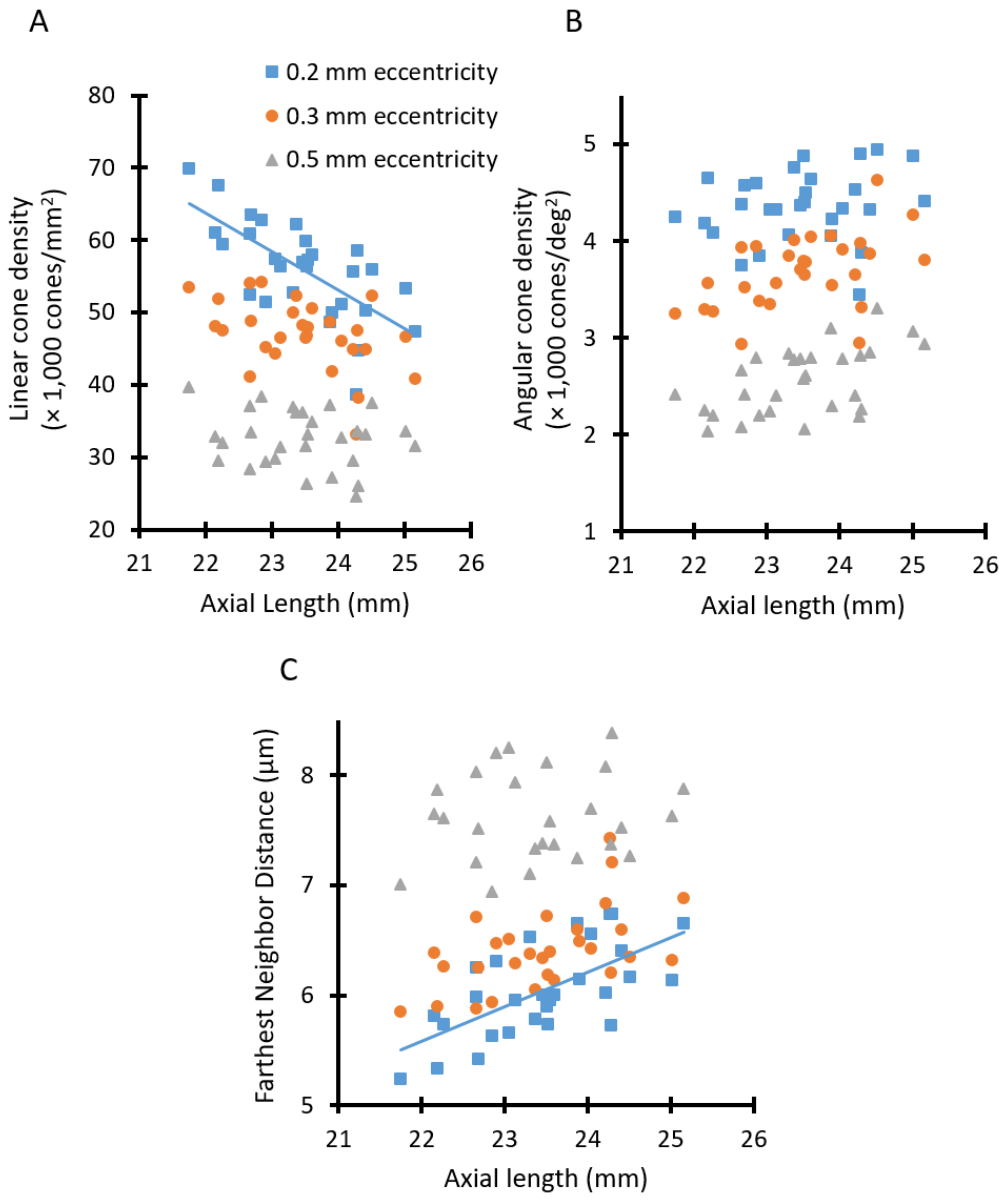

Figure 3-5. Cone metrics were analyzed as a function of axial length at eccentricities of 0.2 mm (blue squares), 0.3 mm (orange circles), and 0.5 mm (gray triangles) for 29 subjects. Lines show linear regressions for those data that possessed a statistically significant relationship. (A) Linear cone density (cones/mm^2) significantly decreased with increasing axial length only at an eccentricity of 0.2 mm (linear cone density [x 1,000 cones/mm^2] = -5.2913 x (axial length, in mm) + 180.08, *P*=0.001). (B) Angular cone density (cones/deg^2) was not significantly related to axial length at any examined eccentricity. (C) Farthest neighbor distance significantly increased in eyes with longer axial lengths only at an eccentricity of 0.2 mm (farthest neighbor distance = 0.312 x (axial length, in mm) – 1.2785, *P*=0.002).

3.3.2 Foveal parameters between myopic and non-myopic children

Foveal pit and FAZ metrics were compared between eyes of children that were myopic (SER ≤ -0.50 D) and non-myopic (SER > -0.50 D, Table 3-4). There were no significant differences in foveal pit metrics between refractive error groups. However, myopic eyes tended to have flatter foveal pits compared to non-myopes (foveal pit slope = 15.5 ± 2.5° vs. 17.2 ± 3.3°, respectively, $P = 0.06$). In addition, no statistically significant differences in FAZ metrics were found between the two refractive error groups ($P > 0.05$).

Mean values of all three cone metrics are presented in Figure 3-6 for myopic and non-myopic groups at the examined eccentricities. At an eccentricity of 0.2 mm, mean linear cone density was 50,022 ± 5,878 cones/mm^2 for the myopic group versus 58,989 ± 4,822 cones/mm^2 for the non-myopic group (Fig. 3-6A). At a retinal eccentricity of 0.3 mm, mean linear cone densities for myopic and non-myopic groups were 43,944 ± 5,547 cones/mm^2 and 48,622 ± 3,538 cones/mm^2, respectively. The difference in linear cone density between refractive groups was lowest at 0.5 mm eccentricity (31,512 ± 4,389 cones/mm^2 for myopes vs 33,105 ± 3,710 cones/mm^2 for non-myopes).

Table 3-4. Mean (± standard deviation) foveal pit and FAZ metrics in myopic and non-myopic children.

	Myopic	Non-myopic	P Value
Foveal Pit Metrics (n = 48)			
Number of Subjects	18	30	--
Foveal Pit Depth (µm)	129 ± 16	129 ± 14	0.83
Foveal Pit Diameter (mm)	2.21 ± 0.21	2.13 ± 0.18	0.18
Foveal Pit Slope (degrees)	15.5 ± 2.5	17.2 ± 3.3	0.06
Foveal Point Thickness (µm)	220 ± 16	219 ± 10	0.86
FAZ Metrics (n = 31)			
Number of Subjects	11	20	--
FAZ Area (mm^2)	0.338 ± 0.162	0.283 ± 0.099	0.25
FAZ Perimeter (mm)	2.592 ± 0.805	2.454 ± 0.593	0.59
Axis Ratio	1.14 ± 0.08	1.21 ± 0.17	0.24
FAZ Effective Diameter (µm)	632 ± 185	591 ± 107	0.44
Circularity	0.61 ± 0.15	0.60 ± 0.15	0.88
Acircularity	1.31 ± 0.17	1.32 ± 0.17	0.88

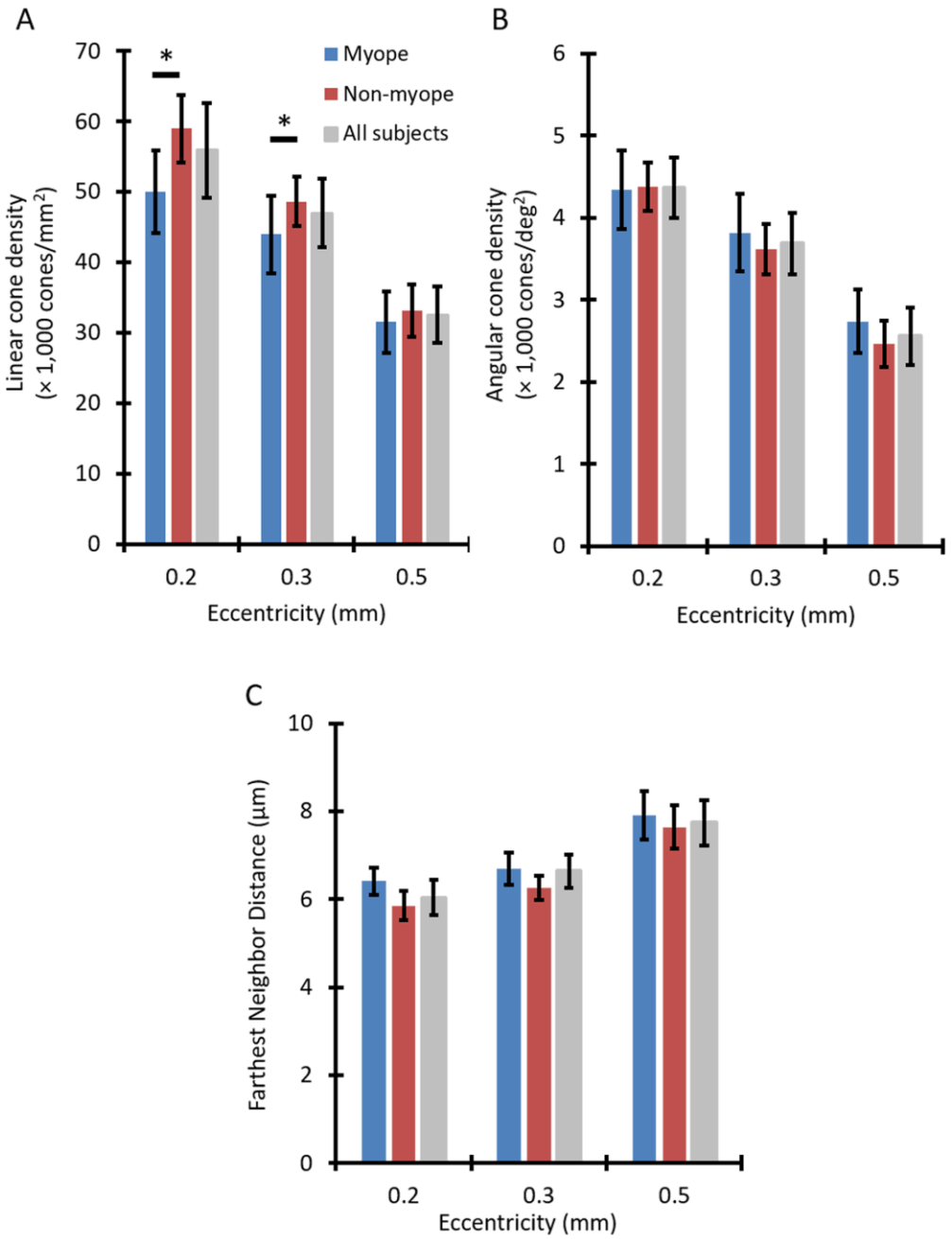

Figure 3-6. Differences in cone density and spacing metrics were found between myopic and non-myopic groups. Mean (A) linear cone density, (B) angular cone density, and (C) farthest neighbor distance averaged across 10 myopic children (blue), 19 non-myopic children (red), and all 29 children combined (gray) as a function of eccentricity. Error bars represent ± 1 standard deviation. Asterisks indicate a statistically significant difference between myopic and non-myopic groups at a given retinal eccentricity (P<0.001). (A) Linear cone density was significantly lower in myopic children at 0.2 and 0.3 mm eccentricities. (B) Angular cone density was significantly higher across all eccentricities combined in myopic children. (C) Farthest neighbor distance was also significantly higher across all eccentricities combined in myopic children.

Table 3-5 presents results from three-way ANOVAs that were performed to investigate whether there were any significant effects of eccentricity, meridian, and refractive error group on cone density and spacing parameters, and whether there were significant interactions between these variables. For both linear and angular cone densities, significant effects of eccentricity, meridian, and refractive group were observed ($P < 0.05$ for each variable). Linear and angular cone densities were significantly higher along the horizontal meridian than the vertical meridian ($P < 0.001$ for both, Fig. 3-4B). A significant interaction was observed between eccentricity and refractive group ($P < 0.001$) for linear cone density, with myopic children showing decreased linear cone density compared to non-myopic children at eccentricities of 0.2 mm and 0.3 mm ($P < 0.001$). Similarly, for farthest neighbor distance, significant effects of eccentricity, meridian, and refractive status were observed, with a significant interaction between eccentricity and meridian ($P < 0.001$ for all). Farthest neighbor distance was greater for myopic versus non-myopic children across all eccentricities combined ($P < 0.001$), and was smaller in the horizontal meridian versus the vertical meridian at an eccentricity of 0.5 mm ($P < 0.001$).

In order to provide a more comprehensive assessment of the foveal region in children, we examined whether relationships exist between various metrics (including FAZ and foveal pit parameters) across all eyes. Eyes with larger FAZ areas had wider and deeper foveal pits ($r = 0.65$, $P < 0.001$, and $r = 0.56$, $P = 0.002$, respectively). FAZ area was also smaller in eyes with greater foveal point thicknesses ($r = -0.70$, $P < 0.001$), while eyes with thinner foveal point thicknesses had deeper foveal pits ($r = -0.61$, $P = 0.001$). Linear cone density at an eccentricity of 0.2 mm was lower in eyes with larger FAZ areas ($r = -0.45$, $P = 0.02$) and wider foveal pits ($r = -0.40$, $P = 0.03$).

Table 3-5. Main effects and interaction effects of eccentricity, meridian, and refractive group on cone photoreceptor density and spacing metrics.

	P value		
	Linear Cone Density (cones/mm^2)	**Angular Cone Density (cones/deg^2)**	**Farthest Neighbor Distance**
Main effect of eccentricity	<0.001*	<0.001*	<0.001*
Main effect of meridian	<0.001*	<0.001*	<0.001*
Main effect of refractive group	<0.001*	0.011*	<0.001*
Interaction effect of eccentricity x meridian	0.185	0.151	<0.001*
Interaction effect of eccentricity x refractive group	<0.001*	0.125	0.231
Interaction effect of meridian x refractive group	0.672	0.360	0.244
Interaction effect of eccentricity x meridian x refractive group	0.662	0.601	0.278

* $P < 0.05$ was regarded as statistically significant

3.4 Discussion

The main purpose of this study was to determine whether overall foveal structure differs as a function of age and refractive status in children. Eyes with myopic refraction and increased axial length tended to have decreased linear cone density close to the fovea. Linear cone density (cones/mm^2) was significantly lower in eyes of myopic children compared to non-myopic children at 0.2 and 0.3 mm eccentricities. However, foveal avascular zone and foveal pit geometry were independent of age, axial length, and refractive status.

None of the foveal avascular zone, foveal pit, or cone density metrics measured in the children in this study showed a significant relationship with age, suggesting that the foveal parameters investigated here may be close to being fully developed. Although studies have shown that foveal development is a protracted process (Hendrickson et al., 2012; Vajzovic et al., 2012), the rate of development and maturation of different aspects of the fovea is not constant throughout infancy, childhood, and adolescence. For example, Lee et al. (2015) reported that outer nuclear layer, inner segment, and outer segment thicknesses increase logarithmically between birth and the first few years after birth, after which the thicknesses of these layers increase more gradually during childhood and adolescence. An increase in the thickness of the outer nuclear layer could be explained by the migration of cone photoreceptors toward the foveal center. However, there is no direct evidence in the literature as to when cones cease centripetal migration or the rate at which they migrate over time. Based on Yuodelis and Hendrickson's work (Yuodelis & Hendrickson, 1986), cone density for a 37 year-old donor eye was twice the density of a 45 month-old donor eye, whose density was ten times greater than the density of a donor eye at 22 weeks gestation.

This study is the first to report *in vivo* cone densities specifically in young children at retinal eccentricities within 0.45 mm (~1.5°) of the foveal center. Published cone photoreceptor data in children under 18 years of age are sparse. Park et al.(Park et al., 2013) used AOSLO

imaging to measure cone densities at 0.5, 1.0, and 1.5 mm eccentricities in subjects between 10 and 20 years old. More recently, Tumahai et al. (2018) used an adaptive optics retinal camera (RTX-1, Imagine Eyes) to measure cone density at an eccentricity of 0.45 mm in the nasal and temporal meridians of subjects between 6 and 20 years of age. In both of these studies, children were not classified separately from adults and mean cone density was reported for all subjects younger than 20 years old, making it challenging to determine potential differences in density between children and adult eyes. Building on these reports, we detail cone density measurements in children as young as 5.8 years old (range: 5.8-15.8 years) at eccentricities as close as 0.2 mm from the fovea.

Linear cone density values measured in the eyes of the children in our study are comparable to those measured in adolescent eyes at slightly more peripheral locations (0.5 mm) (Table 3-3). The mean value of linear cone density calculated in the children in this study at an eccentricity of 0.5 mm (32,556 ± 3,954 cones/mm^2) was similar to the values reported by Park et al.(Park et al., 2013) in 10 to 20 year old subjects at an eccentricity of 0.5 mm (32,554 ± 2,884 cones/mm^2) and by Tumahai et al. (2018) in 6 to 20 year old subjects at an eccentricity of 0.45 mm (~36,500 cones/mm^2). However, given the lack of published data on cone density in children at closer eccentricities, we also compared measurements from the children in our study with those from studies performed in adult eyes. While the cone density values reported in this study are lower than *ex vivo* values reported by Curcio et al. (1990) and *in vivo* values reported by Li et al. (2010), they are within the range of reported *in vivo* values in adult eyes (Table 3-3). For example, at an eccentricity of 0.3 mm, the mean linear cone density measured in this study (47,009 ± 4,802 cones/mm^2) is less than the mean value reported by Li et al. (Li et al., 2010) (57,000 ± 6800 cones/mm^2) at 0.3 mm in 18 adult eyes, but is greater than the mean values reported by Elsner et al. (2017) (43,216 ± 6,039 cones/mm^2) at 0.27 mm in 36 adult eyes (where density would be expected to be greater than that measured at 0.3 mm).

Similarly, at an eccentricity of 0.2 mm, the mean linear cone density measured in this study (55,897 ± 6,698 cones/mm^2) is lower than the values reported by Curcio et al. (1990) and Li et al. (2010) (73,000 and 78,900 ± 9,300 cones/mm^2, respectively). However, our mean value of cone density along the horizontal meridian at the same eccentricity of 0.2 mm (57,412 ± 6,427 cones/mm^2) is similar to values reported by Lombardo et al. (2013) at an eccentricity of 0.25 mm along the horizontal meridian (mean = 57,508 cones/mm^2). Even though Hendrickson et al. (2012) found that the thickness of the outer nuclear layer increases from one nucleus thick at birth to 12 nuclei-thick at 13 years of age, we did not observe a significant relationship between cone density and age after controlling for the effect of axial length. In addition, the cone density values measured in the children in our study are already within an adult-like range. Hence, it is possible that the majority of cone photoreceptor migration toward the foveal center occurs by a younger age and/or cone migration beyond the age of 5 occurs at a rate that is slower compared to first few years of life. Further study is warranted in children younger than 5 years of age, as well as in longitudinal studies, to elucidate differences in cone density during infancy and childhood. Such studies could additionally provide improved understanding of the variability in cone density and spacing metrics for children of a given age, as well as across ages.

Consistent with results reported histologically (Curcio et al., 1990) and *in vivo* in adult eyes (Chui et al., 2008b; Song et al., 2011; Park et al., 2013), we observed higher linear cone densities along the horizontal meridian in children (Fig. 3-4B). Differences in cone density were measured between the horizontal and vertical meridians across all eccentricities. However, the difference was statistically significant only for farthest neighbor distance at an eccentricity of 0.5 mm.

No relationships were found between foveal pit metrics and age in the children in our study. Previous histological studies performed in a limited set of retinas from children have reported that the foveal pit becomes wider and shallower postnatally (Hendrickson et al., 2012;

Springer & Hendrickson, 2005). More recently, Read et al. (2015) performed *in vivo* OCT imaging in nearly 200 children between 4 and 12 years of age and found a significant increase in foveal thickness with age. However, we did not find any relationships between foveal pit shape or foveal point thickness and age in our cohort of 5 to 15 year old children. These conflicting results may stem from multiple sources, including differences in age, race, and refractive error between studies. For example, subjects in the Read et al. (2015) study were younger in age relative to our subjects, and 90% of their sample was White, whereas our population was more diverse (primarily consisting of 31% White, 40% Hispanic, and 17% African-American). Moreover, the range of spherical equivalent refractive errors in the Read et al.(Read et al., 2015) study was close to emmetropia (-0.50 D to +1.25 D), while the spherical equivalent refractive errors in our sample were more broadly distributed, ranging from -5.44 D to +7.23 D.

Values of foveal pit metrics measured in our cohort are similar to those reported in previous studies in children and adults. Mean (± standard deviation) values of foveal pit depth and slope in our study (129 ± 15 µm and 16.5 ± 3.1°, respectively) are comparable to values reported by Yanni et al.(Yanni et al., 2012) in 34 normal children aged 5 to 16 years (129.6 ± 35.6 µm and 14.6 ± 5.2°, respectively), while foveal pit diameter was slightly larger in our group (2.16 ± 0.19 mm vs 1.77 ± 0.35 mm). Foveal pit metrics in the Yanni et al. (2012) study were quantified from a single horizontal (and vertical) line scan bisecting the fovea, which ignores the heterogeneity of foveal pit structure measured along different meridians. In our study, we built on the approach introduced by Dubis et al. (2009) to model the foveal pit in three dimensions, thereby better representing the overall shape of the pit and providing more accurate measures of pit parameters. In addition to being similar to previous reports in children, the range of values for foveal pit depth (99 – 170 µm), diameter (1.67 – 2.61 mm), and slope (11.5 – 25.6 degrees)

in the current study are similar, but slightly higher, than those reported in adults by Dubis et al. (2012) (48 – 156 µm, 1.12 – 2.40 mm, and 5.1 – 21 degrees, respectively).

Linear cone density significantly decreased in eyes with longer axial lengths only at an eccentricity of 0.2 mm (Fig. 3-5A), indicating that axial elongation impacts cone density at retinal locations closer to the foveal center. We were unable to image the central-most foveal cones in any children, and therefore could not determine whether this trend was also true at the foveal center. However, when coupled with no observed change in angular cone density with increasing axial length, this decrease in linear cone density at 0.2 mm eccentricity supports a simple scaling model of growth in which the size and spacing of the more central cones increase in response to axial elongation. It would be valuable to measure cone densities at locations closer to the foveal center and at more peripheral eccentricities to provide more information on whether axial elongation differentially impacts retinal structure at different eccentricities.

In agreement with previous studies in adults, linear cone density is significantly lower in myopic compared to non-myopic children (Chui et al., 2008a; Lombardo et al., 2012). Specifically, the eyes of myopic children had significantly lower linear cone densities compared to the eyes of non-myopic children at retinal eccentricities of 0.2 mm and 0.3 mm (three-way ANOVA, post-hoc comparison, $P < 0.001$). Lombardo et al. (2012) examined linear cone density in young adult eyes at eccentricities of 0.26, 0.4, and 0.6 mm and found that the mean difference in cone density between emmetropic and myopic eyes was greatest at an eccentricity of 0.26 mm (7,709 cones/mm^2) and lowest at an eccentricity of 0.6 mm (4,536 cones/mm^2). Likewise, in our study, the mean difference in linear cone density was highest at the closest eccentricity examined (8,967 cones/mm^2 at 0.2 mm eccentricity) and lowest at the furthest eccentricity examined (1,593 cones/mm^2 at 0.5 mm eccentricity).

We found no significant correlations between any foveal pit metric and axial length in our cohort. Axial length has been shown to dramatically increase during the first few years of life (Larsen, 1971), and retinal stretching (potentially resulting from axial elongation) has been proposed as a mechanism for altering the morphometry of the foveal pit (Springer and Hendrickson, 2005). It is possible that the lack of relationship found between axial length and foveal pit metrics in our study could have been confounded by the racial makeup of our subjects. Wagner-Schuman et al. (2011) reported that differences in foveal pit architecture exist between White and African-American adult subjects. Given the more heterogeneous ethnic composition of our cohort, future studies could include additional children across different racial and ethnic groups. In addition, we found no significant difference in foveal pit morphometry between myopic and non-myopic children. This finding is consistent with results reported by Dubis et al. (2009) in 61 healthy emmetropic and myopic subjects aged between 13 and 52 years.

None of the FAZ metrics calculated in this study were correlated with age or axial length. Previous work conducted by Cheung et al. (2019) in a population of children aged 6-8 years old in Hong Kong found that FAZ area decreases in eyes with longer axial lengths. The discrepancy between their findings and those reported in this study could be due to several factors, including differences in the range of ages and ethnicities of both groups. Furthermore, Cheung et al. (2019) did not report whether they laterally scaled the magnification of their retinal images to correct for differences in axial length between subjects, providing another potential source for the discrepancy. In alignment with our results in children, studies conducted in adult eyes which have scaled for retinal magnification have reported no significant relationship between FAZ area and axial length (Dubis et al., 2012; Fujiwara et al., 2017). In addition, the mean value and range of FAZ area measured in the children in this study (mean = 0.302 ± 0.125 mm^2; range: 0.051 – 0.557 mm^2) are comparable to those recently measured in children between the ages of

9 weeks to 17 years by Hsu et al. (2019) (mean = 0.347 ± 0.168 mm^2; range: 0.05 – 1.17 mm^2) and 9-18 years by Golebiewska et al. (2019) (range: 0.004 – 0.563 mm^2). The range of FAZ areas measured in our study is also in agreement with the range of FAZ areas imaged using adaptive optics in adult eyes (Chui et al., 2012).

In conclusion, this study provides a comprehensive, *in vivo* assessment of foveal morphometry and cone density in healthy children. Our work expands upon previously published studies on retinal structure of children in several ways. First, this study quantifies cone density and spacing in a group of children as young as 5.8 years of age at eccentricities as close as 0.2 mm from the fovea. Second, we investigated the size of the FAZ, morphometry of foveal pit, and cone density and spacing in the same subjects to provide a more comprehensive assessment of the foveal region in children. We found that age was not correlated with any foveal pit, FAZ, or cone density or spacing metric. FAZ and foveal pit morphometry were not different between myopic and non-myopic children whereas linear cone density was lower in myopic children at 0.2 and 0.3 mm eccentricities compared to non-myopic children.

3.5 Acknowledgments

This work was supported by National Institutes of Health (NIH) Grant P30 EY07551, and the University of Houston, College of Optometry. The authors thank Suman Adhikari, Joseph Carroll, Robert Cooper, Austin Roorda, and Alexander Schill for their helpful discussions.

CHAPTER 4

Examination of parafoveal intercapillary region with axial length and FAZ structure in healthy adults

Contributing Authors:

Gwen Musial, PhD; Suman Adhikari, B Optom; Hope M. Queener, MS; Toco Y.P. Chui, PhD; Jason Porter, PhD

4.1 Introduction

The retina is one of the most metabolically active tissues in the human body. It receives its blood supply from two sources, the choriocapillaris and the central retinal artery, the second of which branches into several vascular plexuses (Chen et al., 2016). In the macular region, there are up to four vascular networks (Snodderly et al., 1992; Tan et al., 2012; Chan et al., 2015), including a superficial vascular plexus located in the ganglion cell layer, with intermediate and deep plexuses residing above and below the inner nuclear layer. *In vivo* and *ex vivo* studies that have characterized these networks in human eyes (Chan et al., 2012; Tan et al., 2012; Chan et al., 2015) have revealed a laminar configuration for the deep plexus and a more three-dimensional configuration for the superficial and intermediate plexuses that span different depths. These arrangements are not uniform across the retina. In the foveal region, for instance, a single layer of capillaries that is formed by anastomoses between three networks (superficial, intermediate, and deep) surrounds the foveal avascular zone (Iwasaki & Inomata, 1986; Snodderly et al.,1992; Provis et al., 2000).

The potential impact of the eye's axial length and refractive error on measures of vascular network structure, such as vessel density, is not well-defined. While some studies report reduced vessel density in the superficial macular plexus of highly myopic eyes relative to low myopic/emmetropic eyes (Yang et al., 2016; Li et al., 2017; Leng et al., 2018), other studies have reported no differences in vessel density in the superficial and deep macular networks of eyes with different refractive errors (Yang et al., 2017; Wang et al., 2016). Although measurements of vessel density made from optical coherence tomography angiography (OCTA) images are relatively robust to small segmentation errors, the sensitivity of using this metric for detecting small changes in capillaries is limited (Salz et al., 2016; Schottenhamml et al., 2016). Metrics of parafoveal intercapillary regions (PICRs), or regions between capillaries, may be more sensitive to changes in vascular geometry than vessel density (Salz et al., 2016;

Schottenhamml et al., 2016; Krawitz et al., 2018). For example, a small loss in capillary perfusion may cause a relatively small change in vessel density, but affects intercapillary area to a greater extent. Having a metric that provides accurate information on vessel network geometry is important for better understanding how the retina receives nourishment from its vasculature, particularly for capillaries within the single-layered network surrounding the fovea (or foveal avascular zone). For example, previous studies have shown that the optimal intercapillary distance for oxygen diffusion in the retina is approximately 60 µm (Iwasaki & Inomata, 1986; Chui et al., 2014; Krawitz et al., 2018), with larger intercapillary distances potentially resulting in inadequate oxygenation. Currently, it is unknown whether this optimal distance is preserved in eyes of various axial lengths for capillaries surrounding the foveal avascular zone (FAZ). Moreover, there is a relative lack of data detailing the impact of axial length on PICR geometry and intercapillary spacing surrounding the FAZ.

The primary aim of this study was to determine whether PICR properties for those capillaries surrounding the margin of the FAZ are related to an eye's axial length and/or FAZ structure. PICR metrics were quantified from adaptive optics perfusion images of the FAZ acquired in healthy adult eyes. We then examined whether relationships exist between PICR metrics, axial length, and metrics of FAZ structure. The results of this work provide insights into whether axial elongation may play a role in shaping microvessel geometry surrounding the FAZ.

4.2 Methods

All research adhered to the tenets of the Declaration of Helsinki and was reviewed by the University of Houston Institutional Review Board. Healthy adult subjects between the ages of 20 to 40 years with no history of ocular disease, diabetes, or hypertension were recruited. Written informed consent was obtained from all subjects prior to conducting the experiment. The right eye of each subject was dilated using 1% tropicamide (Henry Schein Inc., Melville, NY USA)

and 2.5% phenylephrine (Paragon Bio Teck Inc., Portland, OR USA). Upon dilation, autorefraction was performed three times and averaged (WAM-5500, Grand-Seiko, Hiroshima, Japan). Axial length, anterior corneal radius of curvature, central corneal thickness, anterior chamber depth, and lens thickness were measured using an ocular biometer (LenStar LS 900, Haag-Streit, Koeniz, Switzerland). Biometry data were used to laterally scale adaptive optics images using a four surface eye model as described in Chapter 2 (Patel et al., 1995; Williams, 1992; Le Grand & El Hage, 1980).

4.2.1 Imaging and analysis of capillaries surrounding the FAZ

The Houston adaptive optics scanning laser ophthalmoscope (AOSLO) (Mirhajianmoghadam et al., 2020) was used to image perfused retinal capillaries extending at least 300 μm from the FAZ margin in the right eye of each subject. While OCTA is a powerful technique that can rapidly acquire images of perfused retinal vessels, its ability to resolve and distinguish fine retinal capillaries is limited due to the presence of ocular aberrations. In contrast, AOSLO imaging provides increased lateral resolution, enabling the visualization of the smallest capillaries *in vivo* and has been shown to better distinguish close-running capillaries compared to OCTA imaging (Kaizu et al., 2017). Given this result and the need to resolve fine foveal capillary structure (~5 to 7 μm in diameter) (Rha et al., 2006) that is below the lateral resolution afforded using OCTA, we chose to perform our imaging using an AOSLO. A custom-made bite bar was used to position each subject in 3-dimensions with respect to the AOSLO's optical axis. A digitally-controlled fixation target was presented and moved within the AOSLO system to guide the patient's fixation for the purpose of imaging desired regions of the retina surrounding the FAZ margin. Confocal and split detector videos of retinal vasculature were simultaneously collected over a 1.5° field of view at a 25 Hz frame rate. The imaging plane of the AOSLO was first adjusted so that the most superficial capillaries forming the temporal side of the FAZ were in

focus. Two 10 second (250 frame) long videos were recorded at each location around the FAZ at this most superficial imaging plane and then at a focus that was approximately 0.075 Diopters (~15 µm) beneath the most superficial layer. Offline, videos were corrected for scan distortions and were stabilized. Subsequently, perfusion images were created using a method similar to that employed by Chui et al. (2012) as described in Chapter 2. Registered perfusion images were stitched together (Adobe Photoshop, Adobe Systems Inc., San Jose, CA USA) to create montages of perfused retinal vasculature at each focus (Figures 4-1A, B). A maximum intensity projection (MIP) montage was created from the montages generated at the two imaging planes using ImageJ (Schneider et al., 2012) (Figure 4-1C). Retinal capillaries were automatically segmented from the MIP perfusion montage using a convolutional neural network (CNN) developed for segmenting capillaries in adaptive optics images (Musial et al., 2020). The resulting probability maps (Figure 4-1D) were then converted to binary images using the "Make Binary" function in ImageJ (Figure 4-1E). The CNN was designed to separately segment capillaries from intermediate and larger vessels. When applied to vasculature surrounding the FAZ, the CNN segmented only capillaries (Figure 4-1E). Hence, an expert rater evaluated all binarized segmentations and manually segmented intermediate and large vessels, while also correcting any segmentation errors (Figure 4-1F).

A custom MATLAB program (MathWorks, Inc., Natick, MA USA) was used to automatically delineate the FAZ and all surrounding PICRs. Any region formed by vessels that made an entirely closed contour (excluding the FAZ) was considered as a PICR. The "regionprops" function was used to calculate FAZ area, FAZ circularity, and PICR metrics. Circularity was calculated as:

$$Circularity = 4\pi\left(\frac{area}{perimeter^2}\right) \quad (4.1)$$

where a value of 1 indicates a perfect circle and a value closer to 0 indicates an elongated polygon shape. The program also created masks to remove vessels that are located outside of

three zones with distances of 100 µm, 200 µm, and 300 µm from the FAZ margin (Figure 4-2). To calculate PICR metrics for each zone, only PICRs whose centroids were located inside the corresponding mask were used. PICR area and circularity were then calculated. In addition, an ellipse was fit to each PICR using second order moments (Hu et al., 1962) and was used to calculate major axis length, minor axis length, and axis ratio (or the ratio of the major axis to minor axis length).

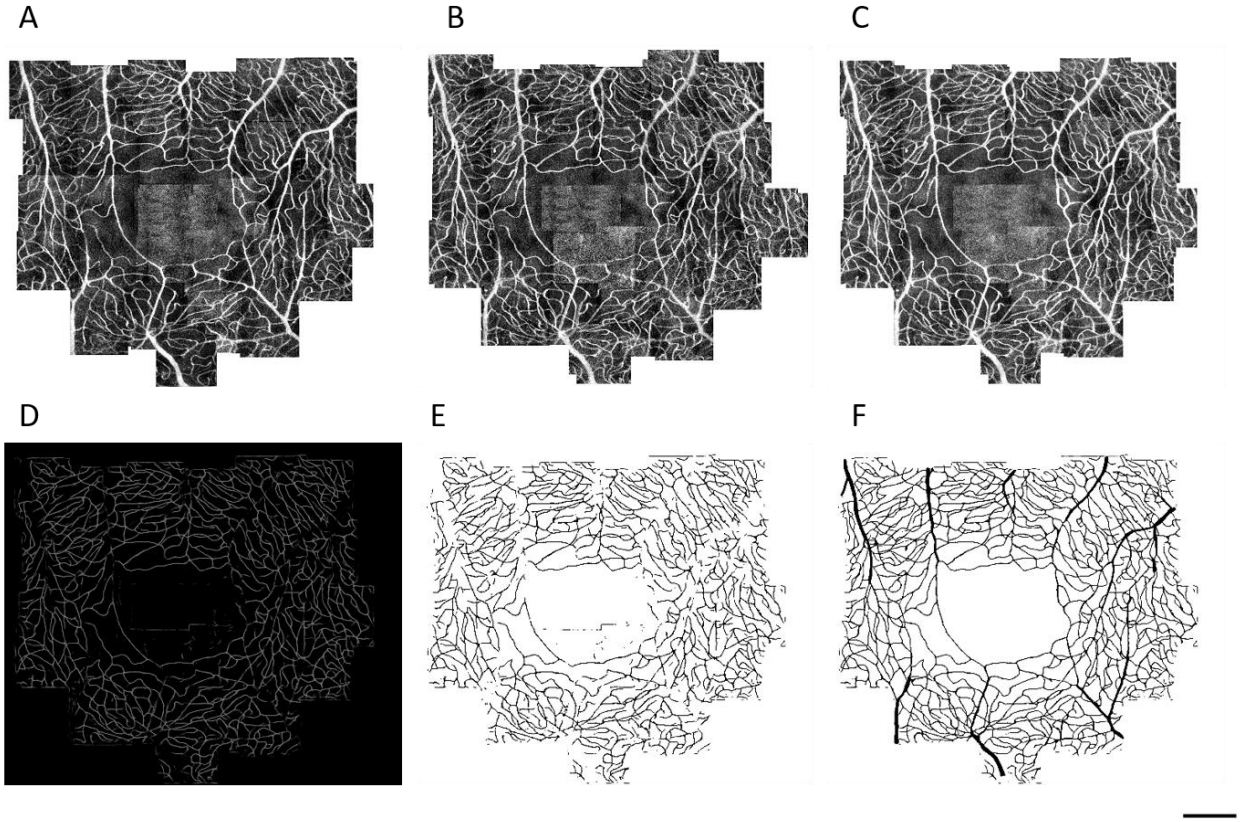

Figure 4-1. Sequence of images from a representative healthy adult eye illustrating the process for creating perfusion maps of the central-most foveal capillaries. Montages of perfused parafoveal vessels surrounding the FAZ were generated at (A) the most superficial focus and (B) approximately 15 µm deeper. (C) A maximum intensity projection (MIP) image was created from the montages in (A) and (B) and subsequently segmented using a convolutional neural network (CNN). (D) Image of the probability map generated following CNN segmentation of the MIP image, which was (E) binarized and (F) manually corrected to remove small fragments and include larger vessels. Scale bar: 300 µm.

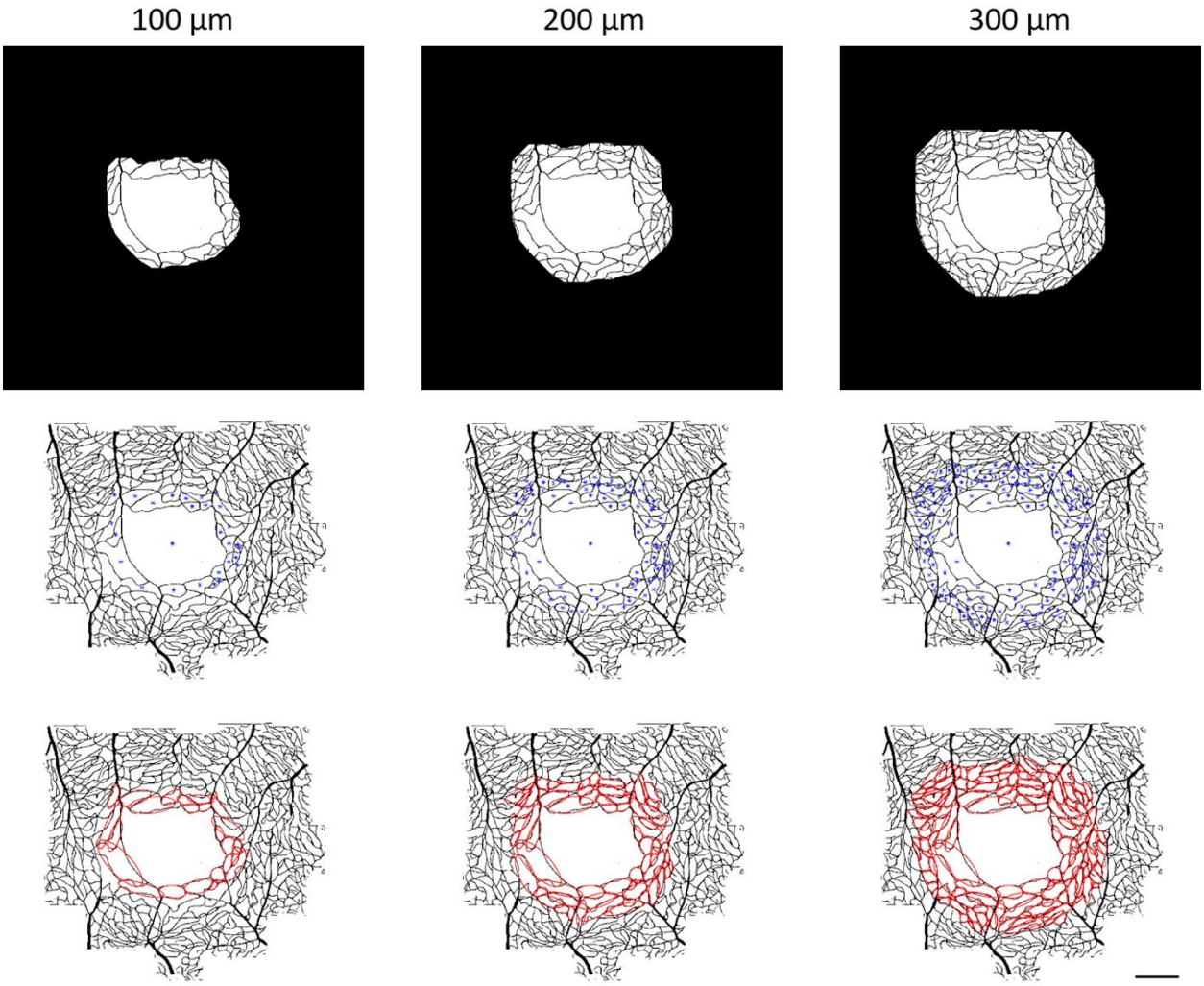

Figure 4-2. Sequence of images from a representative healthy adult eye illustrating the process for identifying and quantifying PICRs within 100 µm (leftmost column), 200 µm (middle column), and 300 µm (rightmost column) of the FAZ margin. (Top row) Masks created to remove capillaries located at a distance greater than 100 µm, 200 µm, and 300 µm from the FAZ margin. (Middle row) The centroids of the FAZ and each PICR contained within the given distance from the FAZ margin are marked with a blue asterisk in the montage. A greater number of PICRs are included when the size of the analysis zone increases. (Bottom row) Red ellipses are best-fit to those PICRs whose centroids were within the given distance from the FAZ margin. Scale bar: 300 µm.

4.2.2 Statistical Analysis

Data are presented as mean ± standard deviation. Pearson correlations were used to determine whether significant relationships between PICR metrics and axial length, and between PICR

metrics and FAZ metrics. A Kruskal-Wallis One-way ANOVA was used to compare PICR metrics between the three zone sizes (i.e., 100 µm, 200 µm, and 300 µm from the FAZ margin). A P value < 0.05 was considered statistically significant.

4.3 Results

Twenty-two eyes of 22 subjects (15 females, 7 males) were included in the study. The self-reported races/ethnicities of our subjects were White (n=10), Asian (n=11), and Hispanic (n=1). Subjects had a mean age of 27.1 ± 4.1 years (range: 22 to 36 years). The mean axial length for our subjects was 23.82 ± 1.18 mm (range: 22.47 to 26.70 mm), while the mean spherical equivalent refractive error was -0.73 ± 1.39 D (range: -3.68 D to +0.69 D). Mean FAZ area and circularity were 0.28 ± 0.10 mm^2 (range: 0.12 to 0.50 mm^2) and 0.62 ± 0.12 (range: 0.45 to 0.86), respectively.

Mean values of all analyzed PICR metrics are presented in Table 4-1 for the 3 zones of 100 µm, 200 µm, and 300 µm from the FAZ margin. PICR areas within the 100 µm zone were significantly larger than those areas for all PICRs contained within the 200 µm and 300 µm zones (Kruskal-Wallis One Way AVNOVA on ranks, Tukey Post-hoc, *P*<0.05). However, PICR

Table 4-1. Mean (± standard deviation) of PICR metrics across all subjects for the three zones of 100 µm, 200 µm, and 300 µm from the FAZ margin.

	Zone size		
	100 µm	**200 µm**	**300 µm**
PICR area ($µm^2$)	8,740 ± 3,435 *	5,842 ± 1,862	4,636 ± 1,114
PICR major axis (µm)	173.1 ± 47.3 *	136.6 ± 28.2	119.5 ± 17.8
PICR minor axis (µm)	62.7 ± 11.9 *	50.9 ± 7.9	46.1 ± 5.0
PICR axis ratio	2.84 ± 0.46	2.78 ± 0.37	2.69 ± 0.23
PICR circularity	0.56 ± 0.05	0.57 ± 0.04	0.57 ± 0.03

* Indicates a statistically significant difference for the 100 µm zone relative to the 200 µm and 300 µm zones (P < 0.05).

areas within the 200 µm and 300 µm zones were not significantly different from each other. The same relationships were also observed for PICR major and minor axes (Kruskal-Wallis One Way AVNOVA on ranks, Tukey Post-hoc, $P<0.05$). Conversely, PICR axis ratio and circularity were similar for all zones.

All PICR metrics were compared with the axial lengths of our subjects. While no PICR metric was correlated with axial length for PICRs within the 100 µm and 200 µm zones, eyes with longer axial lengths had significantly larger PICR areas ($r = 0.49$, $P = 0.02$) and values of PICR major axis ($r = 0.45$, $P = 0.04$) for PICRs within the 300 µm zone (Figure 4-3A,B). However, upon removal of the PICR values associated with the subject whose axial length was 26.7 mm, which is greater than 2 standard deviations from the mean axial length (or 26.18 mm), the aforementioned correlations were no longer significant ($r = 0.22$, $P = 0.33$ and $r = 0.23$, $P = 0.32$ for PICR area and major axis, respectively) (Figure 4-3C,D).

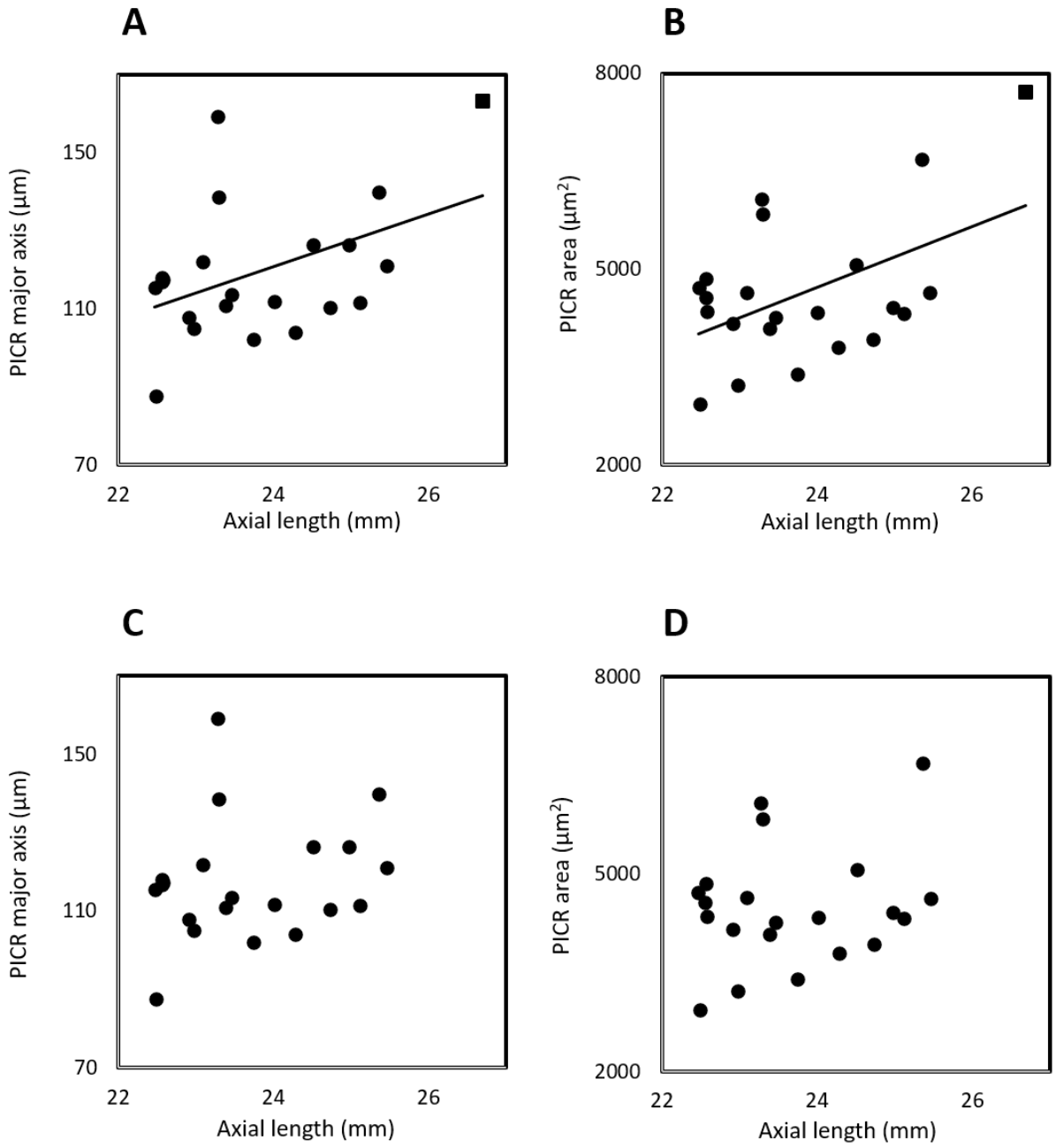

Figure 4-3. PICR major axis and area as a function of axial length for PICRs contained within the 300 µm zone. Solid lines show linear regressions for those data that possessed a statistically significant relationship. (A) Eyes with longer axial lengths tended to contain PICRs with significantly larger major axis lengths (r = 0.45, *P* = 0.04). (B) Eyes with longer axial lengths also contained PICRs with greater areas (r = 0.49, *P* = 0.02). (C, D) After removing the subject with an axial length of 26.7 mm, represented as the square data point in (A) and (B), there was no significant relationship between (C) PICR major axis (r = 0.22, *P* = 0.33) or (D) PICR area (r = 0.23, *P* = 0.32) and axial length.

We also compared PICR and FAZ metrics across subjects. FAZ area was not correlated with PICR area or PICR minor axis for any of the three zones. However, eyes with larger FAZ areas had more elliptically-shaped PICRs, as evidenced by decreased values of PICR circularity and increased PICR axis ratios (Figure 4-4). As FAZ area increased, PICR circularity significantly decreased for PICRs within all 3 zones (100 µm: r = -0.53, *P* = 0.012; 200 µm: r = -0.50, *P* = 0.017; 300 µm: r = -0.42, *P* = 0.048). Similarly, PICR axis ratio increased in eyes with larger FAZ area for PICRs within the 300 µm zone (r = 0.42, *P* = 0.0496), and nearly achieved significance for PICRs within the 100 µm (r = 0.41, *P* = 0.057) and 200 µm (r = 0.39, *P* = 0.07) zones. PICR major axis significantly increased in eyes with larger FAZ areas, but only for PICRs within the 200 µm and 300 µm zone (r = 0.45, *P* = 0.038 and r = 0.47, *P* = 0.03, respectively).

When comparing PICR metrics with FAZ circularity, we found that eyes with more circular FAZs (i.e., values of FAZ circularity that are closer to 1) had larger PICR major axes (r = 0.44, *P* = 0.04), increased PICR axis ratios (r = 0.49, *P* = 0.019), and decreased PICR circularity (r = -0.48, *P* = 0.02) for PICRs within the 100 µm zone. For PICRs within the 200 µm zone, only PICR axis ratio was significantly correlated with FAZ circularity, as eyes with more circular FAZs tended to contain PICRs with increased axis ratios (r = 0.50, *P* = 0.017).

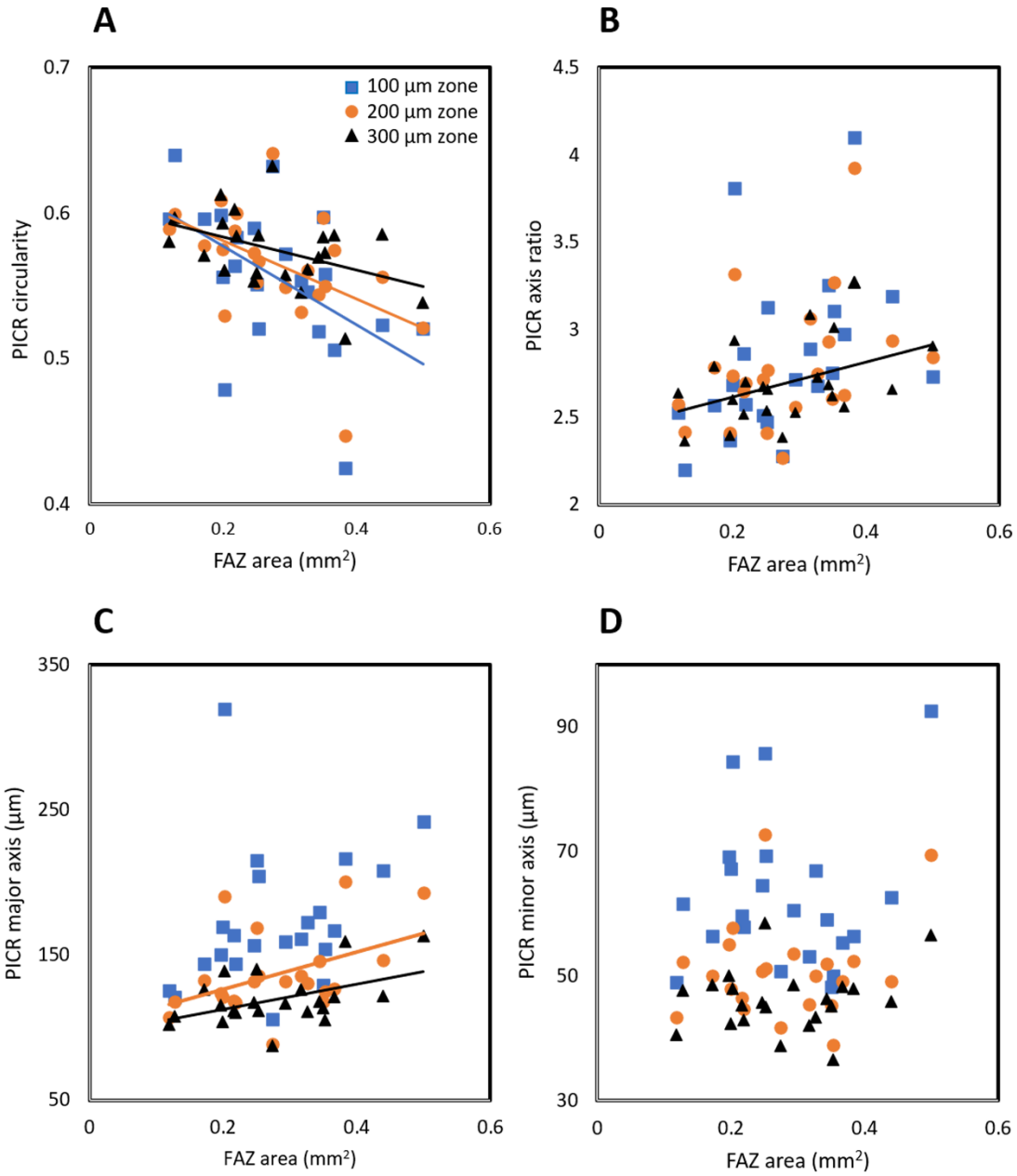

Figure 4-4. Comparisons of PICR metrics with FAZ area for all PICRs contained within 100 µm (blue squares), 200 µm (orange circles), and 300 µm (black triangles) of the FAZ margin. Lines show linear regressions for those data that possessed a statistically significant relationship. (A) PICR Circularity significantly decreased with increasing FAZ area for all 3 zones. (B) PICR axis ratio significantly increased for PICRs contained with the 300 µm zones. (C) PICR major axis significantly increased with increasing FAZ area for PICRs within the 200 µm and 300 µm zone. (D) There were no relationships between PICR minor axis and FAZ area for any zone.

4.4 Discussion

The purpose of this study was to quantify PICR metrics surrounding the margin of the FAZ in healthy adult eyes to determine whether PICR properties are related to an eye's axial length and/or FAZ structure. The minor axis and area for PICRs within the 100 µm zone were significantly larger than for PICRs contained within the 200 µm and 300 µm zones. While axial length was not correlated with any PICR metric for the 100 and 200 µm zones, PICR major axis and area increased in eyes with longer axial lengths for PICRs within the 300 µm zone. However, these relationships for the 300 µm zone were no longer significant after removing the myopic subject whose axial length was more than 2 standard deviations outside of the mean value. In addition, eyes with larger FAZ areas tended to have more elliptically-shaped PICRs.

Values of PICR minor axis and area measured in this study were higher than those reported previously using OCTA. Figure 4-5 compares PICR data obtained in our study with values obtained by Krawitz et al. (2018) in 19 healthy adults (mean age = 52 years) using an Avanti RTVue-XR OCTA imaging system (Optovue, Fremont, CA USA). The higher values of PICR minor axis and area obtained from AOSLO images could likely be attributed to the increased lateral resolution inherent in AOSLO imaging relative to OCTA. Capillaries have been shown to have larger lumen diameters in OCTA images compared to AOSLO fluorescein angiography and histological images (Mo et al., 2016; Tan et al., 2015). Larger capillary diameters would lead to smaller PICR areas and decreased PICR minor axes in OCTA-derived metrics. Moreover, due to the decreased lateral resolution and larger capillary diameters, it can be more challenging to accurately distinguish close-running capillaries in OCTA images compared to AOSLO images (Kaizu et al., 2017). Hence, one big PICR in an AOSLO image may appear as two smaller PICRs in an OCTA image (Figure 4-6).

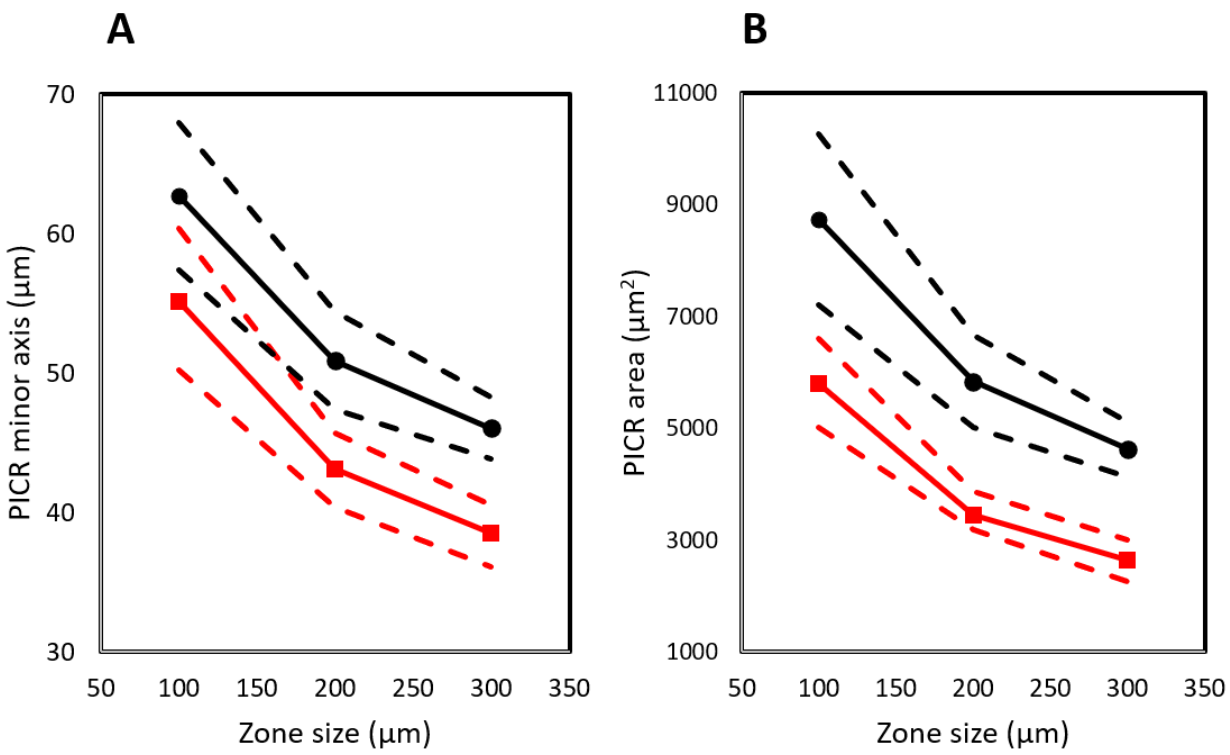

Figure 4-5. Values of PICR minor axis and area calculated in this study (black circles) tended to be higher than OCTA-derived values calculated by Krawitz et al. (2018) (red squares). Symbols represent mean values, while dashed lines represent 95% confidence intervals. (A) Mean PICR minor axis and (B) mean PICR area both decreased with increasing zone size from the FAZ margin.

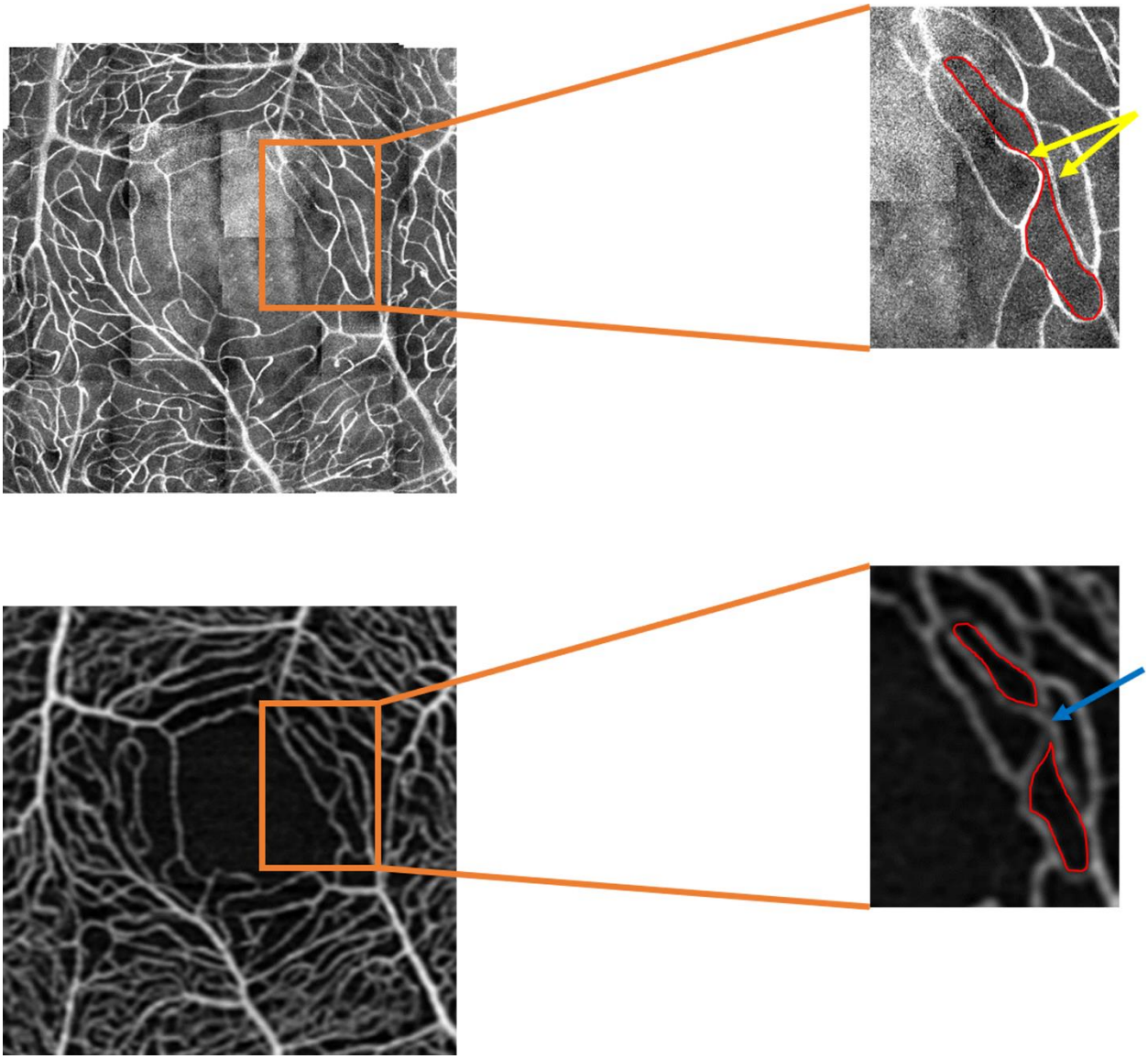

Figure 4-6. The increased lateral resolution afforded with adaptive optics imaging can improve the accuracy of delineating capillaries and quantifying PICRs relative to optical coherence tomography angiography (OCTA). (Top row) Maximum intensity projection image of vasculature surrounding the FAZ in a representative healthy adult eye created from two superficial focuses acquired with our AOSLO. (Bottom row) Averaged superficial OCTA image (segmented from the internal limiting membrane to the inner plexiform layer) acquired using the ZEISS Angioplex OCTA system (Zeiss Meditec. Inc, Oberkochen, Germany) in the same subject over the same region. Magnified images of the same region of interest are shown to the right of each larger montage (orange lines). Two separately resolved capillaries that pass very close to each other (close-running capillaries) in the AOSLO perfusion image (yellow arrows, top right image) appear to overlap or merge into a single capillary in the OCTA image (blue arrow). Consequently, the larger PICR from the AOSLO image (outlined in red) would be classified as 2 smaller PICRs (red outlines) in the OCTA image.

The PICR metrics calculated in this study provide a better understanding of microvessel geometry immediately surrounding the FAZ. Only a single layer of capillaries borders the FAZ, where the retina is typically thin. The average PICR minor axis for those capillaries closest to the FAZ margin (i.e., within the 100 µm zone) was 62 µm in our study, which is consistent with the optimal distance previously reported (~60 µm) for oxygen diffusion in the parafoveal area (Iwasaki & Inomata 1986; Chui et al., 2014). With increasing eccentricity from the FAZ margin, the thicknesses of inner retinal layers increase. Consequently, more than one vascular bed is needed to provide metabolic support for the retina. The presence of multiple vascular plexus would likely result in the appearance of smaller PICRs in *en face* AOSLO images, which are 2D projections of a 3D vascular structure. The fact that PICR minor axis and PICR area decreased with increasing distance from the FAZ margin in our subjects supports this idea. Further research could model the vasculature network surrounding the FAZ in 3 dimensions, potentially in a fashion similar to work done to quantify the size of lamina cribrosa beams and pores in 3 dimensions (Lockwood et al., 2015), and examine whether the volume of tissue between capillaries changes at different distances from the FAZ margin.

PICR metrics were not correlated with axial length, suggesting that factors other than axial length dictate intercapillary spacing. Axial elongation is thought to alter retinal structure, such as the density of photoreceptors and retinal thickness, by exerting mechanical forces that stretch the retina. Although FAZ size and shape are not correlated with axial length in healthy individuals (Dubis et al., 2012; Fujiwara et al., 2017), some studies have reported differences in the retinal microvascular network with axial length, including reduced macular vessel density in highly myopic eyes (Yang et al., 2016; Li et al., 2017; Leng et al., 2018). However, at least two points need to be considered when interpreting these results. First, some studies have not corrected for the effects of retinal magnification on retinal images due to differences in axial length (Leng et al., 2018), which serves to confound the reported results (Sampson et al., 2017).

In addition, despite the wide use of vessel density as a metric for assessing vascular properties and changes, vessel density is not sensitive at detecting small capillary changes (Salz et al., 2016; Schottenhamml et al., 2016). Given that PICR metrics have been suggested to be more sensitive than vessel density at detecting small capillary changes (Schottenhamml et al., 2016), we investigated capillary network structure by quantifying PICRs in AOSLO images that were scaled based on each individual's biometric measurements. As part of this work, we hypothesized that retinal stretching associated with axial elongation would affects vascular structure such that eyes with longer axial lengths would also have increased PICR minor axes, potentially impacting the ability of the retina to be adequately oxygenated and nourished. However, we found no significant relationship between PICR minor axis (or PICR major axis and area, after removing the subject with the longest axial length) and axial length in our subjects for any zone, implying that factors other than axial length likely play a more prevalent role in dictating capillary network geometry near the FAZ.

When examining PICR major axis and PICR area across all subjects, we initially found a significant relationship between these parameters and axial length for PICRs within the 300 µm zone. Interestingly, these correlations disappeared after removing the subject whose axial length was more than 2 standard deviations from the mean value (26.7 mm) and may have been classified as a high myope (i.e., having an axial length greater than 26 mm) (Zhang et al., 2016; Wan et al., 2018). One potential limitation of this study is the lack of more eyes with longer axial lengths. While the range of axial lengths examined in this studied was relatively broad (22.47 mm to 26.70 mm), the second highest axial length (25.46 mm) was 1.24 mm shorter than the maximum value of 26.70 mm. Future studies may include eyes with larger axial lengths to investigate whether these relationships hold.

The decreased values of PICR circularity and increased values of PICR axis ratio measured in our subjects indicate that PICRs tended to be more elliptical in eyes with larger

FAZ areas. Conversely, eyes with smaller FAZ areas tended to have increased values of PICR circularity and decreased values of PICR axis ratio, or more circularly-shaped PICRs. We believe this relationship can potentially be explained by considering the relationships known to occur between FAZ area, foveal pit depth, and retinal thickness. Smaller FAZs area have been shown to occur in eyes with shallower foveal pits (Chui et al., 2012; Dubis et al., 2012), thicker central maculas (Samara et al., 2015), thicker central foveas (Chui et al., 2012), and increased foveal inner retinal thicknesses (Yu et al., 2016). Eyes with thicker inner retinas are likely to experience higher metabolic demands and possess vessels that penetrate more deeply into the retina. As these vessels turn to travel horizontally in the retina, it is possible that vessels located at different depths may appear to cross over each other in a 2D projection image, yielding more fragmented PICRs with smaller areas and perimeters. As can be seen in Eqn. 4.1, PICR circularity is directly proportional to PICR area, but inversely proportional to the *square* of the PICR perimeter. Therefore, changes in PICR perimeter have more effect on circularity compared to changes in area. Based on this model, more fragmented PICRs (with smaller perimeters) in eyes with smaller FAZs would lead to higher values of PICR circularity, which was observed in our subjects.

The relationship between FAZ area and PICR geometry may affect vascular density measurements around the FAZ. Vessel density is a commonly used metric to quantitatively evaluate vascular networks and their abnormalities (Al-Sheikh et al., 2016; Wei et al., 2017; Ciloglu et al., 2019). However, different definitions of “vessel density” exist in the literature. The most common method for determining vessel density is to calculate the percentage of retinal area (usually, within a 3 x 3-mm square that is centered on the fovea) that is occupied by perfused vessels (Borrelli et al., 2018; Roberts et al., 2019; Wang et al., 2019). A drawback of this method is that it does not exclude the area within the FAZ, which may lead to higher vessel density values for eyes with a smaller FAZ area compared to eyes with larger FAZ areas.

Some studies have quantified vessel density in annuli of various sizes from the FAZ margin to account for variations in FAZ size (Tam et al., 2010; Romo et al., 2019). Although this latter method excludes pixels inside the FAZ margin and standardizes the region that is analyzed across subjects, vessel density measurements could still be affected if there is a relationship between FAZ area and PICR area. For example, if PICR area was smaller in eyes with smaller FAZs, then vessel density measurements could also be larger in eyes with smaller FAZs within a fixed annulus from the FAZ margin. While no direct relationship was found between FAZ area and PICR area in our subjects, we did observe that eyes with smaller FAZ areas have more circular PICRs, and eyes with more circular PICRs have decreased PICR areas (100 µm: r = -0.55, $P = 0.008$; 200 µm: r = -0.64, $P = 0.001$; 300 µm: r = -0.63, $P = 0.002$) and eyes with decreased PICR areas have increased vessel density (100 µm: r = -0.81, $P < 0.001$; 200 µm: r = -0.81, $P < 0.001$; 300 µm: r = -0.74, $P < 0.001$). Further studies are required to determine whether vessel density measurements need to take into account the area of the FAZ and the geometry of its PICRs.

In conclusion, we used an AOSLO to image vasculature around the FAZ in heathy adult eyes and quantified PICR metrics in zones as large as 300 µm from the FAZ margin to examine the effect of axial length and FAZ structure on PICR geometry. We measured larger values of PICR minor axis and area compared to OCTA-derived metrics, potentially because of the higher lateral resolution inherent in our AOSLO system. PICR minor axis and axial length were not correlated, implying that the optimal distance for oxygen diffusion is preserved across eyes with different axial lengths. Additionally, eyes with smaller FAZ areas had more circularly shaped PICRs. However, it remains unclear whether FAZ and PICR geometry influence measures of vessel density.

4.5 Acknowledgements

This research was supported by National Institutes of Health (NIH) Grant P30 EY007551 and the University of Houston College of Optometry. The authors thank Mindy Fox for her contribution in data collection. We also thank Nimesh Patel for his helpful discussion.

CHAPTER 5

General Conclusions

5.1 General conclusion

The fovea is a specialized region of the retina that plays an important role in visual function. This region has unique characteristics which differentiate it from other parts of the retina. It is typically characterized by increased cone density, excavation of inner retinal layers (forming the foveal pit), and a capillary-free region known as the foveal avascular zone (FAZ). The geometry of the fovea is thought to be affected by different factors, including axial length. Axial elongation exerts mechanical forces on the retina and can lead to retinal stretching, which may impact foveal geometry and, consequently, visual function. Several studies have investigated the effect of axial elongation on individual foveal structures (Chui et al., 2008a; Dubis et al., 2009; Lombardo et al., 2012). However, the simultaneous examination of multiple foveal structures altogether provides a more comprehensive picture of foveal anatomy. The experiments carried out in this work were designed to provide a more detailed understanding of the impact of axial elongation on foveal structure in the eyes of healthy adults (chapter 2) and children (chapter 3). In addition, the impact of axial elongation on intercapillary spacing within the microvascular network surrounding the FAZ was investigated (chapter 4).

5.1.1 Experiment 1 (Chapter 2): Determine whether differences exist in overall foveal architecture (cone packing, FAZ, and foveal pit metrics) between healthy adult eyes with long and short axial lengths

Retinal stretching associated with axial elongation is one of the factors that has been suggested to affect foveal morphometry and the packing of cones. While several studies have separately investigated potential differences in cone packing and foveal pit geometry between emmetropes and myopes (Chui et al., 2008a; Dubis et al., 2009; Lombardo et al., 2012), ocular determinants of refractive error could have masked any effects found due to axial length. Moreover, less is known about the relationship of cone packing with foveal pit and FAZ parameters in the same

eyes (Wilk et al., 2016). We sought to more comprehensively understand whether relationships exist between foveal structure and axial length by examining and comparing FAZ, foveal pit, and cone packing metrics between healthy adult eyes with short and long axial lengths, as well as between other foveal metrics.

Eyes with short and long axial lengths did not have significantly different FAZ or foveal pit metrics. Our results were consistent with previous findings showing no relationship between FAZ size and axial length (Chui et al., 2014; Fujiwara et al., 2017; Wen et al., 2019) and corroborate reports finding no significant differences in the shape of the foveal pit between myopic and emmetropic subjects (Dubis et al., 2009). Linear cone density was lower and metrics of cone spacing (including farthest neighbor, nearest neighbor, and intercell distances) were greater in the long axial length group across all eccentricities. These results indicate that axial elongation alters cone packing at the examined eccentricities. In addition, eyes in the long axial length group that possessed larger FAZ areas had larger pit volumes, areas, and diameters. However, no relationships were observed between cone density and FAZ area or foveal pit volume.

Our findings, coupled with those from other studies, imply that different factors govern the geometry of different foveal features. Retinal stretching likely affects the arrangement of cones, whereas FAZ and foveal pit structure may primarily be shaped by factors other than axial length.

5.1.2 Experiment 2 (Chapter 3): Determine whether differences exist in overall foveal structure as a function of age and refractive status in eyes of healthy children

Ex vivo and *in vivo* studies have shown that the fovea is not fully developed at birth and suggest that some aspects of the fovea continue to develop and mature throughout childhood into the early teenage years (Yuodelis & Hendrickson, 1986; Vajzovic et al., 2012; Lee et al., 2015;

Read et al., 2015). Although most postnatal changes are attributed to the maturation and migration of cone photoreceptors, studies on cone density in children are sparse. Moreover, myopia usually develops during childhood. Yet, most of what is known regarding myopia-related differences in cone density and foveal pit morphometry comes from studies conducted in the adult retina. The purpose of this study was to determine whether differences exist in overall foveal structure, including cone density and spacing, FAZ size, and foveal pit shape, as a function of age and refractive status in children.

No relationships were observed between FAZ, foveal pit, or cone density and spacing metrics with age (after controlling for the effect of axial length). In addition, mean values of the examined metrics were comparable to values reported for adults in previous studies. Taken together, these results suggest that age-related changes may happen by a younger age or at a slower rate compared to first few years of life. FAZ and foveal pit metrics were not significantly different between myopic and non-myopic eyes. However, in myopic children, linear cone density was significantly lower at 0.2 and 0.3 mm eccentricities relative to densities in non-myopic children. Across all eccentricities, angular cone density and farthest neighbor distance were significantly higher in the myopic group compared to the non-myopic group. Consistent with histological and *in vivo* studies in adults, we observed asymmetry in cone density and spacing along the horizontal and vertical meridians. At 0.2 mm eccentricity, eyes with longer axial lengths had significantly lower linear cone densities and increased farthest neighbor distance.

In conclusion, this study is significant in that it is the first study to report *in vivo* cone densities in a group of children as young as 5.8 years old at retinal eccentricities as close as 0.2 mm from the foveal center. Furthermore, our measures of FAZ geometry, foveal pit morphometry, and cone density and spacing in the same eyes provides a more comprehensive assessment of the foveal region in children.

5.1.3 Experiment 3 (Chapter 4): Determine whether differences exist in capillary geometry immediately surrounding the FAZ border as a function of axial length and FAZ structure in healthy adult eyes

Understanding factors that determine the geometry of vessels bordering the FAZ is important in that the capillary network is single-layered at this region and changes to the spacing between capillaries (or intercapillary distances) may impact oxygenation of the inner retina. It is still unclear whether the topography of the foveal microvascular network is related to an eye's length or other foveal properties. The purposes of this study were to quantify parafoveal intercapillary region (PICR) metrics for capillaries neighboring the margin of the FAZ in healthy adult eyes and to determine whether these metrics are different as a function of eye's axial length and FAZ structure in an attempt to better understand foveal microvascular geometry.

Mean PICR minor axis for PICRs within a 100 µm zone from the FAZ margin was 62 µm, which agrees with the optimal distance (~60 µm) reported for oxygen diffusion (Iwasaki & Inomata, 1986; Chui et al., 2014). With increasing distance from the FAZ margin, PICR minor axis and area decreased, potentially due to the increasing thickness of inner retinal layers and the presence of more than one vascular layer. Our values for PICR minor axis and area were higher compared to previously published studies using OCTA (Krawitz et al., 2018). We believe these differences may stem from differences in the lateral resolution inherent between AOSLO and OCTA imaging. We did not observe any significant relationship between PICR minor axis and axial length, which suggests that factors other than axial elongation contribute to capillary spacing near the FAZ. Eyes with longer axial lengths had larger values of PICR major axis and area. However, more subjects with longer axial lengths are needed to confirm this observation. Eyes with smaller FAZ areas had more circularly-shaped PICRs.

To conclude, our examination of the arrangement of the microvasculature immediately surrounding the FAZ in healthy adult eyes suggests that factors other than retinal stretching primarily drive intercapillary spacing.

5.2 Summary and future directions

High resolution *in vivo* retinal imaging has improved our understanding of retinal anatomy and potential factors that drive its formation. We combined AOSLO and OCT imaging in the experiments described in Chapters 2 and 3 to provide a more comprehensive picture of foveal structural properties in healthy adults and children. We also capitalized on the high resolution imaging capabilities of our AOSLO instrument to better characterize perfused capillary structure surrounding the FAZ in healthy adult eyes.

Despite the high lateral resolution of our AOSLO system (approximately 2.5 μm), the closest eccentricity for which cones could be reliably counted in all subjects for Chapter 2 was at 0.15 mm from the foveal center. Future work could focus on imaging the central-most foveal cones (potentially by using shorter wavelength illumination, a smaller imaging field size, and other technical improvements) to determine peak cone density and see whether it differs in eyes with short versus long axial lengths.

Performing AOLSO imaging in children is not an easy task as it requires children to cooperate, sit still, and maintain fixation. Despite these challenges, the study outlined in Chapter 3 demonstrates our ability to successfully image a cohort of children as young as 5.8 years old using our AOSLO system at eccentricities as close as 0.2 mm form the foveal center. Given that many of the foveal metrics we examined were similar in magnitude to measurements recorded in adult eyes, it would be interesting to image children younger than 5.8 years to see whether age and foveal metrics are related in younger eyes. One could also design a longitudinal experiment that would quantify foveal metrics in the same children with the goal of better

clarifying age-related changes in photoreceptor distribution and foveal pit shape during the processes of emmetropization and the development of myopia.

The experiment described in Chapter 4 used our AOSLO system to image superficial vasculature surrounding the FAZ in healthy adult eyes. However, the same location was also imaged with the Cirrus OCTA system in all subjects (data not reported). A qualitative and quantitative comparison between values obtained from AOSLO and OCTA images would be interesting and challenging. One challenge would be the co-registration of AOSLO and OCTA perfusion images, as OCTA can be more prone to eye motion artifacts. Although 10 consecutive OCTA scans (~ 3x3 mm centered at the fovea) were acquired to make an averaged OCTA perfusion image, we still found the co-registration process to be arduous. Moreover, it would be interesting to quantify PICR metrics at four separate quadrants (superior, inferior, nasal, temporal) and investigate whether relationships exist between axial length and PICR metrics at the level of individual quadrants, as there might be an asymmetry in the mechanical forces associated with axial elongation. Additionally, it would be of interest to better understand whether the relationship between FAZ size and PICR geometry affect vessel density measurements.

Ultimately, any structural imaging and analysis should be combined with functional measures to elucidate the extent to which structural changes associated with axial elongation impact retinal and visual function. Particularly, it is of interest to know how differences in the packing of the cones or the shape of the foveal pit are associated with resolution, acuity, or contrast sensitivity.

REFERENCES

Al-Sheikh M, Akil H, Pfau M, Sadda SR. Swept-Source OCT Angiography Imaging of the Foveal Avascular Zone and Macular Capillary Network Density in Diabetic Retinopathy. *Invest Ophthalmol Vis Sci*. 2016;57(8):3907-3913.

ANSI. American National Standard for Safe Use of Lasers (ANSI Z136.1-2014). The laser institue of America. 2014.

Benjamini Y, Hochberg Y. Controlling the False Discovery Rate: A Practical and Powerful Approach to Multiple Testing. *J R Stat Soc Ser B.* 1995;57:289–300.

Borrelli E, Lonngi M, Balasubramanian S, Tepelus TC, Baghdasaryan E, Iafe NA, Pineles SL, Velez FG, Sarraf D, Sadda SR, Tsui I. Macular microvascular networks in the healthy pediatrics subjects. *Retina*. 2019;39(6):1216-1224.

Brown NP, Koretz JF, Bron AJ. The development and maintenance of emmetropia. *Eye.* 1999;13:83.

Bruce A, Pacey IE, Bradbury JA, Scally AJ, Barrett BT. Bilateral changes in foveal structure in individuals with amblyopia. *Ophthalmology*. 2013;120:395–403.

Bullimore MA, Gilmartin B, Royston JM. Steady-state accommodation and ocular biometry in late-onset myopia. *Doc Ophthalmol*. 1992;80:143–55.

Chan G, Balaratnasingam C, Yu PK, Morgan WH, Mcallister IL, Cringle SJ, Yu D-Y. Quantitative morphometry of perifoveal capillary networks in the human retina. *Invest Ophthalmol Vis Sci.* 2012;53:5502–14.

Chan G, Balaratnasingam C, Xu J, Mammo Z, Han S, Mackenzie P, Merkur A, Kirker A, Albini D, Sarunic MV, Yu D-Y. In vivo optical imaging of human retinal capillary networks using speckle variance optical coherence tomography with quantitative clinico-histological correlation. *Microvasc Res.* 2015;100:32–9.

Chen TC, Cense B, Pierce MC, Nassif N, Park BH, Yun SH, White BR, Bouma BE, Tearny GJ, de Boer JF. Spectral Domain Optical Coherence Tomography: Ultra-high Speed, Ultra-high Resolution Ophthalmic Imaging. *Arch Ophthalmol.* 2005;123:1715–20.

Chen J, Liu C-H, Sapieha P. Retinal vascular development. In: Stahl A. *Anti-Angiogenic Therapy in Ophthalmology*. 1st ed. Switzerland: Springer international Publishing, 2016; 1-19

Cheung CY, Li J, Yuan N, Lau GYL, Chan AYF, Lam A, Tang FY, Tham CC, Pang CP, Chen LJ, Yam JC. Quantitative retinal microvasculature in children using swept-source optical coherence tomography: the Hong Kong Children Eye Study. *Br J Ophthalmol.* 2019;103:672.

Chui TYP, Song H, Burns SA. Individual variations in human cone photoreceptor packing density: Variations with refractive error. *Invest Ophthalmol Vis Sci.* 2008a;49:4679–87.

Chui T, Song H, Burns SA. Adaptive-optics imaging of human cone photoreceptor distribution. *J Opt Soc Am A-Optics Image Sci Vis* 2008b;25:3021–9.

Chui Toco Y. P, Zhong Zhangyi A, Song Hongxin A, Burns Stephen A. Foveal Avascular

Zone and Its Relationship to Foveal Pit Shape. *Optom Vis Sci.* 2012;89:602–10.

Chui TYP, VanNasdale DA, Elsner AE, Burns SA. The association between the foveal avascular zone and retinal thickness. *Invest Ophthalmol Vis Sci.* 2014;55:6870–7.

Ciloglu E, Unal F, Sukgen EA, Koçluk Y. Evaluation of Foveal Avascular Zone and Capillary Plexuses in Diabetic Patients by Optical Coherence Tomography Angiography. *Korean J Ophthalmol*. 2019;33(4):359-365.

Coletta NJ, Watson T. Effect of myopia on visual acuity measured with laser interference fringes. *Vision Res.* 2006;46:636–51.

Cooper RF, Wilk MA, Tarima S, Carroll J. Evaluating descriptive metrics of the human cone mosaic. *Invest Ophthalmol Vis Sci.* 2016;57:2992–3001.

Cornish EE, Madigan MC, Natoli R, Hales Angela, Hendrickson AE, provis JM. Gradients of cone differentiation and FGF expression during development of the foveal depression in macaque retina. *Vis Neurosci.* 2005;22:447–59.

Curcio CA, Sloan KR, Kalina RE, Hendrickson AE. Human photoreceptor topography. *J Comp Neurol.* 1990;292:497–523.

Curtin BJ. The myopias : basic science and clinical management . Philadelphia: Harper & Row; 1985.

Delori FC, Webb RH, Sliney DH. Maximum permissible exposures for ocular safety (ANSI 2000), with emphasis on ophthalmic devices. *J Opt Soc Am A Opt Image Sci Vis.* 2007;24:1250–65.

Diaz-Araya C, Provis JM. Evidence of photoreceptor migration during early foveal development: A quantitative analysis of human fetal retinae. *Vis Neurosci.* 1992;8:505–14.

Diaz-Araya CM, Provis JM, Billson FA. NADPH-diaphorase histochemistry reveals cone distributions in adult human retinae. *Aust N Z J Ophthalmol.* 1993;21:171—179.

Dubis AM, McAllister JT, Carroll J. Reconstructing foveal pit morphology from optical coherence tomography imaging. *Br J Ophthalmol.* 2009;93:1223–7.

Dubis AM, Hansen BR, Cooper RF, Beringer J, Dubra A, Carroll J. Relationship between the foveal avascular zone and foveal pit morphology. *Invest Ophthalmol Vis Sci.* 2012;53:1628–36.

Dubis AM. Characterizing foveal morphology in the normal and diseased retina. The Medical College of Wisconsin; 2012.

Dubra A, Harvey Z. Registration of 2D images from fast scanning ophthalmic instruments. *Lect Notes Comput Sci (Including Subser Lect Notes Artif Intell Lect Notes Bioinformatics).* 2010:60–71.

Elsner AE, Chui TYP, Feng L, Song HX, Papay JA, Burns SA. Distribution differences of macular cones measured by AOSLO : Variation in slope from fovea to periphery more

pronounced than differences in total cones. *Vision Res.* 2017;132:62–8.

Falavarjani K, Shenazandi H, Naseri D, Anvari P, Kazemi P, Aghamohammadi F, Alissmail F, Alemzadeh SA. Foveal avascular zone and vessel density in healthy subjects: An optical coherence tomography angiography study. *J Ophthalmic Vis Res.* 2018;13:260–5.

Friedman NE, Mutti DO, Zadnik K. Corneal changes in schoolchildren. *Optom Vis Sci.* 1996;73:552—557.

Fujiwara A, Morizane Y, Hosokawa M, Kimura S, Shiode Y, Hirano M, Doi S, Toshima S, Takahashi K, Hosogi M, Shiraga F. Factors affecting foveal avascular zone in healthy eyes: An examination using swept-source optical coherence tomography angiography. *PLoS One.* 2017;12:e0188572.

Gilmartin B. Myopia: Precedents for research in the twenty-first century. *Clin Exp Ophthalmol.* 2004;32:305–24.

Gołębiewska J, Biała-Gosek K, Czeszyk A, Hautz W. Optical coherence tomography angiography of superficial retinal vessel density and foveal avascular zone in myopic children. *PLoS One.* 2019;14:1–9.

Grosvenor T, Scott R. Three-year changes in refraction and its components in youth-onset and early adult-onset myopia. *Optom Vis Sci Off Publ Am Acad Optom.* 1993;70:677–83.

Han JC, Ko H, Kim SH, Rhee T, Nam SW, Hwang S, Lee GI, Sung J, Song YM, Kee C. Heritability of the morphology of optic nerve head and surrounding structures: The Healthy Twin Study. *PLoS One.* 2017;12:e0187498.

Hendrickson AE, Yuodelis C. The Morphological Development of the Human Fovea. *Ophthalmology.* 1984;91:603–12.

Hendrickson A. A morphological comparison of foveal development in man and monkey. *Eye.* 1992;6:136–44.

Hendrickson A. Organization of the adult primate fovea. In: Penfold PL, Provis JM, eds. *Macular degeneration*. Springer, Berlin, Heidelberg. 2005; 1-25

Hendrickson A, Possin D, Vajzovic L, Toth CA. Histologic Development of the Human Fovea From Midgestation to Maturity. *AJOPHT.* 2012;154:767-778.e2.

Hirsch J, Curcio CA. The spatial resolution capacity of human foveal retina. *Vision Res.* 1989;29:1095–101.

Holden BA, Fricke TR, Wilson DA, Jong M, Naidoo KS, Sankaridurg P, Wong TY, Naduvilath TJ, Resnikoff S. Global Prevalence of Myopia and High Myopia and Temporal Trends from 2000 through 2050. *Ophthalmology.* 2016;123:1036–42.

Hou W, Norton TT, Hyman L, Gwiazda J, Group C. Axial Elongation in Myopic Children and its Association With Myopia Progression in the Correction of Myopia Evaluation Trial. *Eye Contact Lens.* 2018;44:248–59.

Hsu ST, Ngo HT, Stinnett SS, Cheung NL, House RJ, Kelly MP, Chen X, Enyedi LB, Prakalapakorn SG, Materin MA, El-Dairi MA, Jaffe GJ, Freedman SF, Toth CA, Vajzovic L. Assessment of Macular Microvasculature in Healthy Eyes of Infants and Children Using OCT Angiography. *Ophthalmology.* 2019;126:1703–11.

Hu M-K. Visual pattern recognition by moment invariants. *IRE Trans Inf Theory.* 1962;8:179–87.

Huang D, Swanson EA, Lin CP, Schuman JS, Stinson WG, Chang W, Hee MR, Flotte T, Gregory K, Puliafito CA, et al. Optical coherence tomography. *Science.* 1991;254:1178–81.

Huang W, Duan A, Qi Y. Posterior scleral reinforcement to prevent progression of high Myopia. *Asia-Pacific J Ophthalmol*. 2019;8:366–70..

Insler MS, Cooper HD, May SE, Donzis PB. Analysis of corneal thickness and corneal curvature in infants. *CLAO J Off Publ Contact Lens Assoc Ophthalmol Inc.* 1987;13:182–4.

Ivers KM, Li C, Patel N, Sredar N, Luo X, Queener H, Harwerth RS, Porter J. Reproducibility of measuring lamina cribrosa pore geometry in human and nonhuman primates with in vivo adaptive optics imaging. *Invest Ophthalmol Vis Sci.* 2011;52:5473–80.

Iwasaki M, Inomata H. Relation between superficial capillaries and foveal structures in the human retina. *Invest Ophthalmol Vis Sci.* 1986;27:1698–705.

Jonas J, Schneider U, Naumann G. Count and density of human retinal photoreceptors. *Graefe's Arch Clin Exp Ophthalmol.* 1992;230:505–10.

Kozulin P, Natoli R, O'Brien K, Madigan MC, Provis J. Differential expression of anti-angiogenic factors and guidance genes in the developing macula. *Mol Vis.* 2009a:45–59.

Kozulin P, Natoli R, Madigan MC, O'Brien KM, Provis JM. Gradients of Eph-A6 expression in primate retina suggest roles in both vascular and axon guidance. *Mol Vis.* 2009b;15:2649–62.

Kozulin P, Natoli R, Bumsted O'Brien KM, Madigan MC, Provis JM. The cellular expression of antiangiogenic factors in fetal primate macula. *Invest Ophthalmol Vis Sci.* 2010;51:4298–306.

Kaizu Y, Nakao S, Wada I, Yamaguchi M, Fujiwara K, Yoshida S, Hisatomi T, Ikeda Y, Hayami T, Ishibashi T, Sonoda KH.. Imaging of Retinal Vascular Layers : Adaptive Optics Scanning Laser Ophthalmoscopy Versus Optical Coherence Tomography Angiography. *Trans Vis Sci Tech*. 2017;6(5):2.

Krawitz BD, Phillips E, Bavier RD, Mo S, Carroll J, Rosen RB, Chui TYP. Parafoveal Nonperfusion Analysis in Diabetic Retinopathy Using Optical Coherence Tomography Angiography. *Trans Vis Sci Techl.* 2018; 7(4):4.

Larsen JS. The sagittal growth of the eye. IV. Ultrasonic measurement of the axial length of the eye from birth to puberty. *Acta Ophthalmol (Copenh)*. 1971;49(6):873-886.

Le Grand Y, El Hage SG. Optics of the eye. In: *Physiological Optics.* Springer, Berlin, Heidelberg; 1980. 57–69.

Lee H, Purohit R, Patel A, Papageorgiou E, Sheth V, Maconachie G, Pilat A, McLean RJ, Proudlock FA, Gottlob I. In vivo foveal development using optical coherence tomography. *Invest Ophthalmol Vis Sci.* 2015;56:4537–45.

Legras R, Gaudric A, Woog K. Distribution of cone density, spacing and arrangement in adult healthy retinas with adaptive optics flood illumination.(Research Article). *PLoS One.* 2018;13:e0191141.

Leng Y, Tam EK, Falavarjani KG, Tsui I. Effect of Age and Myopia on Retinal Microvasculature. *Ophthalmic Surg Lasers Imaging Retina.* 2018;49:925.

Li KY, Roorda A. Automated identification of cone photoreceptors in adaptive optics retinal images. *J Opt Soc Am A Opt Image Sci Vis.* 2007;24:1358–63.

Li KY, Tiruveedhula P, Roorda A. Intersubject variability of foveal cone photoreceptor density in relation to eye length. *Invest Ophthalmol Vis Sci.* 2010;51:6858–67.

Li M, Yang Y, Jiang H, Gregori G, Roisman L, Zheng F, Ke B, Qu D, Wang J. Retinal Microvascular Network and Microcirculation Assessments in High Myopia. *Am J Ophthalmol.* 2017;174:56–67.

Liang J, Williams DR, Miller DT. Supernormal vision and high-resolution retinal imaging through adaptive optics. *J Opt Soc Am A Opt Image Sci Vis.* 1997;14:2884–92.

Linberg KA, Fisher SK. A burst of differentiation in the outer posterior retina of the eleven-week human fetus: An ultrastructural study. *Vis Neurosci.* 1990;5:43–60.

Linderman RE, Muthiah MN, Omoba SB, Litts KM, Tarima S, Visotcky A, Kim JE, Carroll J.. Variability of foveal avascular zone metrics derived from optical coherence tomography angiography images. *Trans Vis Sci Tech.* 2018;7(5):20

Linderman R, Salmon AE, Strampe M, Russillo M, Carroll J. Assessing the Accuracy of Foveal Avascular Zone Measurements Using Optical Coherence Tomography Angiography : Segmentation and Scaling. *Trans Vis Sci Tech*. 2017;6(3):16.

Llorente L, Barbero S, Cano D, Dorronsoro C, Marcos S. Myopic versus hyperopic eyes: axial length, corneal shape and optical aberrations. *J Vis.* 2004;4:288–98.

Lockwood H, Reynaud J, Gardiner S, Grimm J, Libertiaux V, Downs JC ,Yang H, Burgoyne CF. Lamina cribrosa microarchitecture in normal monkey eyes part 1: methods and initial results. *Invest Ophthalmol Vis Sci*. 2015;56(3):1618-1637.

Lombardo M, Serrao S, Ducoli P, Lombardo G. Variations in image optical quality of the eye and the sampling limit of resolution of the cone mosaic with axial length in young adults. *J Cataract Refract Surg.* 2012;38:1147–55.

Lombardo M, Serrao S, Ducoli P, Lombardo G. Eccentricity dependent changes of density, spacing and packing arrangement of parafoveal cones. *Ophthalmic Physiol Opt.* 2013;33:516–26.

Mason C, Kandel ER. Central visual pathways. In: Kandel ER, Schwarz JH, Jessell TM, eds. *Principles of Neural Science*. Appleton & Lange, Norwalk, Connecticult. 1991; 420-439.

Marmor MF, Choi SS, Zawadzki RJ, Werner JS. Visual Insignificance of the Foveal Pit: Reassessment of Foveal Hypoplasia as Fovea Plana. *Arch Ophthalmol.* 2008;126:907–13.

Martin GR. The eye of a passeriform bird, the European starling (Sturnus vulgaris): eye movement amplitude, visual fields and schematic optics. *J Comp Physiol A.* 1986;159:545–57.

Mcallister JT, Dubis AM, Tait DM, Ostler S, Rha J, Stepien KE, Summers CG, Carroll J. Arrested development: High-resolution imaging of foveal morphology in albinism. *Vision Res.* 2010;50:810–7.

McBrien NA, Millodot M. A biometric investigation of late onset myopic eyes. *Acta Ophthalmol.* 1987;65:461–8.

Meijering E, Jacob M, Sarria J -C. F, Steiner P, Hirling H, Unser M. Design and validation of a tool for neurite tracing and analysis in fluorescence microscopy images. *Cytom Part A.* 2004;58:167–76.

Mirhajianmoghadam H, Jnawali A, Musial G, Queener HM, Patel NB, Ostrin LA, J Porter. In vivo assessment of foveal geometry and cone photoreceptor density and spacing in children. *Sci Rep.* 2020;10:8942.

Mo S, Krawitz B, Efstathiadis E, Geyman L, Weitz R, Chui TYP, Carroll J, Dubra A, Rosen RB. Imaging Foveal Microvasculature: Optical Coherence Tomography Angiography Versus Adaptive Optics Scanning Light Ophthalmoscope Fluorescein Angiography. *Invest Ophthalmol Vis Sci.* 2016;57:OCT130–40.

Musial G, Queener HM, Adhikari S, Mirhajianmoghadam H, Schill AW, Patel NB, Porter J. Automatic segmentation of retinal capillaries in adaptive optics scanning laser ophthalmoscope perfusion images using a convolutional neural network. *Trans Vis Sci Tech*. 2020; 9:43.

Mutti DO, Zadnik K, Adams AJ. Myopia. The nature versus nurture debate goes on. *Invest Ophthalmol Vis Sci.* 1996;37:952–7.

Mutti DO, Zadnik K, Fusaro RE, Friedman NE, Sholtz RI, Adams AJ. Optical and structural development of the crystalline lens in childhood. *Invest Ophthalmol Vis Sci.* 1998;39:120–33.

Nesmith B, Gupta A, Strange T, Schaal Y, Schaal S. Mathematical analysis of the normal anatomy of the aging fovea. *Invest Ophthalmol Vis Sci.* 2014;55:5962–6.

Oliveira C, Harizman N, Girkin CA, Xie A, Tello C, Liebmann JM, *Ritch R..* Axial length and optic disc size in normal eyes. *Br J Ophthalmol.* 2007:91(1):37-39.

Osterberg GA, Topography of the layer of rods and cones in the human retina. *Acta Ophthalmol.* 1935;13:1-97

Pan C, Ramamurthy D, Saw S. Worldwide prevalence and risk factors for myopia. *Ophthalmic*

Physiol Opt. 2012:3–16.

Pararajasegaram R. VISION 2020-the right to sight: from strategies to action. *Am J Ophthalmol.* 1999;128:359.

Park SP, Chung JK, Greenstein V, Tsang SH, Chang S. A study of factors affecting the human cone photoreceptor density measured by adaptive optics scanning laser ophthalmoscope. *Exp Eye Res.* 2013;108:1-9.

Patel S, Marshall J, Fitzke FW. Refractive index of the human corneal epithelium and stroma. *J Refract Surg.* 1995;11:100–5.

Patel NB, Hung L-F, Harwerth RS. Postnatal maturation of the fovea in Macaca mulatta using optical coherence tomography. *Exp Eye Res.* 2017;164:8–21.

Rha J, Jonnal RS, Thorn KE, Qu J, Zhang Y, Miller DT. Adaptive optics flood-illumination camera for high speed retinal imaging. *Opt Express*. 2006;14(10):4552-4569.

Popescu D, Choo-Smith L-P, Flueraru C, Mao Y, Chang S, Disano J, Sherif S, Sowa MG.. Optical coherence tomography: fundamental principles, instrumental designs and biomedical applications. *Biophys Rev.* 2011;3:155–69.

Provis JM. Development of the human retina: patterns of cell distribution and redistribution in the ganglion cell layer. *J Comp Neurol.* 1985:429.

Provis JM, Diaz CM, Dreher B. Ontogeny of the primate fovea: A central issue in retinal development. *Prog Neurobiol.* 1998;54:549–81.

Provis J, Sandercoe T, Hendrickson AE. Astrocytes and blood vessels define the foveal rim during primate retinal development. *Invest Ophthalmol Vis Sci.* 2000;41:2827–36.

Provis JM, Hendrickson AE. The Foveal Avascular Region of Developing Human Retina. *Arch Ophthalmol.* 2008;126:507–11.

Provis JM, Dubis AM, Maddess T, Carroll J. Adaptation of the central retina for high acuity vision: Cones, the fovea and the avascular zone. *Prog Retin Eye Res.* 2013;35:63–81.

Putnam NM, Hofer HJ, Doble N, Chen L, Carroll J, Williams DR. The locus of fixation and the foveal cone mosaic. *J Vis.* 2005;5:632–939.

Read SA, Collins MJ, Vincent SJ, Alonso-Caneiro D. Macular retinal layer thickness in childhood. *Retina.* 2015;35:1223–33.

Recchia FM, Carvalho-Recchia CA, Trese MT. Optical Coherence Tomography in the Diagnosis of Foveal Hypoplasia. *Arch Ophthalmol.* 2002;120:1587–8.

Rich KA, Zhan Y, Blanks JC. Migration and synaptogenesis of cone photoreceptors in the developing mouse retina. *J Comp Neurol.* 1997;388:47–63.

Roberts PK, Nesper PL, Goldstein DA, Fawzi AA. Retinal capillary density in patients with

birdshot chorioretinopathy. *Retina*. 2018;38(2):387-394.

Rommel F, Siegfried F, Kurz M, Brinkmann MP, Rothe M, Rudolf M, Grisanti S, Ranjbar M. Impact of correct anatomical slab segmentation on foveal avascular zone measurements by optical coherence tomography angiography in healthy adults. *J Curr Ophthalmol.* 2018;30:156–60.

Romo J, Linderman R, Pinhas A, Carroll J, Rosen R, Chui T. Novel Development of Parafoveal Capillary Density Deviation Mapping using an Age-Group and Eccentricity Matched Normative OCT Angiography Database. *Trans Vis Sci Tech.* 2019;8(3):1.

Roorda A, Romero-Borja F, Donnelly Iii W, Queener H, Hebert T, Campbell M. Adaptive optics scanning laser ophthalmoscopy. *Opt Express* 2002;10:405–12.

Rossi EA, Weiser P, Tarrant J, Roorda A. Visual performance in emmetropia and low myopia after correction of high-order aberrations. *J Vis.* 2007;7:14

Rossi EA, Roorda A. The relationship between visual resolution and cone spacing in the human fovea. *Nat Neurosci.* 2010;13:156–7.

Salz D, Decarlo T, Adhi M, Moult E, Choi W, Baumal CR, Witkin AJ, Duker JS, Fujimoto JG, Waheed NK. Select Features of Diabetic Retinopathy on Swept-Source Optical Coherence Tomographic Angiography Compared With Fluorescein Angiography and Normal Eyes. *JAMA Ophthalmol.* 2016;134:644.

Samara Wasim A, Say Emil A. T, Khoo Chloe T. L, Higgins Timothy P, Magrath George L, Ferenczy Sandor L, Shields CL. Correlation of foveal avascular zone size with foveal morphology in noormal eyes using optical coherence tomography angiography. *Retina.* 2015;35:2188–95.

Sampson DM, Gong P, An D, Menghini M, Hansen A, Mackey DA, Sampson DD, Chen FK. Axial Length Variation Impacts on Superficial Retinal Vessel Density and Foveal Avascular Zone Area Measurements Using Optical Coherence Tomography Angiography. *Invest Ophthalmol Vis Sci*. 2017;58(7):3065-3072.

Sandercoe TM, Geller SF, Hendrickson AE, Stone J, Provis JM. VEGF expression by ganglion cells in central retina before formation of the foveal depression in monkey retina: Evidence of developmental hypoxia. *J Comp Neurol.* 2003;462:42–54.

Schneider CA, Rasband WS, Eliceiri KW. NIH Image to ImageJ: 25 years of image analysis. *Nat Methods* 2012;9:671.

Scoles D, Sulai YN, Langlo CS, Fishman GA, Curcio CA, Carroll J, Dubra A. In vivo imaging of human cone photoreceptor inner segments. *Invest Ophthalmol Vis Sci.* 2014;55:4244–51.

Schottenhamml J, Moult EM, Ploner S, Lee B, Novais EA, Cole E, Dang S, Lu CD, Husvogt L, Waheed NK, Duker JS, Hornegger J, Fujimoto JG. An automatic, intercapillary area based algorithm for quantifying diabetes related capillary dropout using optical coherence tompgraphy angiography. *Retina*. 2016;36 Suppl 1(Suppl 1):S93-S101.

Shapiro MB, Schein SJ, De Monasterio FM. Regularity and Structure of the Spatial Pattern of Blue Cones of Macaque Retina. *J Am Stat Assoc.* 1985;80:803–12.

Shimizu N, Nomura H, Ando F, Niino N, Miyake Y, Shimokata H. Refractive errors and factors associated with myopia in an adult Japanese population. *Jpn J Ophthalmol.* 2003;47:6–12.

Snodderly DM, Weinhaus RS, Choi JC. Neural-vascular relationships in central retina of macaque monkeys (Macaca fascicularis). *J Neurosci.* 1992;12:1169.

Song H, Chui TYP, Zhong Z, Elsner AE, Burns SA. Variation of cone photoreceptor packing density with retinal eccentricity and age. *Invest Ophthalmol Vis Sci.* 2011;52:7376–84.

Song H, Chui TYP, Zhong Z, Elsner AE, Burns SA. Variation of cone photoreceptor packing density with retinal eccentricity and age. *Invest Ophthalmol Vis Sci.* 2011;52:7376–84.

SPRINGER AD. New role for the primate fovea: A retinal excavation determines photoreceptor deployment and shape. *Vis Neurosci.* 1999;16:629–36.

Springer A, Hendrickson A. Development of the primate area of high acuity. 1. Use of finite element analysis models to identify mechanical variables affecting pit formation. *Vis Neurosci.* 2004a;21:53–62.

Springer AD, Hendrickson AE. Development of the primate area of high acuity. 2. Quantitative morphological changes associated with retinal and pars plana growth. *Vis Neurosci.* 2004b;21:775–90.

Springer AD, Hendrickson AE. Development of the primate area of high acuity, 3: Temporal relationships between pit formation, retinal elongation and cone packing. *Vis Neurosci.* 2005;22:171–85.

Stevenson S, Roorda A. Correcting for miniature eye movements in high-resolution scanning laser ophthalmoscopy. vol. spie-5688. 2005:145–51

Tam J, Dhamdhere KP, Tiruveedhula P, Manzanera S, Barez S, Bearse MA, Adams AJ, Roorda A. Disruption of the retinal parafoveal capillary network in type 2 diabetes before the onset of diabetic retinopathy. *Invest Ophthalmol Vis Sci.* 2011;52:9257–66.

Tan PE, Yu PK, Balaratnasingam C, Cringle SJ, Morgan WH, McAllister IL, Yu DY. Quantitative confocal imaging of the retinal microvasculature in the human retina. *Invest Ophthalmol Vis Sci.* 2012;53:5728–36.

Tan PE, Balaratnasingam C, Xu J, Mammo Z, Han SX, Mackenzie P, Kirker AW, Albiani D, Merkur AB, Sarunic MV, Yu DY. Quantitative Comparison of Retinal Capillary Images Derived By Speckle Variance Optical Coherence Tomography With Histology. *Invest Ophthalmol Vis Sci.* 2015;56:3989.

Tan CS, Lim LW, Chow VS, Chay IW, Tan S, Cheong KX, Tan GT, Sadda SR. Optical Coherence Tomography Angiography Evaluation of the Parafoveal Vasculature and Its Relationship With Ocular Factors. *Invest Ophthalmol Vis Sci.* 2016;57:OCT224–34.

Tam J, Martin JA, Roorda A. Noninvasive visualization and analysis of parafoveal capillaries in humans. *Invest Ophthalmol Vis Sci.* 2010;51:1691–8.

Tick S, Rossant F, Ghorbel I, Gaudric A, Sahel J-A, Chaumet-Riffaud P, Paques M. Foveal shape and structure in a normal population. *Invest Ophthalmol Vis Sci.* 2011;52:5105–10.

Tumahai P, Moureaux C, Meillat M, Debellemanière G, Flores M, Delbosc B, Saleh M. High-resolution imaging of photoreceptors in healthy human eyes using an adaptive optics retinal camera. *Eye.* 2018;32:1723–30.

Vajzovic L, Hendrickson AE, O'Connell R V, Clark LA, Tran-Viet D, Possin D, Chiu SJ, Farsiu S, Toth CA. Maturation of the Human Fovea: Correlation of Spectral-Domain Optical Coherence Tomography Findings With Histology. *Am J Ophthalmol.* 2012;154:779-789.e2.

Vitale S, Sperduto RD, Ferris FL. Increased prevalence of myopia in the United States between 1971-1972 and 1999-2004. *Arch Ophthalmol.* 2009;127:1632–9.

Wagner-Schuman M, Dubis AM, Nordgren RN, Lei Y, Odell D, Chiao H, Weh E, Fischer W, Sulai Y, Dubra A, Carroll J.. Race- and sex-related differences in retinal thickness and foveal pit morphology. *Invest Ophthalmol Vis Sci.* 2011;52:625.

Wan L, Wu Z, Chen X. Exome sequencing study of 20 patients with high myopia. *PeerJ.* 2018;6:.

Wang X, Kong X, Jiang C, Li M, Yu J, Sun X. Is the peripapillary retinal perfusion related to myopia in healthy eyes? A prospective comparative study. *BMJ. Open* 2016; 6(3):e010791.

Wang SW, Hung KC, Tsai CY, Chen MS, Ho TC. Myopic traction maculopathy biomarkers on optical coherence tomography angiography-An overlooked mechanism of visual acuity correction in myopic eyes. *Eye (Lond)*. 2019;33(8):1305-1313.

Webb RH, Hughes GW, Pomerantzeff O. Flying spot TV ophthalmoscope. *Appl Opt.* 1980;19:2991–7.

Wei Y, Jiang H, Shi Y, Qu D, Gregori G, Zheng F, Rundek T, Wang J. Age-Related Alterations in the Retinal Microvasculature, Microcirculation, and Microstructure. *Invest Ophthalmol Vis Sci*. 2017;58(9):3804–17.

Wen C, Pei C, Xu X, Lei J. Influence of Axial Length on Parafoveal and Peripapillary Metrics from Swept Source Optical Coherence Tomography Angiography. *Curr Eye Res.* 2019;44:980–6.

Wilk MA, Mcallister JT, Cooper RF, Dubis AM, Patitucci TN, Summerfelt P, Anderson JL, Stepien KE, Costakos DM, Connor TB Jr, Wirostko WJ, Chiang PW, Dubra A, Curcio CA, Brilliant MH, Summers CG, Carroll J. Relationship between foveal cone specialization and pit morphology in albinism. *Invest Ophthalmol Vis Sci.* 2014;55:4186–98.

Wilk MA, Dubis AM, Cooper RF, Summerfelt P, Dubra A, Carroll J. Assessing the spatial relationship between fixation and foveal specializations. *Vision Res* 2017;132:53–61.
Williams T.D. Determination of the true size of an object on the fundus of the living eye. *Optom*

Vis Sci. 1992;69:717–20.

Wojtkowski M, Bajraszewski T, Gorczyńska I, Targowski P, Kowalczyk A, Wasilewski W, Radzewicz C. Ophthalmic imaging by spectral optical coherence tomography. *Am J Ophthalmol.* 2004;138:412–9.

Wong TY, Foster PJ, Hee J, Ng TP, Tielsch JM, Chew SJ, Johnson GJ, Seah. Prevalence and risk factors for refractive errors in adult Chinese in Singapore. *Invest Ophthalmol Vis Sci.* 2000;41:2486–94.

Yang Y, Wang J, Jiang H, Yang X, Feng L, Hu L, Wang L, Lu F, Shen M. Retinal Microvasculature Alteration in High Myopia. *Invest Ophthalmol Vis Sci*. 2016;57(14):6020-6030.

Yang S, Zhou M, Lu B, Zhang P, Zhao J, Kang M, Wang R, Wang F, Sun X. Quantification of Macular Vascular Density Using Optical Coherence Tomography Angiography and Its Relationship with Retinal Thickness in Myopic Eyes of Young Adults. *J Ophthalmol*. 2017:1397179.

Yanni SE, Wang J, Chan M, Carroll J, Farsiu S, Leffler JN, Spencer R, Birch EE. Foveal avascular zone and foveal pit formation after preterm birth. *Br J Ophthalmol.* 2012:96(7):961-966.

Young TL, Metlapally R, Shay AE. Complex Trait Genetics of Refractive Error. *Arch Ophthalmol.* 2007;125:38–48.

Young RW. Cell proliferation during postnatal development of the retina in the mouse. *Brain Res.* 1985;353:229–39.

Yu J, Gu R, Zong Y, Xu H, Wang X, Sun X, Jiang C, Xie B, Jia Y, Huang D. Relationship Between Retinal Perfusion and Retinal Thickness in Healthy Subjects: An Optical Coherence Tomography Angiography Study. *Invest Ophthalmol Vis Sci.* 2016;57:204–10.

Yuodelis C, Hendrickson A. A qualitative and quantitative analysis of the human fovea during development. *Vision Res.* 1986;26:847–55.

Zadnik K, Mutti DO, Friedman NE, Adams AJ. Initial cross-sectional results from the Orinda Longitudinal Study of Myopia. *Optom Vis Sci Off Publ Am Acad Optom.* 1993;70:750–8.

Zhang T, Godara P, Blanco ER, Griffin RL, Wang X, Curcio CA, Zhang Y. Variability in Human Cone Topography Assessed by Adaptive Optics Scanning Laser Ophthalmoscopy. *Am J Ophthalmol.* 2015;160:290-300.e1.

Zhang Y, Liang XY, Liu S, Lee JWY, Bhaskar S, Lam DSC. Accuracy of Intraocular Lens Power Calculation Formulas for Highly Myopic Eyes. *J Ophthalmol.* 2016;1917268